Università degli Studi di Pisa

Facoltà di Ingegneria
Corso di Dottorato in Ingegneria Aerospaziale
XXIV Ciclo

Tesi di Dottorato

Cathode Processes in MPD Thrusters

Relatore
Prof. Mariano Andrenucci

Candidato
Riccardo Albertoni

Direttore del Corso di Dottorato
Prof. Giovanni Mengali

Dicembre 2012

To Paola Rossetti

Would you measure by your rules something that is not governed by them? Forget your own guidelines; seek first for appropriate rules.

Richard Wagner *Die Maistersinger: Act I*

Abstract

Magnetoplasmadynamic (MPD) thrusters have demonstrated performance and power handling capabilities which make them attractive for use on thrust-intensive and high energy missions, such as Earth to Mars transfer of a cargo vehicle or a crewed Mars mission. However, the performance and lifetime demonstrated so far with gaseous propellants are at best marginal for these missions. Thermionic cathodes have been long identified as the run-time limiting components in both steady-state and pulsed devices making them a priority in the development of future high power MPD thrusters.

In this dissertation, an experimental and theoretical investigation of high-current hollow cathodes performance is carried out to provide guidelines for scaling and increasing MPDT lifetime. It is found that, whether the cathode technology, quasi-steady application results in erosion rates not compatible with any real mission duration. As a consequence, a theoretical model is derived for the performance evaluation of steady-state thermionic cathodes and verified by comparison with experimental data available in the literature. The model includes the effect of non-equilibrium multi-step ionization and allows for estimation of the plasma penetration length. It is shown that the cathode operative temperature can be effectively reduced by using low-work function refractory ceramics or by seeding the gaseous propellant with alkali metal vapours. However, since the seed neutral number densities required for an effective covering of the surface are in the order of the propellant density or higher, an emitting layer can be maintained only at very high seed mass flow rates. It is thus concluded that the use of non-diffusing low-work function insert is preferred.

The physical insights obtained from this study can aid in defining design criteria and general guidelines for high-current hollow cathode design and performance evaluation.

Acknowledgements

I wish to express my sincere gratitude to my thesis advisor, Professor M. Andrenucci, for his guidance and motivation during the course of this investigation. Special thanks are also extended to Professor F. Paganucci for his enlightening discussion concerning this work.

Finally, and most importantly, I would like to thank those closest to me. I thank all my friends for sharing with me some of the most precious moments of my life. I am greatly indebted to my parents and brothers for all the moral support and for their unshakable confidence in my abilities for which my mere expression of thanks likewise does not suffice.
A very special thank-you goes to my wife Chiara for her relentless encouragement and loving support through both the good times and bad times.

Introspection

It comes the time to say "this is it", to stop adding paragraphs to a document that will neither be as clear nor as extensive as I would like it to be and admit to myself that I did my best.
This thesis has had a complicate evolution throughout the four years of my PhD. Plans had to change, the title itself changed twice since the start and I had many difficult times that made me question my skills, my inclination and ultimately my direction in the years to come. But I did not give up, thanks to the support from the people around me.
Now that it is almost done, I stop and think for a while. So I realize that the most important thing I have learnt during this PhD is the incredible extent to which scientific research can be frustrating: whenever one is trying something new, there is just no way to tell how it will end up, to guess whether any interesting result will come up at all.
When I started this long journey, I thought it was the new discovery, however small, that would make me happy and give me the energy to keep going. Never mind how difficult the path, because the nice part of researching is finding. Yet, it was difficult to realize that I was completely wrong. With such an attitude, I had a very hard time and I was not happy at all, my mind was not focussed and doing a good job became more and more challenging.
Eventually, I understood that I had to love what I was doing every day, regardless of the results I was getting. Only loving *doing research* and not the *results of the research* there is a chance to become a good researcher.
A peaceful mind works better and results come spontaneously. Perhaps.

Contents

Part I

MPD Thrusters and Cathode Operation

Chapter 1

Introduction

The idea of using electrical means to propel a spacecraft was formulated as early as 1906 by Robert H. Goddard and independently described by Tsiolkovsky in 1911 [1]. Goddard believed electric propulsion would "*go forward at some time in the future, as interest in the subject refuses to die, in spite of the frowns of some authorities*" [2]. He left the work of achieving scientific respectability to others like Herman Oberth in Germany and Shepherd in Britain. The first systematic analysis was undertaken by Ernst Sthulinger who, during the period from about 1929 to early 1950's, showed that practical electric propulsion system could be made offering substantial performance gains over chemical rocket systems. It is interesting to reflect on the fact that the primary concern of the early electric propulsion visionaries and pioneers was with the prospect of human piloted interplanetary travel, which still remains the *raison d'être* of the electric propulsion to the present day. In the recent past, both Russian and American scientists have considered again the manned mission to Mars as a viable long-term goal encompassing great opportunities for the future of humankind. Perhaps electric propulsion will play a vital role in turning this long-held dream into reality.

1.1 Electric Propulsion - Overview

The objective of all rocket systems is to induce a reaction force by expelling mass drawn from propellant tanks onboard a spacecraft. The magnitude of this force is given by the expression

$$T = \langle \dot{m} u_e \rangle \ , \tag{1.1}$$

where $\langle \dot{m} u_e \rangle$ represents a mean value of the product of propellant flow rate and velocity component along the thrust axis. The effect of applying such

a force on a space vehicle in an environment where gravitational forces are negligibly small is to change the velocity of the vehicle itself by an amount given by

$$\Delta v = \langle u_e \rangle \ln \left[\frac{m_i}{m_f} \right] , \tag{1.2}$$

where $\langle u_e \rangle$ is the mass-averaged value of the propellant exhaust velocity measured relative to the thruster along its axis while m_i and m_f are the spacecraft masses before and after the thrusting event, respectively. For a particular propulsion system to be attractive, its mass should be small, as should the propellant mass $\Delta m = m_i - m_f$ required to accelerate the final mass through the velocity change Δv. However, it is apparent from equation (1.2) that substantial changes in vehicle velocity, i.e. interplanetary missions, necessitate a very large initial-to-final vehicle mass ratio unless the propellant exhaust velocity is also large.

The great advantage of the electric propulsion over conventional chemical rockets is that the exhaust velocity (or specific impulse[1]) capabilities of electric thrusters are much greater and, as a result, the amounts of propellant required for a typical mission can be orders of magnitude lower. Since the cost for launching a satellite into low Earth orbit (LEO) is currently around 20 k$/kg, the benefit of using electric propulsion systems is evident.

Considering equation (1.2) alone might lead to conclude that the optimum exhaust velocity for a spacecraft approaches infinity. Generally, this is not the case since an energy source is also required so that a mass penalty associated with supplying this energy must be taken into account. In the case of chemical thrusters the energy is stored in the combustible fuel/oxidizer mixture. For an electric thruster, however, an external power source is required and its mass must be subtracted from the final mass to determine the useful payload delivered. The ratio of the electrical power P_E to the mass of the power plant m_P is defined as α and is referred to as the specific power. Its value hinges on technological advances and the electric thruster module configuration. At present, typical values of α range between 100 and 200 W/kg. The impact of the specific power on the optimum exhaust velocity is defined, in turn, by a number of mission considerations which reflect the fact that electric thrusters tend to be power limited rather than energy limited. In addition, even though a high exhaust velocity is mass-efficient, trip times using continuous, low-thrust trajectories may be longer than that for chemical propulsion using impulsive maneuvers. For a constant acceleration, $a = T/M_S$, where

[1] The specific impulse is historically used as a thruster performance parameter. It is defined as the thrust per unit earth-weight propellant consumption rate and it is approximately equal to the mean exhaust velocity divided by the sea-level gravitational acceleration, $I_{sp} = \langle u_e \rangle / g_0$. It is expressed in units of seconds.

T is the thrust and M_S is the mass of the spacecraft, the trip time can be expressed as the total velocity change divided by the average acceleration of the vehicle, namely $\tau \simeq \Delta v/a$. Since typical values for the acceleration are in the order of $10^{-4}\, g_0$, for a 5 km/s Δv mission a total thrusting time of about 8 weeks is needed. It is apparent, therefore, that a time penalty for operating at low continuous thrust must be considered. However, the optimum exhaust velocity of an electric thruster delivering a given payload in a reasonable time lies in the $10^1 - 10^2$ km/s range [3]. Such exhaust velocities are still an order of magnitude greater than those for the best chemical rockets and, as a result, the initial masses of electrically propelled vehicles are substantially less than those for chemical systems delivering the same payload.

Since Goddard's early work, it has been recognized that plasma thrusters can be classified according to the mechanisms for plasma production and acceleration. Plasma production and heating is achieved by either direct-current biased electrodes or alternate current antennas. Plasma acceleration mechanisms are best identified in the MHD momentum equation,

$$\nabla \cdot \rho \boldsymbol{u}\boldsymbol{u} = \varepsilon_0 \left(\nabla \cdot \boldsymbol{E}\right) \boldsymbol{E} + \boldsymbol{j} \times \boldsymbol{B} - \nabla \cdot \bar{\bar{P}} \,, \tag{1.3}$$

where ρ is the mass density, $\boldsymbol{u}$ is the fluid velocity of the plasma, $\boldsymbol{j}$ is the electric current density, $\bar{\bar{P}}$ is the pressure tensor, ε_0 is the vacuum permittivity while $\boldsymbol{E}$ and $\boldsymbol{B}$ are the electric and magnetic fields, which can be either applied externally or self-induced by the plasma. Both ρ and $\boldsymbol{u}$ are determined by the massive ions, while the main contribution to $\boldsymbol{j}$ comes generally from electrons. The prevalence of any of the three terms on the right-hand side of equation (1.3) classifies a plasma device as *electrostatic*, *electromagnetic* or *electrothermal* thruster. However, this classification is by no means exhaustive and some concepts may fall into more than one category.

Electrothermal devices, such as arcjets, involve electrical heating and subsequent acceleration of a propellant through a nozzle to induce a reaction force. The maximum temperature of the working gas is limited by the melting temperature of the thruster structure. Since $I_{sp} \propto \sqrt{T}$, the operative temperature places a ceiling on the specific impulse that electrothermal thrusters can actually attain, typically between 500 and 1200 seconds [4]. Moreover, the high temperature of the thruster walls limits the lifetime of the arcjet to no more than 10^3 hours [5].

Electrostatic devices, such as ion thrusters (GIT), rely on Coulomb forces to accelerate a propellant composed of charged particles. Since the magnetic field is negligible in the acceleration region, the electrostatic thrusters must have a non-zero net charge density ρ_e to generate thrust. In electron bombardment ion engines, ions are created by bombarding the neutral flow with

high energy electrons. The ions are then accelerated to energies of few keV by a pair of grids biased at different voltages [6]. Downstream of the acceleration region a hollow cathode is required to supply electrons into the ion beam to prevent spacecraft charging. The main drawback of ion engines is the space-charge limited ion current density as given by the Child-Langmuir law, namely $j_i \propto V^{3/2}$ where V is the applied voltage. The previous relation explains why the ion thruster is a high-voltage, low-current device encompassing a bulky and sophisticated power processing unit [7, 8].
Hall effect thrusters (HET) are a widely commercialized electric devices in direct competition with the ion thrusters. Since its introduction in the field, there was considerable discussion about the classification of such thruster according to its acceleration mechanism. In the light of equation (1.3) the HET is an electromagnetic plasma accelerator, where the plasma momentum gain comes mainly from the magnetic force due to the interaction between the azimuthal current density and the applied near-radial magnetic field [9]. However, at the kinetic level, the axial Lorentz force which transfer the thrust to the thruster body through the magnetic field lines comes mainly from an electrostatic acceleration of the unmagnetized ions by the ambipolar electric field created in the plasma volume [10]. Moreover, since the condition of quasi-neutrality is satisfied within the closed-drift region, there is no limitation on the attainable ion current density by space-charge effects. All in all, the discussion about its clssification seems to be somewhat academic since the Hall accelerator may be thought of as a crosslink between an ion engine and an electromagnetic thruster. Considering that in a HET the thrust scales as $T \propto \sqrt{V}$ much like the ion thrusters, it was decided to include it among electrostatic thrusters. A Hall effect thruster typically operates with xenon as propellant at discharge voltages in the range 200-400 V. These thrusters achieve specific impulses of 1500-2000 s with thrust efficiencies in the 45-55% range.
Electromagnetic devices, such as magnetoplasmadynamic (MPD) thrusters, are characterized by a net-current free plasma so that no external neutralizer is required. When operated in the pure electromagnetic regime, i.e. magnetic Reynolds number much greater than unity, the plasma acceleration comes from the interaction between the magnetic field, either externally applied or self-induced, and the discharge current density [11, 12]. Since the transition between the electrothermal to the electromagnetic regime requires discharge currents of few thousand amperes [13], the MPD thruster is a high-power device only. The current lack of such outstanding in-space power plants along with its modest thrust efficiency (<40% using noble gases) have hampered the development of such a thruster, relegating it to a status of laboratory

technology in need of much refinement [14, 15].

1.2 The MPD Accelerator

Magnetoplasmadynamic (MPD) thrusters[2] are simple and compact devices that rely on steady-state crossed electric and magnetic fields to produce a continuous stream of high-velocity plasma. Among its many engineering attractions, MPD propulsion system can count a wide range of attainable exhaust velocities, thrust densities of $10^2 - 10^3\ N/m^2$, utilization of a broad gamut of space-compatible propellants, minimal power-processing interfaces to space power sources and good ranges of in-flight throttleability. Among its potential debits are its low efficiency of conversion of input power to axially directed plasma acceleration, reduced lifetime associated with electrodes erosion and the onset of a strongly unstable regime when operated above a critical value of the discharge current for a given mass flow rate. Despite all shortcomings, MPD thrusters still basically remain the only possible option among electric propulsion concepts for future interplanetary missions.
The MPD plasma accelerator consists of a central cathode, an annular coaxial anode and a suitable interelectrode insulator, configured in variations like those sketched in Fig. 1.1. The propellant, either noble gas or metal vapor, is introduced axially through the backplate or through a central hollow cathode, whereupon it is ionized by its passage into an intense radial, azimuthally uniform, electric field. When the self-generated azimuthal magnetic field interacts with both radial and axial arc current, an axial and radial body-force component is exerted on the plasma stream, directly accelerating it downstream and compressing it toward the thruster centerline. Subsequent axial expansion combined with the direct axial acceleration, yields to exhaust plume velocities in the order of $10^1 - 10^2$ km/s and thrust levels in the range $10^{-1} - 10^2$ N. The optimum power range for the operation of such accelerators is delimited on the underside by the desirability of full ionization of the propellant along with fractionally small electrode losses while, on the topside, by the onset of plasma instabilities and untoward erosion of the electrodes. It has been theoretically shown by Alvén [16] that full ionization is attained for a total arc current I higher than a critical value given by

$$I_{fi} = \left[\frac{\dot{m}}{b}\right]^{1/2} \left[\frac{2\varepsilon_i}{M_a}\right]^{1/4}, \tag{1.4}$$

[2]The appellation "MPD arcjet" is sometimes used, especially in the Japanese literature. It is advisable to avoid using the term arcjet since it has traditionally been reserved to denote a class of arc-heated electrothermal devices in which electromagnetic effects are not dominant. Antiquated names like "plasma-jet engine", "plasma jet boosters" and "plasmatron" appear in the older and Soviet literature.

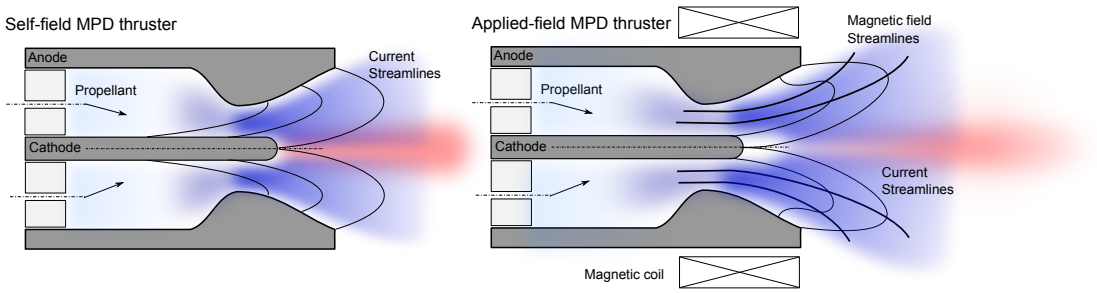

Figure 1.1: Illustration of self-field and applied-field MPD thrusters

where ε_i is first ionization potential of the propellant, M_a is its molecular weight and $b = T/I^2$ is the electromagnetic thrust parameter, typically $b \simeq 2 \times 10^{-7}\ N/A^2$ [14, 17]. Using 3 g/s of argon, I_{fi} is then about 12 kA, at which current the terminal voltage settles to about 10^2 V yielding to a thrust of 25 N and a total power of about 1 MW. Moreover, the anode fall voltage was found to be almost constant over a wide range of discharge currents resulting in a decreasing fraction energy deposition with increasing total power, so that the anode fall reaches tolerable proportions only in the megawatt range [18]. It is thus clear that self-field MPD thrusters operate most efficiently in the $10^0 - 10^1$ MW power range, which is more than an order of magnitude higher than the available power on-board present spacecrafts. In addition, since the acceleration mechanism based on the Lorentz force relies upon collisional momentum transfer between electrons and ions, the inherent frictional dissipation limits the maximum attainable thrust efficiency at $65 - 70\%$ [19–21].

Nevertheless, it was found that the addition of an applied magnetic field arranged so as to diverge in a nozzle fashion toward the exit significantly increases the thruster performance at power levels lower than 500 kW [22]. The applied longitudinal magnetic field induces an azimuthal current in the plasma so that the resulting axial Lorentz force adds to the contribution of the self-field B_ϑ, the radial applied field B_r, namely $f = j_r B_\vartheta - j_\vartheta B_r$. Since $B_\vartheta \propto I$, at low discharge currents the self-field is negligible and the applied-field MPD thruster should be considered as an independent thruster with $T \propto BI$ in contrast to self-field MPD thruster where $T \propto I^2$ [11, 23].

Beyond the realism of available in-space power sources, the upper bounds on MPD operation are set by excessive electrode erosion rates and the inception of the so called *onset phenomena* which induce intense fluctuations of thruster terminal voltage. Even though the number of contributions to this topic is enormous, embracing a host of different physical phenomena, most of

the accepted theories fall into two categories: plasma instabilities [24–26] and anode starvation [27–29]. As a matter of fact, any current-carrying plasma is potentially unstable to oscillations of character and frequency dependent on the plasma state and the magnitude of the current driven through it. These oscillations are manifested in local plasma densities, electric fields, electrical conductivity and other transport processes that may precipitate macroscopic instabilities, enhanced internal dissipation and electrode erosion. The anode starvation model, which is often referred as the triggering mechanism for plasma instability, argues that the radially inward directed component of the Lorentz force reduces the density of charge carriers nearby the anode up to the point at which it can no longer collect the total current imposed by the external circuit. As a result, the current transport to the anode is largely inhibited leading to the so called current saturation, which is supposed to trigger a macroscopic unstable behavior of the accelerator. At whatever level of sophistication these issues are approached, the essential point is that any anomaly, by definition, is a significant departure from some pattern of established behaviour which, for MPD accelerators, is yet to be fully defined. Clearly, some understanding and control of such anomalies is requisite to the enhancement of MPD thruster performance.
Considerable experimental studies of electrode erosion processes have also been undertaken, reaching its most sophisticated form in a sequence of radioactive surface-layer ablation studies that can track monolayer erosion rates inside an operating thruster as functions of positions and time [30]. Such studies have identified the cathode as the primary limiting component of the thruster assembly. Since the erosion processes depend on a complex coupling between plasma discharge characteristics, plasma-wall interactions and electrode phenomena, a deeper theoretical and experimental understanding of the factors driving the cathode phenomena is of paramount importance for the lifetime prediction of MPD thrusters.

1.3 Hollow Cathode Operation

In its simplest configuration, a hollow cathode consists of a thin-walled refractory metal tube operating at surface temperatures high enough to guarantee a proper electron thermal emission, i.e. between 2500 and 3000 K. This configuration is usually called open-channel or single-channel hollow cathode (ScHC) and is shown in Fig. 1.2. The thruster propellant, or a significant fraction of it, must be supplied through the cathode while an anode, located downstream of the cathode exit section, establishes the potential needed for the self-sustainment of the arc discharge. Under these conditions a dense nearly-Maxwellian plasma is formed within the tube. Typically, the cathode

interior plasma is characterized by modest electron temperature and plasma potential, namely $T_e \simeq 1 - 2\ eV$ and $V \simeq 10^1\ V$.
Electrons emitted from the cathode surface via field-enhanced thermionic process are accelerated into the plasma bulk through the sheath. These electrons, also known as *primary electrons*, acquire sufficient energy to enable ionization of the neutral atoms through multi-step inelastic collision processes. The region of the cathode from which electrons are emitted, called *active zone*, is located adjacent to the exit section of the tube [31]. The length of this region is in the order of the mean free path for energy exchange, λ^*, due to the degrading collisions between the primary electrons and either neutral atoms or thermalized electrons [32]. Each primary electron yields, on the average, one additional electron due to ionization, meaning that the volume and surface processes equally share the total discharge current. Neither emitted electrons nor thermalized electrons can reach the cathode surface, because of the adverse potential gradient which exists at the cathode sheath. As a consequence, they leave the cathode cavity at their rate of supply so that in the plasma bulk the current conduction is electron-dominated. Moreover, the electrostatic confinement of the primary electrons force them to expend most of their energy in ionization and excitation events leading to a higher ionization efficiency with respect to conventional solid rod cathodes [33]. Since the sheath thickness is on the order of several Debye lengths, $\lambda_D \propto \sqrt{T_e/n_e}$, and in high current plasmas this is typically less than a mean free path for ionization, the sheath region can be considered collisionless. Ions created in the cavity bombard the internal surface, helping the cathode to maintain the temperature needed for the thermionic electron emission. It is interesting to note that since in the bulk plasma most of the current is carried by the electrons while in the sheath region a substantial fraction of the current must be carried by the ions to generate the positive space charge that shields the plasma from the cathode potential, a zone over which a transition between these two current conduction mechanisms occurs must exists. This region is known as ionization zone and is of primary importance in the physics of hollow cathodes. If the cathode wall is fully catalytic, all the ions recombine at the internal surface and re-enter the plasma bulk as neutral atoms. The required rate of neutral atom supply is determined by the need of maintaining $\lambda^* \propto n_0^{-1} \simeq D_C$, where n_0 is the neutral number density and D_C is the cathode diameter [32]. Unfortunately, when working at high currents, as for MPD accelerators, the tube diameter must be large in order to maintain the current density below the critical value for which the lifetime of the cathode would be unduly curtailed, typically $10^6\ N/m^2$. In this case the mass flow rate must be greatly increased to guarantee proper operation of

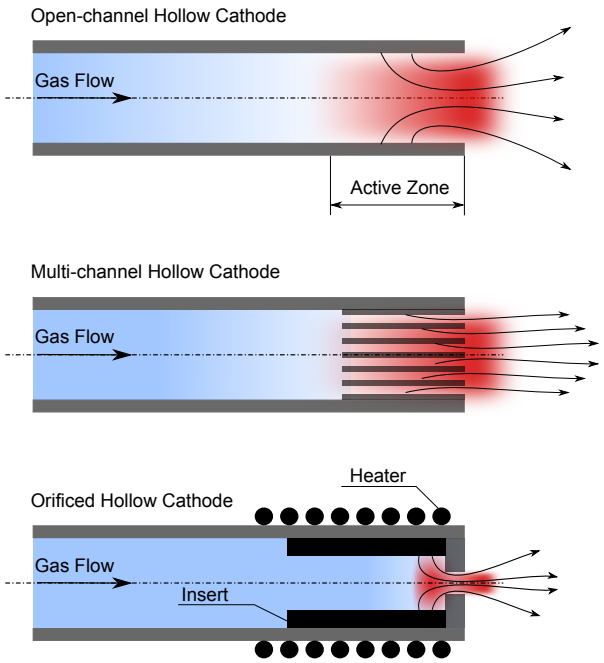

Figure 1.2: Illustration of hollow cathode configurations

the cathode, thereby reducing the performance of the propulsive system. To overcome this limitation, two variants of the open-channel configuration were developed: the multi-channel hollow cathode (McHC) and the orificed hollow cathode (OHC).

1.3.1 Multi-channel Hollow Cathode

A multi-channel hollow cathode consists of a refractory metal tube containing several longitudinal, parallel channels through which the gas flows into the thruster acceleration chamber. Such a structure can be achieved by laser-drilling longitudinal holes in a solid metal plate placed on the downstream end of the cathode or by introducing a bundle of refractory metal rods where channels are created by the inter rod spacing. Once the discharge has been ignited, the rods fuse together creating a single structure with the external tube. Each of those channels can be thought as a ScHC characterized by a large axial pressure gradient along its length. However, unlike ScH cathodes, thermal conductive and radiative losses are greatly reduced in McHC for mere geometrical reasons since a fraction of the outward radially directed energy from each channel is transferred to the contiguous ones. The improved thermal coupling between the channels leads to a reduction in the discharge

voltage for a given operating temperature [34]. Although McH cathodes are well suited for MPDT applications due to their limited gas flow consumption, previous studies indicate that no substantial reduction in wall temperature can be accomplished through simple geometric changes of the electrode [35]. As a matter of fact, McH cathodes were employed almost exclusively on lithium-fed MPD thrusters (LiLFA), where the observed negligible cathode erosion is much likely due to alkali-induced work function reduction rather than to the multichannel technology itself [36].

1.3.2 Orificed Hollow Cathode

An orificed hollow cathode, like the one shown in Fig. 1.2, consists of a refractory metal tube that is electron-beam welded to an orifice plate. These cathodes usually come with a low-work function insert located within and electrically connected to the main tube. Before the discharge initiation, the emitter is heated to thermionic emission temperatures by an external source, typically a resistive heating element in physical contact with the exterior of the tube. The orifice plate serves as a physical barrier acting to retain the neutral gas pressure inside the insert region, increasing the propellant stay-time and thus the ionization probability. Most of the pressure gradient is located within the orifice, so that the inert region acts as a reservoir for the propellant with a nearly constant total pressure.
Orificed hollow cathodes are generally classified according to the nature of the emitting surface used, namely *dispenser* cathodes, *rare-earth* cathodes and *elementary* emitters. The insert of a dispenser cathode consists of a refractory-metal porous matrix filled with an emissive compound such as Ba or Sc carbonates. The porous metal matrix acts as a reservoir from which the emissive material can diffuse to the surface where a low-work function active layer is formed. Even though no other cathode can provide the same stability of operation and the low work function of the dispenser cathodes ($\sim 2\ eV$), they are prone to oxygen contamination. Since no chemistry is involved in establishing the low work function surface, rare-earth emitters, such as LaB_6 and CeB_6, provide a superior resistance to contaminants ad moisture along with a reduced evaporation rate at the additional cost of a fairly higher work function ($\sim 2.7\ eV$). Finally, elementary emitters have no low-work function insert and no external heating device so that the electron emission is directly from the walls of the main tube. Since typical work functions of refractory metals are about $4.5\ eV$, this type of electron source has a lifetime of no more than few hundred hours. At the discharge currents inherent in MPD thrusters ($\sim 10^3 - 10^4\ A$), the use of dispenser hollow cathodes is largely hampered by the excessive evaporation of the emissive compound [37] and elementary emitters have been long recognized as impractical for long-duration missions

due to their excessive erosion rates [38]. Pioneering works of Goebel showed that rare-earth emitters are suitable for prolonged operations at few hundred amperes maintaining the lifetime in the $10^3 - 10^4$ hours range. These results are encouraging and may pave the way for substantial improvements in the lifetime of MPD accelerators [39, 40].

1.4 Dissertation Objectives and Outline

The ultimate goal of the present research is to get a deeper insight into the physical processes involved in the cathode of an MPD thruster. Interest in such processes derives from the need to achieve design guidelines to narrow the gap towards space-qualified accelerators. To achieve this goal both experimental and theoretical methods were used with a particular focus on the following questions:

- *What are the dominant power dissipation components in MPD thrusters*?

  Which is the dominant power sink in MPD thrusters and how different plasma parameters and material properties affect the power distribution?

- *What are the main physical processes determining the performance of hollow cathodes*?

  Specifically, what is the main electron emission mechanism? Which is the dominant ionization mechanism in high-current hollow cathodes? Is it possible to derive simple scaling relations for the cathode behavior?

- *Is it possible to devise a method to extend the cathode lifetime*?

  Since the lifetime is directly tied with the cathode temperature, is there any mean to significantly reduce the maximum cathode temperature for a given operative condition?

Using both empirical data and theoretical models, this thesis attempts to draw conclusions for each of the above questions.

The remainder of this dissertation presents the theoretical models and the experimental data used to validate them. Chapter 2 describes the experimental apparatus, the testing facility and illustrates the main results of the experimental investigation. Chapter 3 is devoted to the analytical performance model used to derive physical insights on the power distribution in MPD thrusters. In the same Chapter, the theoretical results are then compared to the experimental data. In Chapter 4 and Chapter 5 the main electron emission and ionization mechanisms are reviewed and simple models for the

field-enhanced thermionic emission and for the multi-step ionization in a hollow cathode are presented. In Chapter 7 a model for the prediction of the voltage drop, the temperature and the plasma penetration length is formulated and validated against the experimental data. Finally, in Chapter 8 a summary of the most important findings is presented along with a discussion concerning the open questions raised during this work.

Chapter 2

Experimental Investigation

In this section the results of the experimental campaign concerning the 100-kW AF-MPD thruster are presented and discussed[1]. The primary goal of these experiments was to assess the thruster performance in terms of thrust, thrust efficiency and specific impulse. Moreover, a multi-channel hollow cathode (McHC) was employed in the present experiments to investigate the effectiveness of such a technology in pulsed, quasi-steady applications. The data collected provided a complete characterization of AF-MPDT operation and significant insights into McHC behaviour. In addition, the results acquired in these experiments have been obtained extending the current pulse duration to 0.5 s allowing for a time-resolved thruster measurement. The present data indicate that the thrust scales linearly with the product of the discharge current and the applied magnetic field strength suggesting the predominance of the swirl acceleration mechanism in the thrust generation. Moreover, the use of a central McHC did not provide substantial benefits in terms of terminal voltage or erosion rate even though some significant insights into hollow cathode operation were achieved.

2.1 MPD Thruster Design

A coaxial plasma accelerator driven by protracted pulses of current in the range of $10^2 - 10^3$ A and synchronized mass flow rates from 60 to 120 mg/s of argon was designed and tested. The thruster, designed after the Russian "Ageyev-type" high-current plasma accelerator and shown in Fig. 2.1, employed a central multichannel hollow cathode and a coaxial flared anode [35]. A molybdenum alloy (TZM) cathode with an inner diameter of 40 mm and

[1]The experimental results discussed in this chapter were presented at the 32nd International Electric Propulsion Conference held in Wiesbaden, Germany [41]

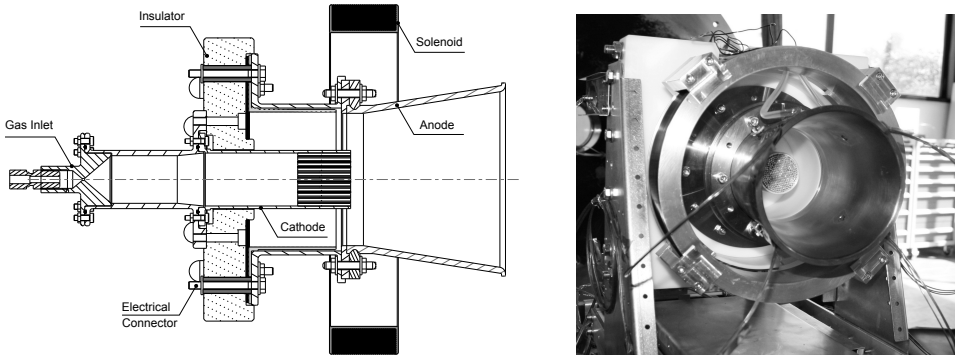

Figure 2.1: Schematic of the 100-kW AF-MPD thruster

a wall thickness of 2 mm was used. The inside of the cathode was tightly packed with 330 W-La rods of 2 mm diameter and 40 mm length each. The open cross section after filling, A_v, was about 220 mm^2, leading to a packing porosity of approximately 17%. A slightly divergent ($\alpha \simeq 20\ deg$) oxygen-free copper (OFC) anode having a minimum diameter of 100 mm was used for a maximum anode-to-cathode radius ratio $\bar{R} \equiv R_a/R_c$ of about 3. The anode and the cathode assemblies were electrically insulated form each another by an acetal resin (Delrin® 100 NC010) flange. The use of copper and non-refractory ceramics is justified by the negligible thermal loads when the thruster is operated in pulsed regime. Clearly, steady-state operations require a fairly different material selection. The applied magnetic field was provided by a 430 turns coaxial solenoid capable of generating a magnetic field strength up to 130 mT with a current of about 60 A. The solenoid was designed to minimize the total mass ($m_S \simeq 5\ kg$) and the thermal power losses ($P_s < 5$ kW) at the nominal magnetic field of 80 mT as measured on the thruster centerline at the cathode tip. In this condition the applied magnetic field strength is of the same order of magnitude of the self-induced one, namely $\bar{B} \equiv B_a/B_{sf} \simeq 4$.

2.2 Apparatus and Diagnostics

The measurements reported herein were conducted in the IV-10 facility at Alta. The chamber consists of a cylindrical stainless steel section of 10 m in length with an inner free diameter of about 6 m. The pumping system consists of eight pumps and five cold panels capable of an ultimate vacuum level lower than $2 \cdot 10^{-9}$ mbar and a pumping rate of about 300,000 l/s (for xenon). The pressure was monitored by three Leybold-Inficon ITR90 Pirani/Bayard sensors placed symmetrically on opposite sides of the vessel. The vacuum

chamber operated at a base pressure in the low-10^{-5} mbar range and approximately $2 \cdot 10^{-4}$ mbar during the thruster operation without cryogenic pumping. After each pulse, a minimum of 10 minutes was required for a complete recovery of the initial base pressure.
High-purity argon, grade 4.8, was used as propellant. The gas feeding system

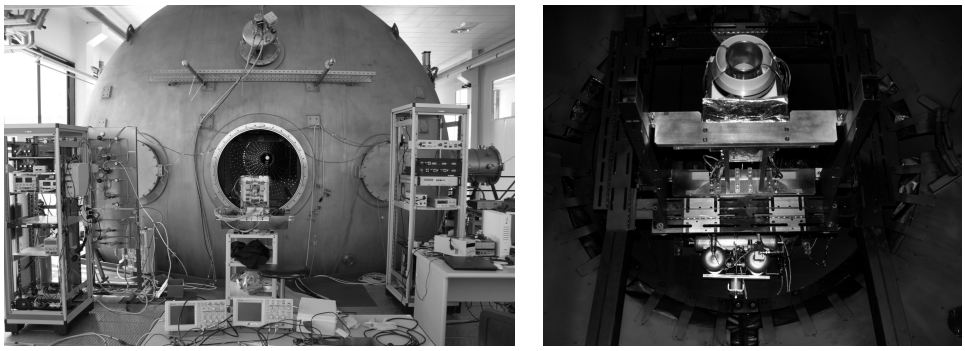

Figure 2.2: IV-10 vacuum facility (right) and the 100-kW AF-MPD thruster before operation (left)

consisted of a 8.5 l main reservoir positioned inside the vacuum chamber to prevent air contamination. This system was designed to guarantee a top-flat gas pulse of about 2 seconds for a maximum pressure loss of approximately 10%. Prior to each shot, the reservoir was filled with argon up to a given pressure corresponding to the desired mass flow rate; 225 mbar and 380 mbar for 60 mg/s and 120 mg/s, respectively. The propellant was injected through the cathode by means of a fast acting solenoid valve (FAV). The time delay between the opening of the FAV and the achievement of a top-flat gas signal was recorded during the calibration procedure [42] and used to trigger the discharge process. This procedure allowed for a mass flow rate measurement with an overall uncertainty within $\pm 5\%$ of the value.
The quasi-steady current pulse to the thruster was provided by a bank of four Maxwell Technologies BMOD-0165 supercapacitors (SCs) in series. Each 165 F capacitor is capable of delivering a maximum peak current of 5000 A for a rated charging voltage of 48 V leading to a maximum bank voltage of about 190 V. Prior to each firing, a dedicated power supply charged the SCs to the voltage value corresponding to an estimated discharge current. The relationship between the charging voltage and the discharge current was preliminary estimated on the basis of previous test campaigns and refined by a dedicated test session. A pulse forming network (PFN) was used as thruster igniter. The PFN, widely used in previous MPD tests with short pulses (up to 5 ms) at Alta [43], consists in a bank of 180 capacitors and inductances allowing to

store energy at a rate of 600 J/s from a HVL Series 311-6203 charging unit. The PFN circuit was isolated from the SCs bank via high-currents Semikron SKN-240 diodes. The initiation of the gas breakdown was controlled by the closure of a mercury vapor igniter. A customized 240 kW DC power supply was used to provide the current pulse to the solenoid. A schematic of the electrical feeding system is shown in Fig. 2.3

The thrust measurements were recorded using a single axis, double-pendulum

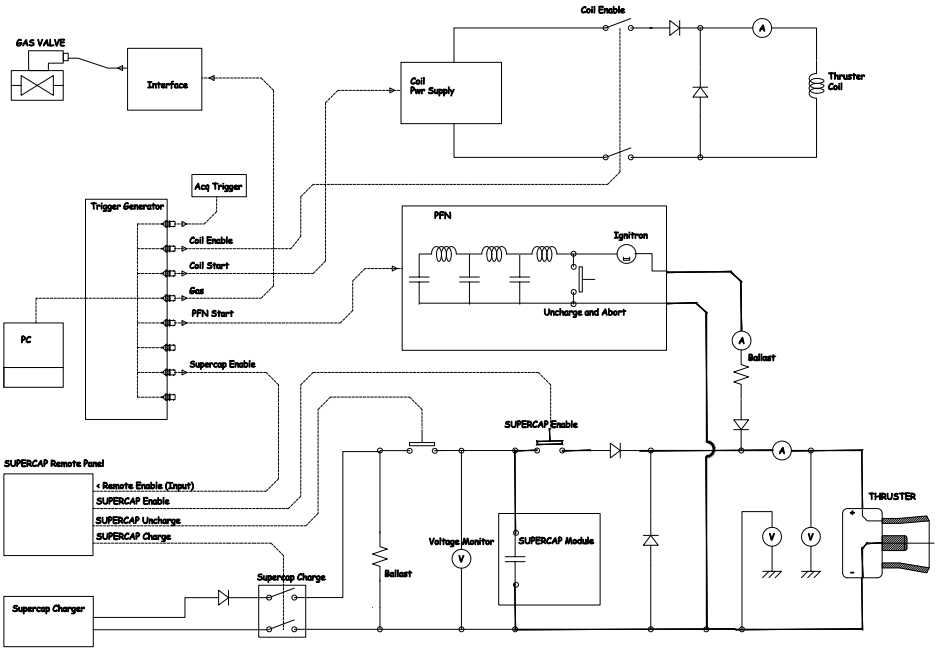

Figure 2.3: Schematic of the electrical feeding system

thrust stand. The thrust balance was mounted on a tilting platform to guarantee a proper leveling during the calibration while an electromagnetic calibrator was used to generate a reference force of 2 N in order to check the response of the thrust stand prior to each firing. The sensing elements are based on high-precision optical stain gages measuring the strain on the flexural elements. The thrust stand frequency response is about 15 Hz for a maximum thruster mass of 25 kg. For the performance measurements, thruster operation was monitored in real time by a Tektronix TDS224 digital oscilloscope. The monitored properties include the solenoid current, discharge current and voltage along with the thrust. The terminal voltage was evaluated by independently measuring the cathode-to-GND and the anode-to-GND voltages via Tektronix P5100 voltage probes connected to the feedthrough terminals at the vacuum chamber header. The voltage drop was then obtained by

subtracting one signal from the other. The discharge current was measured using a single LEM LT-4000S probe at the cathode cable. The error associated with the DC voltage measurements was ±2% while a relative error of ±1% was evaluated for the current measurements. Thrust, specific impulse and thrust efficiency measurement uncertainties were found by accounting for all aforementioned errors resulting in ±5%, ±7% and ±11% relative error, respectively.

2.3 Results and Discussion

2.3.1 Data Reduction

Three non-sequential measurements for each operating condition were performed in order to asses the repeatability of the data. For each data point the standard deviation of the sample mean was obtained over an automatically-defined time window. Figure 2.4 shows typical measured arc current and voltage signals along with the considered time window. Through the experimental determination of the thrust, T, and mass flow rate, $\dot{m}$, the thruster performance was calculated in terms of thrust efficiency $\eta_T = T^2/(2\dot{m}P)$ and specific impulse $I_{sp} = T/(g_0\dot{m})$. The required power to operate the solenoid was not included in the calculation of the thrust efficiency since $P \gg P_s$ for all the operative conditions investigated. Error bars account for both the standard deviation and the measurement uncertainty. Where not explicitly indicated, the dimensions of the symbols used are larger than the related error.

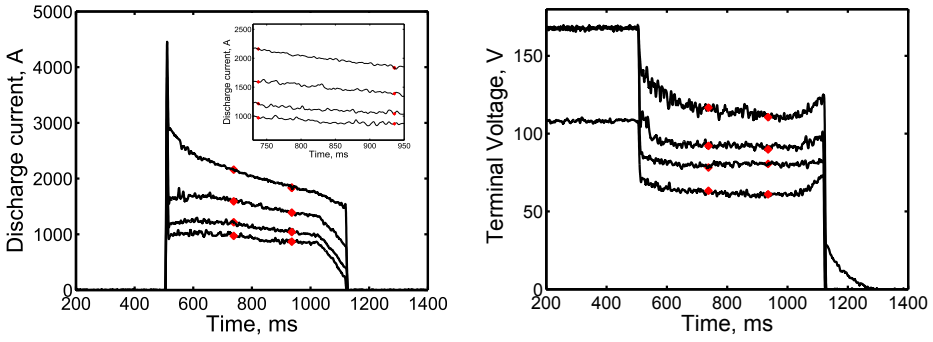

Figure 2.4: Typical filtered current (left) and voltage (right) signals

2.3.2 Performance Data

Values of current and voltage for different mass flow rates and applied induction fields are reported in the electrical characteristics of Fig 2.5. The V-I

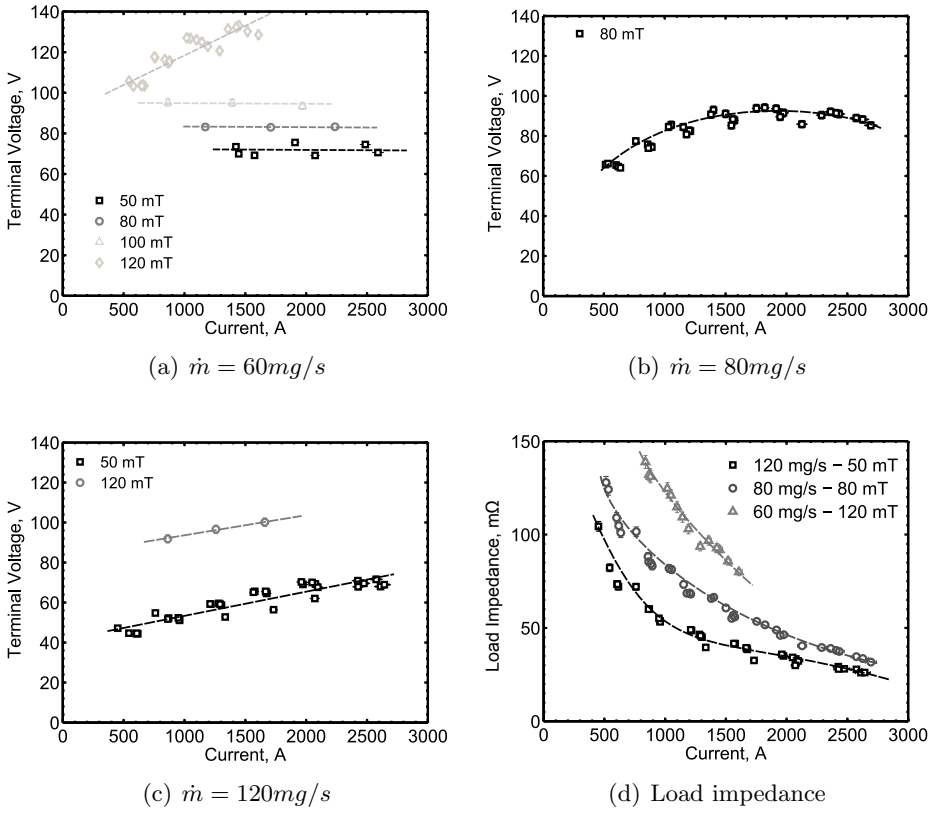

(a) $\dot{m} = 60mg/s$ (b) $\dot{m} = 80mg/s$

(c) $\dot{m} = 120mg/s$ (d) Load impedance

Figure 2.5: Electrical characteristics for different mass flow rates of Ar. Dashed lines are a guide to the eye.

data are in good agreement with other experimental observation reported in the literature as far as concerns the increase in terminal voltage with the magnetic field strength [44–46]. This result is widely known and frequently reported as the magnetic field affects the radial electron mobility toward the anode. The electron mobility in the confining **E**x**B** electron drift is provided mainly by the electron-neutral collisions entailing an increase in frictional dissipation and, thus, in terminal voltage. For a given magnetic field strength, the voltage was found to be almost constant for a wide range of arc currents (500-2500 A) implying a reduction in the overall load impedance, as shown in Fig. 2.5. Similar results were also reported by Myers [45–47] in an extensive series of experiments on a 100-kW class steady-state thruster as well as by Wegemann [48] and Winter [49] during the testing of the ZT-3, steady-state, thruster. This trend may indicate that the full ionization regime was not achieved. Under full ionization conditions, the propellant is exhausted at a

velocity close to the so called critical ionization velocity (CIV) and it is only after the full ionization condition that the thruster complies with the typical $V \propto I^3$ law. For a self-field device, the discharge current corresponding to the full ionization is given by $I_{fi} = \sqrt{\dot{m}\varepsilon_i/b}$, where $b = T/I^2$ is the electromagnetic thrust coefficient. However, no such scaling relation exists for applied-field thrusters and thus no estimations can be made to prove the hypothesis of a partially ionized propellant. As regards the terminal voltage at 80 mg/s, the experimental results are somehow unexpected since a decreasing V-I trend does not comply with any characteristic electrical response of the thruster. This behavior might be tied with an increased erosion at high currents and, thus, to an higher electron density in the discharge chamber.

A typical trace of the calibration signal and thrust measurement is shown in Fig. 2.6 where three thrust measurements refer to 60 mg/s of argon, 110 V charging voltage, at different magnetic induction levels. The calibration sig-

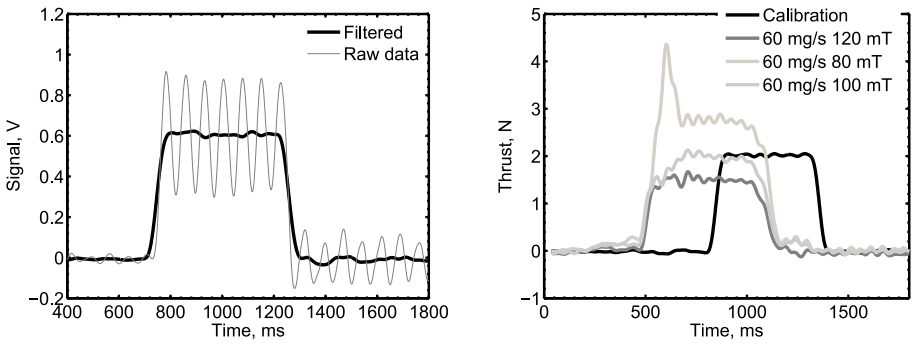

Figure 2.6: Typical thrust calibration signal (left) and thrust measurement at 110 V SCs bank charging voltage (right)

nal is also depicted and intentionally shifted to allow for a better comparison with the experimental data. It has to be underlined that the thrust signals do not correspond to a constant discharge current since the current delivered by the SCs bank depends upon the load impedance which, in turn, depends upon the applied magnetic field strength and the mass flow rate. The T-I curves reported in Fig. 2.7 show the effectiveness of the applied magnetic field in increasing the thrust for a given discharge current. The thrust increases almost linearly with the discharge current for all the applied magnetic field strengths. This result indicates that the most important contribution to the thrust is the so called "swirl acceleration" which is expected to scale with IB_A as the directed azimuthal ion kinetic energy is converted into axial kinetic energy by conservation of the magnetic moment in a decreasing B-field. The

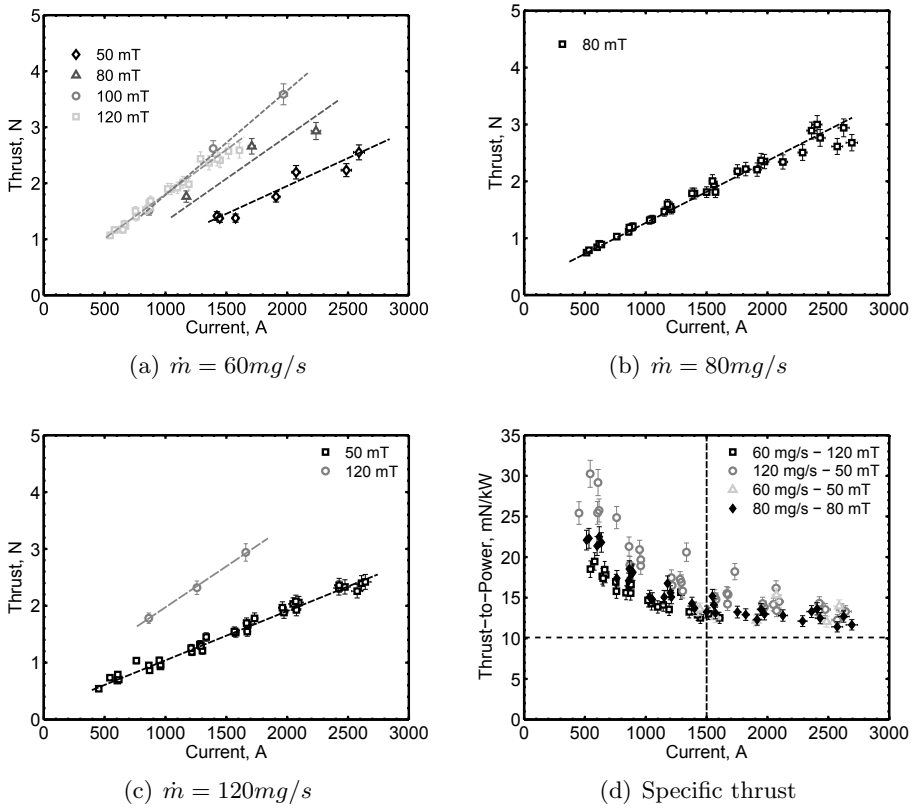

(a) $\dot{m} = 60mg/s$ (b) $\dot{m} = 80mg/s$

(c) $\dot{m} = 120mg/s$ (d) Specific thrust

Figure 2.7: Thrust measurements for different mass flow rates of Ar. Dashed lines are a guide to the eye.

thrust-to-power ratio shows that the thrust efficiency increases much slower than the specific impulse for increasing discharge current indicating that a larger fraction of the total arc power is lost to the electrodes. Moreover, the results suggest that at high current levels the specific thrust levels off at about 10 mN/kW independently of mass flow rate and magnetic field strength. As the power supply mass for a given thrust scales as $m_P \propto (T/P)^{-1}$, the results show that it may not be worthwhile to adopt high current levels since it may yield to a high power supply mass without significant improvements in thrust efficiency. The specific impulse and the thrust efficiency as a function of the discharge power are shown in Fig. 2.8. The increase in thrust efficiency with increasing arc power and applied field is shown to be more sensitive when the mass flow rate is reduced. This corresponds well to the theoretical prediction of the back-EMF voltage scaling $\sim IB_A^2/\dot{m}$, as recently shown by Lev [50]. Moreover, the thrust efficiency increases linearly with the specific impulse

and is slightly dependent on mass flow rates and B-field for a given I_{sp}.

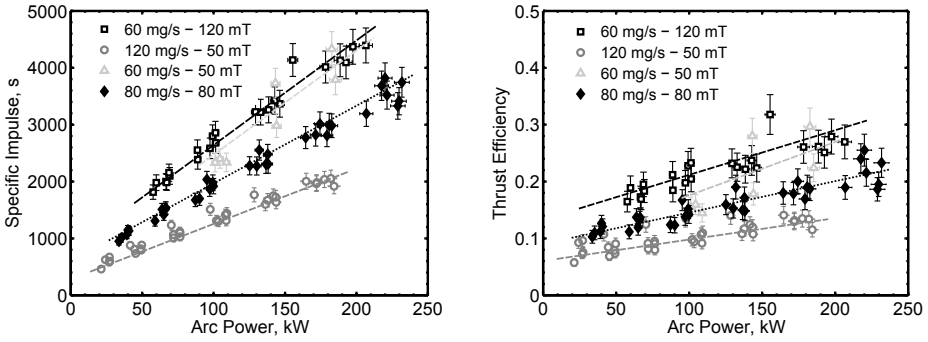

Figure 2.8: Thrust measurements for different mass flow rates of Ar. Dashed lines are a guide to the eye.

2.4 Cathode Operation

The post-test visual inspection performed after few hundred ignitions ($\simeq 500$) revealed that most of the erosion was localized at the main tube annulus. Moreover, as shown in Fig. 2.9, the cathode external surface showed current paths twisted in a helical fashion all along the cathode length indicating that the hollow cathode condition was not fully achieved. Provided that

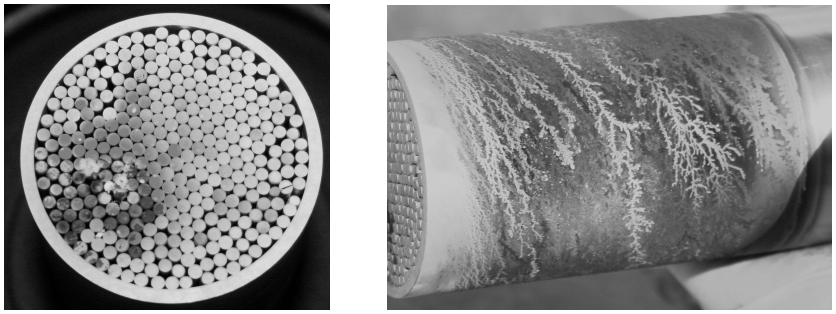

Figure 2.9: McHC frontal section (left) and helical current paths (right)

the external magnetic field has a component parallel to the cathode surface, the motion of the ignition sites deviates from random becoming increasingly directed with increasing magnetic field. Under the influence of an axially applied magnetic field, the arc spots rotate around the cathode as they travel down the length, leaving a trail of crater-like features arranged in an open

helical fashion as shown in Fig. 2.9. Since the azimuthal velocity is proportional to the axial magnetic field, $u_\vartheta \propto B_z$, the spot depth is expected to be lower at the cathode tip since, in this location, the time spent by the arc in each crater along its track is minimum. However, a high spot density is expected at the cathode tip since the pitch of the helix scales as $p \propto B_z^{-1}$. The time τ_h required to heat the cathode spot up to the melting temperature

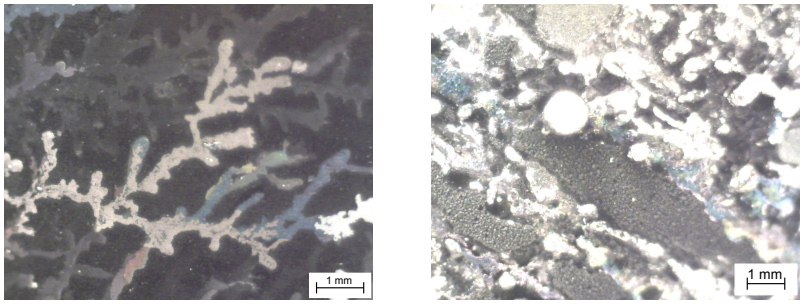

Figure 2.10: Close up of the McHC external surface for different cathode material. Molybdenum alloy (left), stainless steel (right)

$\Delta T \simeq 2500$ K is given by

$$2Q\sqrt{\tau_h} = \Delta T\sqrt{\pi\kappa^2/\delta}\,, \tag{2.1}$$

where Q is the heat power density, κ is the thermal conductivity and δ the thermal diffusivity. At the flux $Q = jV_c \simeq 10^{10}\ W/m^2$ on a molybdenum surface of radius $r_s \simeq 10^{-6}$ m, the characteristic time is $\tau_h \simeq 10^{-6}$ s, implying a frequency in the MHz range. Moreover, assuming a typical spot velocity of $u_s \simeq 10-15$ m/s, the mean spot displacement is in the order of 10^{-5} m. Since the estimated total length of the current track is $L_t \simeq 4$ m, the time required for the spot to move from the cathode tip to the thruster backplate $\tau_t \simeq L_t/u_s$ is approximately 0.2-0.3 s. The effect of the spot motion on different cathode materials is shown in Fig. 2.10. As suggested by Daadler [51] in his Joule heating model for hemispherical spots, the equilibrium crater radius scales as $r_s \propto I_e[\kappa \arccos(T_0/T_m)]^{-1}$ so that, for a given current I_e and local cathode temperature T_0, the mean spot dimension on a stainless steel cathode is expected to be higher by a factor $r_s^{SS}/r_s^{Mo} \simeq 2-4$. High-speed photography displayed a preference for attachment on the outer surface lasting for at least 0.1 s from the initial breakdown for most operating conditions. As shown in Fig. 2.11, after 0.4 s the current seems to attach mostly to the frontal cavities as expected during the hollow cathode operation. No significant variations of the terminal voltage were detected as a consequence of the different cathode operating modes. Moreover, Fig. 2.11 revealed that the number of ignited

channels increases with the discharge current undergoing a self-adaptation of the cathode cross section to the variable current requirements. However, inactive channels were observed at all the tested conditions, suggesting an oversizing of the cathode open cross section. Numerical analysis indicated

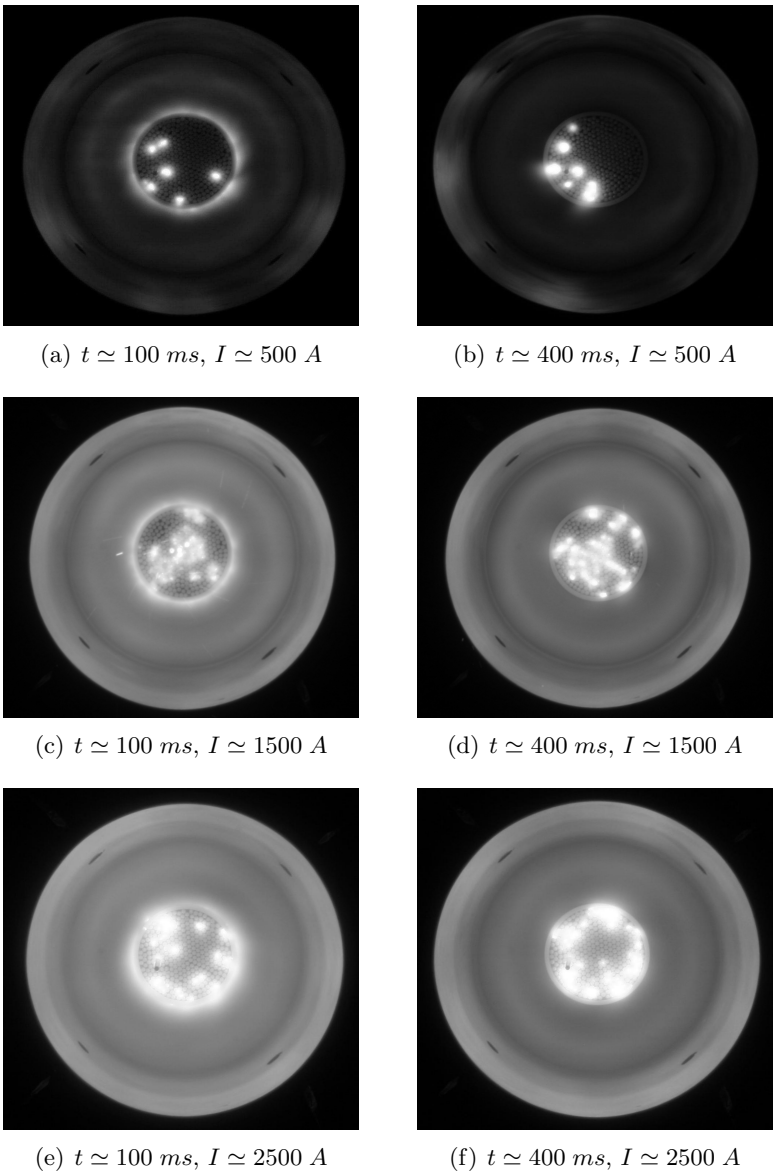

(a) $t \simeq 100\ ms$, $I \simeq 500\ A$ (b) $t \simeq 400\ ms$, $I \simeq 500\ A$

(c) $t \simeq 100\ ms$, $I \simeq 1500\ A$ (d) $t \simeq 400\ ms$, $I \simeq 1500\ A$

(e) $t \simeq 100\ ms$, $I \simeq 2500\ A$ (f) $t \simeq 400\ ms$, $I \simeq 2500\ A$

Figure 2.11: Thruster front view - $\dot{m} = 80\ mg/s$, $B_A = 80\ mT$

that the cathode approached an equilibrium temperature of about 2900 K

after $\tau_{eq} \simeq 10\ s$ from the initial breakdown. Since the discharge characteristic time, τ_d, was always much lower than the equilibrium time,$\tau_d \ll \tau_{eq}$, the cathode bulk remained cold ($< 1000\ K$) so that the thermionic current was at no point a significant fraction of the total discharge current. The current conduction was thus achieved through locally constricted arcs, even though it was not possible to resolve this phenomenon by the present experiment. Tracks of erosion craters left by the spots were found mainly at the cathode tip where the azimuthal component of the apparent spot motion is dominant. Some qualitative precedent for this finding is provided by Auweter-Kurtz [52] and Polk [53]. Since in pulsed applications the filling rods did not experi-

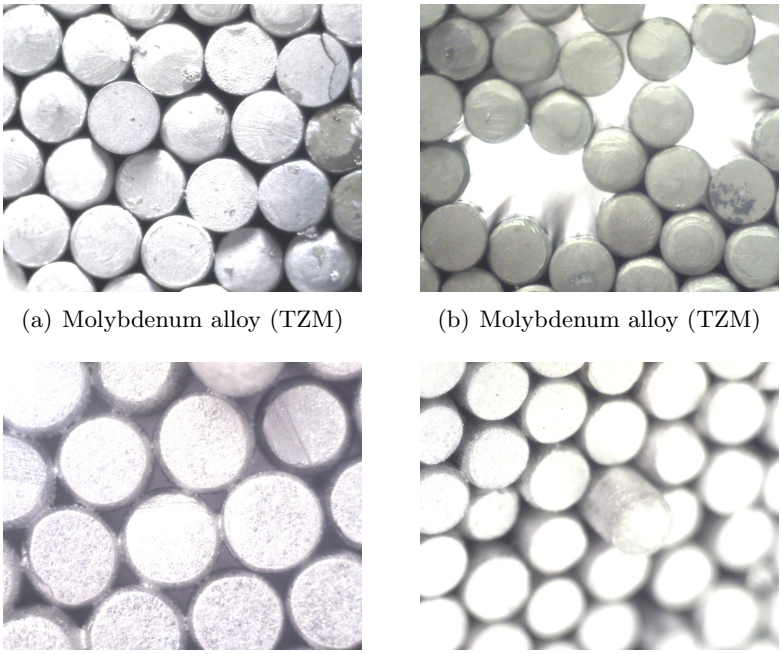

(a) Molybdenum alloy (TZM) (b) Molybdenum alloy (TZM)

(c) Stainless steel (AISI 316) (d) Stainless steel (AISI 316)

Figure 2.12: Close up of the McHC frontal surface

ence gross melting, the mechanical stability of the multi-channel pattern is questionable. Figure 2.12 shows the tungsten rods after few hundreds pulses for molybdenum alloy and stainless steel main tubes. Post-test inspections revealed that in both cases several rods were moved forward or even taken out of the pattern, probably due to thermal deformations of the outer tube combined with the propellant flow back-pressure. This effect was less evident for the stainless steel case, probably due to the fact that melted material was trapped beneath the rods fixing them together.

Chapter 3

MPD Thruster Theoretical Model

In order to assess the role of the electrode energy deposition on the thrust efficiency and lifetime, a theoretical model for the performance prediction of applied-field MPD thrusters was formulated. The validity of the model was then verified through a systematic comparison with the experimental data presented in Chapter 2 as well as with the data available in the literature. Finally, conclusions were drawn on the physics of the electrode power dissipation along with its scaling with respect to the thruster operational parameters.

3.1 Phenomenological Performance Model

The thrust produced by a SF-MPD thruster arises from the interaction between the radial component of the discharge current and the self-induced azimuthal magnetic field resulting in an axial thrust component described by the well-known Maecker [54] relation

$$T_{SF} = \frac{\mu_0}{4\pi}\left[\ln\left(\frac{R_A}{R_C}\right) + K\right] \cdot I^2 \ . \tag{3.1}$$

In the equation above the constant K takes a value between 0 and 3/4 depending upon the current attachment distribution over the cathode surface. For these devices the Lorentz force consists mainly of the gradient of the magnetic pressure $B_\vartheta^2/(2\mu_0)$ and is exerted primarily on the backwall of the acceleration chamber. Since $B_\vartheta \propto I$, at low discharge current the MPD thruster acts as an electrothermal device with a thrust component, T_{GD}, given by

$$T_{GD} = \dot{m} a_0 + p_C A_C \ , \tag{3.2}$$

where a_0 is the plasma sound speed and p_C is the pressure at the cathode exit section, A_C. At typical operating conditions of SF-MPD thrusters the electrothermal component is expected to be much smaller than the electromagnetic component [55] so that the overall thrust can be expressed as $T = T_{SF} + T_{GD} \simeq T_{SF}$. Nevertheless, equation (3.1) was shown to be often contradicted by experimental thrust measurements [56] since the thrust coefficient $C_T \equiv (4\pi/\mu_0)(T/I^2)$ is invariant with $I, \dot{m}$ and the type of propellant used. An improvement of the Maecker formula was suggested by Tikhonov [57] for a quasi-one-dimensional, isothermal plasma under the assumption of high magnetic Reynolds numbers, $R_m \gg 1$. In this condition the thrust coefficient is given by $C_T = [(\gamma + 1)/2] + 1/(2 \cdot A_0^2)$ where A_0 is the ratio between the magnetic pressure and the gasdynamic pressure at the cathode exit section, namely $A_0 = \left[B_\vartheta^2/(2\mu_0)\right] [\gamma A_c/(a_0 \dot{m})] \propto I^2/\dot{m}$. It is interesting to note that this expression is independent of the thruster geometry. As a result, the self-field thrust component can be written as

$$T_{SF} = \frac{\mu_0}{4\pi} \left[\frac{\gamma + 1}{2} + \frac{1}{2A_0^2} \right] \cdot I^2 \, . \tag{3.3}$$

Since the self-field magnetic force depends quadratically on the discharge current, the exhaust velocity u_e and the specific impulse I_{sp} are proportional to the parameter $\kappa = I^2/\dot{m}$. Therefore, it is of advantage to operate these thrusters at high current levels and low mass flow rate. Yet, from the early beginning of experiments with self-field MPD arcs, one surprising result has been the fact that for a fixed propellant and a given geometry of the electrodes, a maximum $I^2/\dot{m}$ exists beyond which undesirable effects occur, e.g. electrode ablation accompanied by terminal voltage fluctuations. Malliaris [58] and Devillers [59] emphasized the role played by Alfvén critical velocity u_A in the definition of the critical value $(I^2/\dot{m})_{crit}$ since it was found that applying the minimum power principle to a completely single ionized plasma and assuming a pure electromagnetic thrust mechanism, an analytical expression relating the maximum $\kappa-$parameter and the thruster operative condition can be written, namely

$$\kappa^* = \left(\frac{I^2}{\dot{m}} \right)_{crit} = \frac{u_A}{b} \, . \tag{3.4}$$

Furthermore, in conjunction with equation (3.1), equation (3.4) yields to an upper limit for the specific impulse which depends only on geometrical factors of the electrode arrangement and the kind of propellant. Even though Oberth [60] and Bruckner [61] demonstrated that u_A is not an ultimate limit of the attainable exhaust velocity, the specific impulse $I_{sp} \simeq u_A/g_0$ still remain a good approximation for the performance of self-field MPD thrusters.

When an external magnetic field is applied to create a field with meridional lines of force ($B_r/B_z \ll 1$, $B_A \simeq B_z$), two electromagnetic acceleration mechanisms are expected: the interaction of the azimuthal component of the discharge current with the applied magnetic field, T_H, and the interaction of the radial component of the discharge current with the applied field, T_{SW}. Since the electron Hall parameter scales as $\Omega_e = \omega_e \tau_e \propto B_A T_e^{5/2}/p_e$, for moderate applied fields the Hall contribution is small if compared to the swirl acceleration, $T_H/T_{SW} \sim B_r/B_z \cdot \Omega_e$ [22, 62]. As a consequence, it is possible to express the overall thrust produced by an applied-field MPD device as $T \simeq T_{SF} + T_{SW} + T_{GD}$. Which mechanism prevails in thrust production depends on the selection of operative parameters and thruster geometry. If the electromagnetic body force is predominant, the ions transmit thrust to the thruster body through a magnetic pressure force exerted mainly on the solenoid.

The interaction between the applied magnetic field and the discharge current results in azimuthal electromagnetic force. The directed azimuthal ion kinetic energy can be converted into directed axial kinetic energy by conservation of the magnetic moment and total ion energy in a decreasing B-field. As the magnetic field decreases, $B \sim r^{-2}$, so does the thermal energy perpendicular to the applied field in favor of the axially-directed energy. Such mechanism of thrust production was initially mentioned by Ellis [63] and Hess [64] without dwelling upon a model based on the rotational energy conversion. Later on this assumption was used as a basis for several theoretical efforts [65–68] aimed at deriving simple relations for the thruster performance. In particular, Fradkin [65] showed that the torque exerted by the interaction of the discharge current with the applied field within the acceleration chamber can be written as

$$T_r = \int_V (j \times B)_\vartheta \, dV = \frac{1}{2} B_A I R_C^2 \left(\bar{R}^2 - 1\right) \ . \tag{3.5}$$

Since the mechanical torque of a hollow cylinder is $T_r = 1/2 \dot{m} \omega R_C^2 \left(\bar{R}^2 + 1\right)$, the plasma angular velocity is given by

$$\omega = \frac{B_A I}{\dot{m}} \left(1 - \frac{2}{\bar{R}^2 + 1}\right) \ . \tag{3.6}$$

It is interesting to note that, for typical values of $I \simeq 10^3$ A, $B_A \simeq 10^{-2}$ T and $\dot{m} \simeq 10^2$ mg/s, the predicted plasma rotation frequency is $10^1 - 10^2$ kHz in good accordance with the experimental data presented by Allario [69] and Zuin [70]. When the plasma rotates as a rigid body [71], the axial thrust due

to a complete conversion of the azimuthal kinetic energy can be written as

$$T_{SW} = \sqrt{2\dot{m}\frac{d}{dt}\left(\frac{1}{2}i\omega^2\right)} = \frac{\bar{R}^2 - 1}{\sqrt{2\left(\bar{R}^2 + 1\right)}} B_A I R_C \ . \tag{3.7}$$

Equation (3.7) represents an upper limit for the swirl acceleration since only a fraction of the electrical power can be converted into rotational kinetic power. Moreover, the viscous forces in a collisional-dominated plasma reduce the efficiency of conversion from rotational to axial flow [65, 72]. Recent experiments have shown that the conversion factor to an ideal azimuthal acceleration is $0.2 \leq \xi \leq 0.5$ [73]. In the present analysis a $\xi \simeq 1/4$ was found to appropriately capture most of the experimental data. Since the applied-field to self-field thrust scales as B_A/B_{SF}, the overall thrust of an applied field MPD thruster can be expressed as

$$T = T_{SF} + \xi \cdot T_{SW} = T_{SF}\left(1 + f(\bar{R}, \xi, A_0)\frac{B_A}{B_{SF}}\right) \ . \tag{3.8}$$

The terminal voltage can be estimated as the sum of four contributions: the back-EMF voltage, the ionization and plasma heating voltage and the losses at the electrodes, namely

$$V = \sum_i V_i \simeq \frac{1}{I}\frac{T^2}{2\dot{m}} + \frac{1}{I}\frac{\left(q\varepsilon_i + 3/2 k_B T_e\right)\dot{m}}{m_i} + \varphi_a + \frac{5}{2}\frac{k_B T_{e,A}}{q} + V_A + V_C \tag{3.9}$$

where ε_i is the propellant first ionization potential, q is the elementary charge and φ_a is the work function of the anode. The plasma is assumed to be singly and fully ionized since the characteristic transit time τ is typically much lower than the characteristic recombination time τ_{rec}, namely $\tau \simeq L/v \ll (n_e\beta)^{-1}$. Multiple ionization, excitation and radiative processes are not included in the present model. The bulk electron temperature was taken to be 5 eV as measured by Serianni [74] over a wide range of discharge current and magnetic field values while the electron temperature at the anode sheath layer, $T_{e,A}$ was set at 2 eV as measured by Myers [75]. Moreover, the electron temperature was assumed to be constant with the discharge current as observed by Myers [76] and Randolph [77]. The cathode fall voltage was taken to be of the same order of magnitude of the propellant first ionization potential, $V_C \sim \varepsilon_i$[1].

In applied-field MPD thrusters the anode voltage drop was found to scale linearly with the current and the applied magnetic field [78–81]. This effect

[1] A more detailed cathode model is presented in Chapter 7.

is commonly attributed to the magnetization of the anode fall region. Nevertheless, since the ratio between the electron gyro radius to the Debye length is in the order of $10^1 - 10^2$, the anode sheath is unmagnetized. The effect of the magnetic field on the anode voltage is rather tied with the reduction in plasma density at the sheath edge due to the increase of the radial inward component of the thrust as measured by Serianni [74] and Gallimore [81]. In addition, the anode fall was found to drop with increasing propellant flow rate and reduced discharge chamber radius [82] corroborating the interplay between the plasma density depletion near the anode and the sheath voltage (*anode mass starvation*).
With this picture in mind, the anode fall voltage was determined assuming that the discharge current is carried to the anode by thermal electrons and ions thus neglecting the thermionically emitted electrons. The validity of this assumption is limited to pulsed, quasi-steady devices in which the characteristic discharge time, τ_d, is much lower than the anode heating time scale, τ_a, namely $\tau_a \simeq C_p m \Delta T / P_a \ll \tau_d$. Moreover, thermionic electrons need an extracting field to overcome the back-pulling force of the emitting surface so that the anode can actually deliver a net thermionic current only if the plasma potential is higher than the wall potential, $\Delta V = V_A - Vp < 0$, i.e. an electron-repelling sheath is needed [83].
Several authors have experimentally shown that this condition is verified in high-current arc discharges when the ratio of the available current from the plasma to the discharge current is of order unity or greater, namely $q\Gamma_e A_a / I \geq 1$ where $\Gamma_e = -D_\perp \cdot \partial_z n_e$ is the transverse electron flux [84–88]. As a matter of fact, measuring the anode fall voltage immediately after the startup and after that the anode had reached about 2300 K, Myers found no substantial differences in the near wall potential of the Princeton Benchmark Thruster operating between 15 kW and 30 kW [75]. Preliminary calculations based on Myers's experimental data have revealed a positive (electron-attracting) anode sheath lending credence to our understanding.

Under the previous hypotheses, the net current density from the anode, $j = I/A_a$, can be written as

$$j = j_{er} - j_i - j_{th} \simeq j_{er} - j_i < j_{sat} \ , \tag{3.10}$$

where j_i is the ion current density and j_{er} is the electron thermal flux collected at the anode surface and j_{th} is the thermionic current density. Assuming $V_p = 0$, from equation (3.10) it is possible to determine the voltage drop as

$$V_A = \frac{k_B T_{e,A}}{q} \left[\ln \left(\frac{\sqrt{m_i/m_e}}{0.61\sqrt{2\pi}} \right) - \ln \left(1 + \frac{j}{0.61 q n_S \sqrt{k_B T_{e,A}/m_i}} \right) \right] \ , \tag{3.11}$$

where n_S is the electron number density at the sheath edge.
It has to be noted that both Subramaniam [89] and Lev [90] have neglected the ion current density term in equation (3.11). This assumption is not fully justified since, as pointed out by Hügel [79], its contribution is essential to maintain the space-charge neutrality at the sheath edge as well as the heat flux at the anode surface. According to Merinov [83] the ion heating can account for 10-30% of the total anode heating power. In the present treatment the ion current density contribution was retained to assess its relevance to the anode sheath voltage drop. The anode fall voltage was shown to be related to changes in the electron number density nearby the electrode [86] and, since the electron density at the sheath edge is proportional to the transverse magnetic field, a relation between the plasma density and the thruster operative conditions must be found. The phenomenological approach taken here to evaluate the radial plasma number density variation is based on the work of Lev [90] and Niewood [91]. Using the MHD momentum equation in the radial direction, under the hypothesis of steady state operation, $\partial_t = 0$, and azimuthal symmetry, $\partial_\vartheta = 0$, it follows

$$m_i n \left(u_r \frac{\partial u_r}{\partial r} + u_z \frac{\partial u_r}{\partial z} - \frac{u_\vartheta^2}{r} \right) = f_r - \frac{\partial p}{\partial r} \, , \tag{3.12}$$

where $f_r < 0$ is the radial force density and $p = nk_B \left(T_e + T_i \right) = nk_B T$ is the local plasma pressure. Assuming a constant radial electron temperature and $u_z \gg u_r \simeq 0$, $u_\vartheta \gg u_r$ along with $\partial_z u_r \simeq 0$, it is possible to write

$$\frac{\partial n}{\partial r} = \frac{1}{k_B T} \left(f_r + m_i n \omega^2 r \right) \simeq \frac{nr}{k_B T} \left[q E_{0r} + \frac{m_i}{\dot{m}^2} B_A^2 I^2 f\left(\bar{R} \right) \right] \, , \tag{3.13}$$

which states that the radial force density, acting to pinch the plasma toward the thruster centerline, is balanced by the centrifugal force and the density gradient. Assuming that the radial force density scales as the thrust [11], it is possible to recast equation (3.13) as

$$\frac{\partial n}{\partial r} = -nr \left(k_1 B_A I + k_2 I^2 - k_3 B_A^2 I^2 \right) \, , \tag{3.14}$$

where $k_{1,2}$ are fitting coefficients. The integration of equation (3.14) between the thruster centerline and the anode radius leads to the following Gaussian profile

$$n_S = n_0 \exp \left[- \left(k_1 B_A I + k_2 I^2 - k_3 B_A^2 I^2 \right) R_A^2 \right] \, , \tag{3.15}$$

where the plasma density at the thruster centerline is estimated as $n_0 = k_4 \dot{m}$ meaning that an increase in mass flow rate leads to an increase in plasma density at all radial positions.

Fig. 3.1 shows the ratio between the plasma density at the sheath and the number density at the thruster centerline, $\xi = n_S/n_0$, along with the anode sheath voltage as a function of the discharge current and the applied magnetic field. The results suggest that both the discharge current and the applied magnetic field tend to pinch the plasma toward the thruster centerline reducing the plasma density nearby the anode surface of few orders of magnitude. As a consequence, the anode fall voltage increases almost linearly

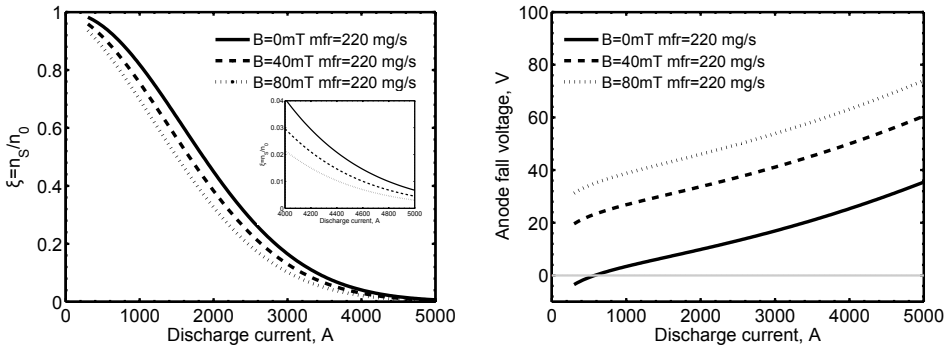

Figure 3.1: Radial number density contraction factor ζ and anode sheath voltage fall as a function of the discharge current and applied magnetic induction. Constants $k_1 = 0.2$, $k_2 = 2 \times 10^{-5}$, $k_3 = 0$, $k_4 = 5 \times 10^{18}$.

with increasing current and applied magnetic field. It is worthwhile to note that an electron-attracting anode sheath is predicted by the model for all the $B_A \neq 0$ conditions. For the present exemplary thruster ($R_C = 10$ mm, $R_A = 100$ mm) operating as a self-field accelerator, the anode sheath reversal occurs at about 600 A inhibiting the thermionic electron emission in almost all the operative conditions investigated.

3.2 Theoretical Results and Insights

The results of the semi-empirical model are here compared with the experimental data of two different thrusters: the 100-kW class AF-MPD thruster described in Chapter 2 and the so called Hybrid Plasma Thruster jointly developed by Alta and RIAME-MAI in 2001 [92].

3.2.1 Alta 100-kW

By analysis of the dependence of the thrust components on discharge current it was found that, for the present thruster design and operative regimes, the gasdynamic component can be neglected since $(T_{SF} + T_{SW})/T \geq 0.9$ and

hence the total thrust was calculated according to equation (3.8). Moreover, the maximum swirl to self-field thrust component is $(T_{SW}/T_{SF})_{max} \simeq 1 - 5$. The trend of a increasing terminal voltage with both applied magnetic field strength and discharge current is captured by the model as shown in Fig. 3.2. Results indicate that the back-EMF term accounts for $5\% - 30\%$ of the predicted terminal voltage while the anode contribution accounts for $15\% - 45\%$. Moreover, the satisfactory agreement between the theory and experiment, confirms the intricate scaling of the terminal voltage with the magnetic field and discharge current.

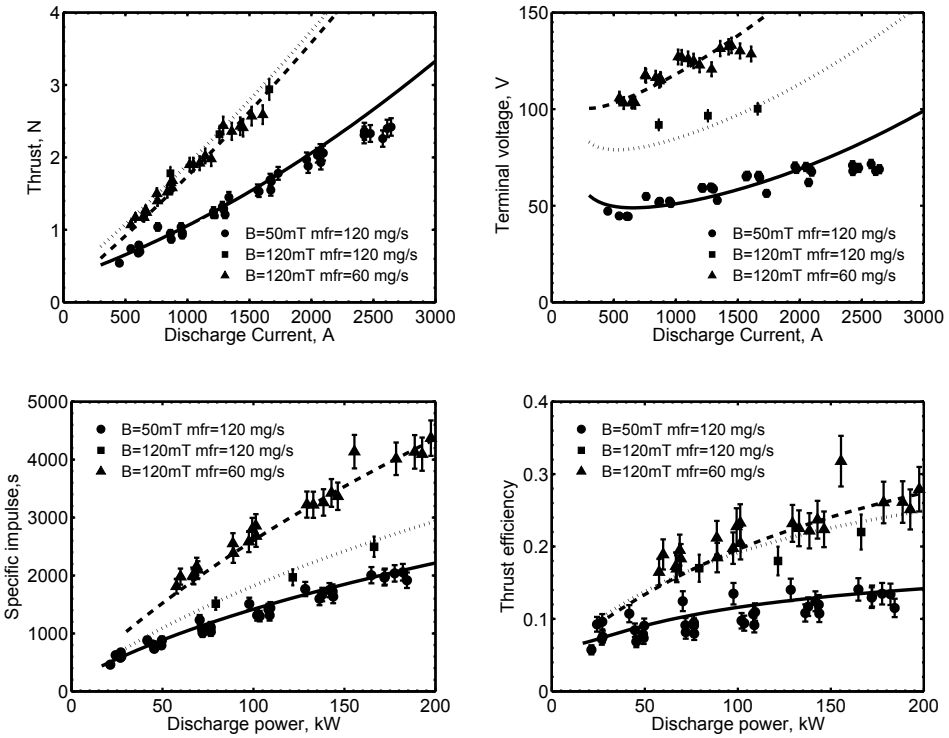

Figure 3.2: Theoretical and experimental thruster performance, $k_1 = 0.2$, $k_2 = 2 \times 10^{-4}$, $k_3 = 0$, $k_4 = 5 \times 10^{18}$

3.2.2 Hybrid Plasma Thruster

The Hybrid Plasma Thruster (HPT) is an axisymmetric MPD thruster with an applied magnetic field, a central acceleration chamber and a peripheral ionization chamber. The thruster has a central 20 mm in dia hollow cathode, an anode consisting of a cylinder 200 mm in dia and eight straps. The anode divides the central chamber from the ionization chamber where eight

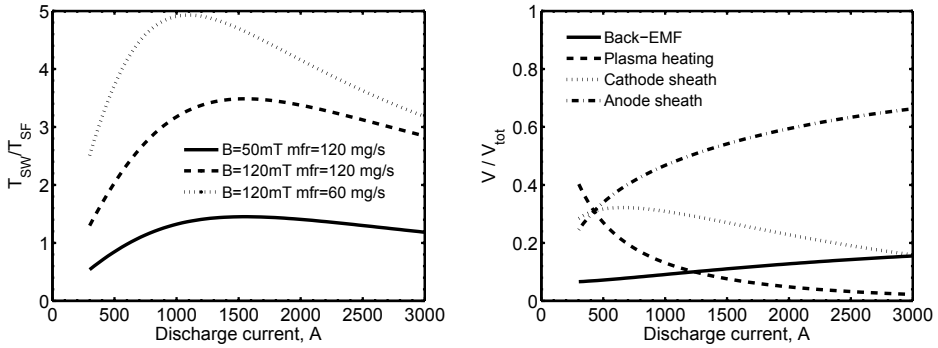

Figure 3.3: Applied-field to self-field thrust ratio and voltage apportionment for 50 mT, 120 mg/s

peripheral hollow cathodes 12 mm in dia are installed. The external solenoid is capable of producing an induction field up to 100 mT as measured at the thruster centerline. The aim of the peripheral chamber is to ionize a small fraction of the propellant by means of a secondary, low-power discharge between the peripheral cathodes and the anode. The ionized propellant then flows in the acceleration chamber, increasing plasma density near the anode. The thruster was operated in a pulsed, quasi-steady mode (pulse length up to 2.5 ms), with argon as propellant for instantaneous power inputs ranging from 100 to 450 kW.

The results reported in Fig. 3.4 demonstrated the effectiveness of applying an external magnetic field to increase the thrust as well as the thrust efficiency of MPD thrusters. The comparison with the thrust measurement data undoubtedly supports the model's scaling law, namely $T \sim B_A I$. For the HPT the back-EMF contribution to the total voltage drop was found to be less important than the plasma ionization and heating voltage, especially at low current levels. Since the thrust efficiency is given by $\eta_T = V_{emf}/V_{tot}$ this result indicates a very inefficient accelerating process where much of the input power is squandered at the electrodes ($9\% - 55\%$ to the anode and $18\% - 38\%$ to the cathode) and in resistive plasma heating ($8\% - 60\%$).

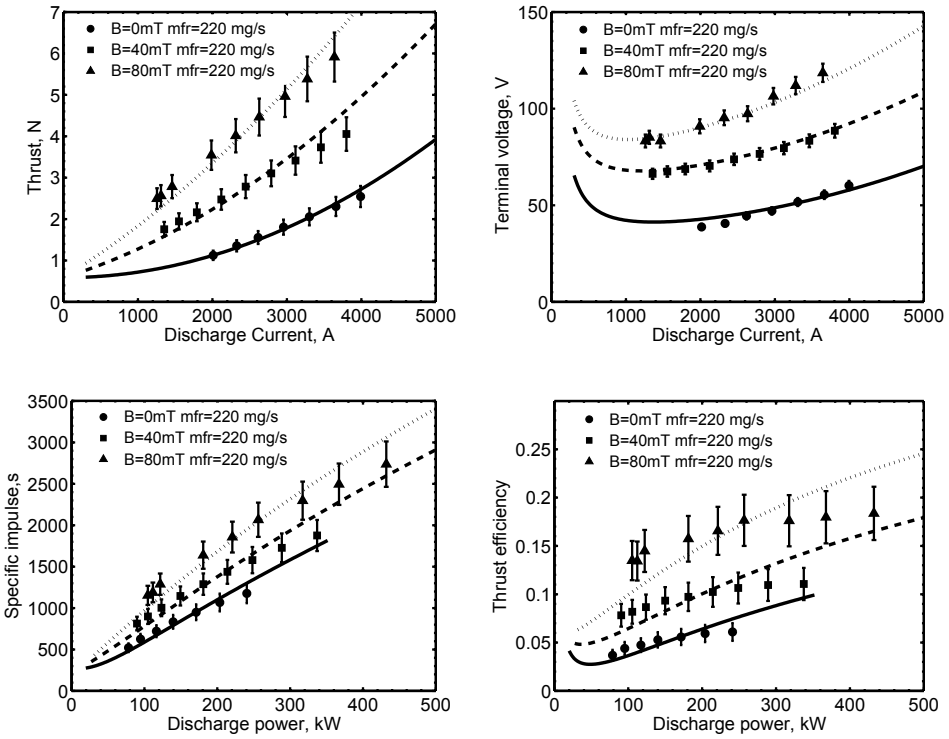

Figure 3.4: Theoretical and experimental thruster performance, $k_1 = 0.2$, $k_2 = 2 \times 10^{-5}$, $k_3 = 0$, $k_4 = 5 \times 10^{18}$

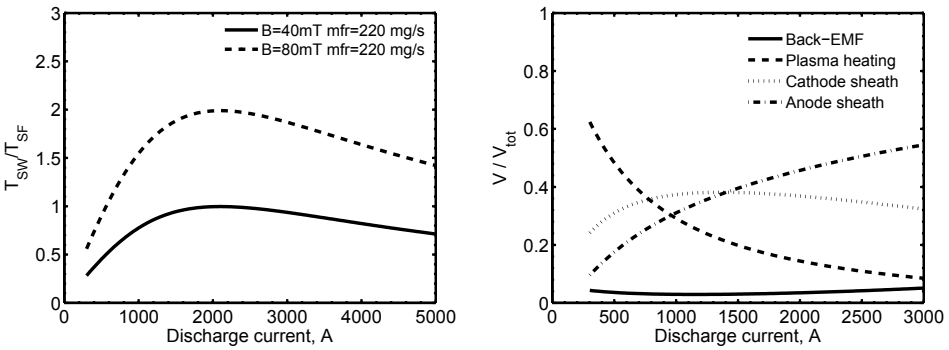

Figure 3.5: Applied-field to self-field thrust ratio and voltage apportionment for 80 mT, 220 mg/s

Part II

Physical Processes in Hollow Cathodes

Chapter 4

Electron Emission Physics

The role of the cathode as a part of the circuit is to serve as an interface between current conduction in the solid state and conduction in the plasma. Current continuity across this interface occurs primarily by the emission of electrons from the cathode surface to the discharge. Electron emission occurs when emissive materials are subjected to high temperatures T (thermal emission), applied electric fields F (field emission) or when photons provide sufficient energy to overcome the confining potential barrier. For thermal and photoemission, the extraction field is small compared to field-emission standards and a common approximation is that all the electrons with energy in excess of the barrier height are emitted (emission over-the-barrier). Conversely, field emission assumes that the thermal component is negligible and the tunnelling current is significant (emission through-the-barrier). In most applications, however, the electron emission tends to be a compromise between these mechanisms.

The present chapter will, therefore, provide a review of both thermal and field emission processes as modified by adsorption phenomena as well as in case of bare metals. A thermo-field emission equation is also provided given its relevance in the field of discharge cathodes for MPD thruster applications.

4.1 Thermionic Emission Fundamentals

Electrons in the conduction band of a metal behave according to Fermi-Dirac quantum statistics and have an energy distribution function (EDF) given by

$$f_{FD}(E,T) = \frac{1}{1+\exp\left[\beta\left(E-\mu\right)\right]}\,, \tag{4.1}$$

which describes the probability that a state of energy E will be occupied in thermal equilibrium at a temperature T, expressed as $\beta = 1/k_B T$. The chemical potential μ at temperature $T = 0$ is called Fermi energy, $\mu(T = 0\ K) = \mu_0 \equiv E_F$ and can be defined as the highest energy of occupied states at the absolute zero. For metals, the temperature dependance of $\mu(T)$ can be written as [93]

$$\frac{\mu}{\mu_0} \simeq 1 - \frac{1}{3}\left(\frac{\pi}{2\mu_0\beta}\right)^2 - \frac{1}{5}\left(\frac{\pi}{2\mu_0\beta}\right)^4 . \tag{4.2}$$

As can be seen in Fig. 4.1, even at 3000 K, $\mu/\mu_0 \simeq 0.998$ so that, for any practical use, the temperature dependance of μ can be neglected and taken as interchangeable with E_F. Since the Fermi energy depends only on the electron density, namely $E_F \propto n_e^{2/3}$, the highest occupied energy level in the conduction band depends upon the cathode material. It is evident that the

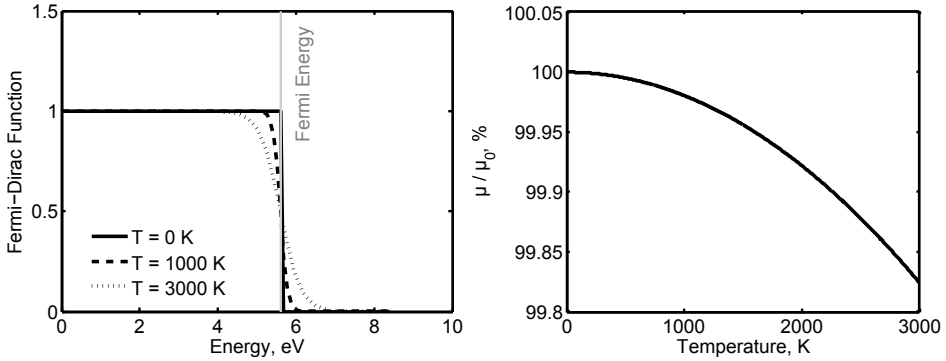

Figure 4.1: (left) Fermi distribution function versus electrons energy at different temperatures. (Right) Normalized chemical potential versus surface temperature.

EDF differs from its zero temperature value only in a small region about E_F of width a few $k_B T$. Moreover, according to the Fermi-Dirac statistics, only a small fraction of electrons can acquire energies above the Fermi level even at high surface temperatures. Notwithstanding the high values of energy of some electrons at 0 K, they remain within the metal, since forces exerted

by the positive ions and by other free electrons prevent them from escaping. To overcome the above-mentioned attractive forces, an energy equal to E_v (also called *vacuum level*) is needed for an initially-at-rest electron. For electrons already possessing a kinetic energy equal to the Fermi level, a smaller energy, $E_v - E_F$, is required. As a consequence, it is assumed that all the electrons striking the surface with a normal component of the velocity z greater than $z_0 = (2E_v/m_e)^{1/2}$ can actually leave the metal, thus contributing to the thermionic current. By letting $1/2m_e z^2 = E_n$, the normal energy, and $N(E_n)dE_n$ the number of electrons moving to the surface having normal energies between E_n and dE_n, it is possible to write the Fermi-Dirac distribution as [94]

$$N(E_n) = \frac{4\pi m_e}{h^3} k_B T \log\left\{1 + \exp\left[-\beta\left(E_n - E_F\right)\right]\right\} . \tag{4.3}$$

As shown in Fig. 4.2 at absolute zero, $N(E_n)$ is a linear function of the energy while at higher temperatures $N(E_n)$ decreases gradually above E_v. By forming the integral of $N(E_n)dE_n$ between the limits $E_n = E_v$ to $E_n \to \infty$, the electron current per unit area can be expressed by the following relation

$$j_T = 2\frac{2\pi k_B^2 m_e q}{h^3} T^2 \exp\left[-\beta\left(E_v - E_F\right)\right] = 2AT^2 \exp\left(-\frac{\varphi_0}{k_B T}\right) , \tag{4.4}$$

where the gap between the Fermi level and the top of the potential well is called *work function*, namely $E_v - E_F = \varphi_0$. Equation 7.3 holds only for $E_v - E_F \gg k_B T$, which is usually the case in high-current cathodes. It

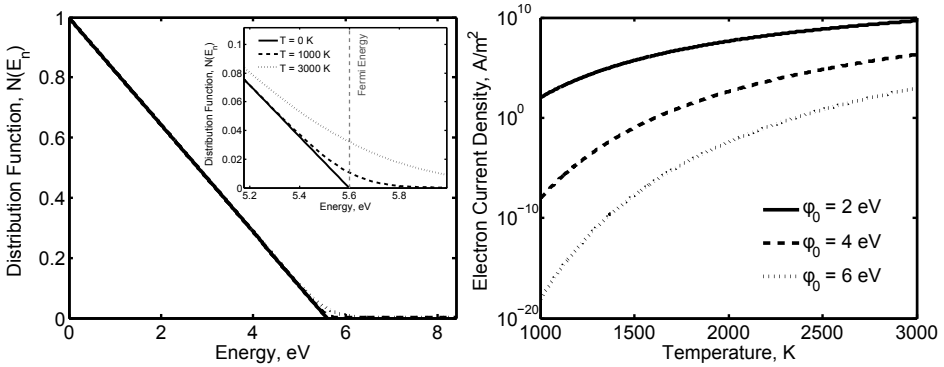

Figure 4.2: (left) Normalized distribution function $\tilde{N}(E_n)$ versus electrons energy at different temperatures. (Right) Thermionic current density for different work function values.

is worth noting that the well-known Richardson-Dushman (RD) relation in

equation (7.3), exclusively depends upon the barrier height, so that the RD equation is independent of whether a rectangular, triangular or image charge potential barrier is used. Moreover, it was assumed that the potential barrier is uniform throughout the surface and hence effects of atomic modulation, crystallographic structure and direction were neglected [95]. Because of these simplifications, the experimental values of the constant A vary widely.

4.1.1 The Value of A in Thermionics

A finite metallic volume may be modeled as a potential well. As shown by Fowler [96], according to the wave mechanics, not all the electrons in the metal reaching the surface with a normal energy greater than E_v will escape since a certain fraction will be reflected back. The emission equation must, therefore, be multiplied by the so called *transmission probability*, T_{p_x} defined as the ratio between the transmitted and incident current densities for a given momentum $p_x = \hbar k = \sqrt{(2m_e E)}$. Conservation of particles across a potential barrier demands that $j_{trans} + j_{ref} = j_{inc}$ so that $T_{p_x} = 1 - R_{p_x}$, where R_{p_x} is the reflection probability. Therefore, equation (7.3) can be written as

$$j_T = 2AT^2 \exp\left(-\frac{\varphi_0}{k_B T}\right) = \underbrace{2A(1-\bar{R}_p)}_{A_G} T^2 \exp\left(-\frac{\varphi_0}{k_B T}\right), \tag{4.5}$$

where $\bar{R}_p$ is the average of R_{p_x} over a Maxwellian distribution. The mean value of $\bar{R}_p$ depends upon the temperature and the topology of the potential distribution on both sides of the surface boundary. The discontinuous slope of potential Nordheim [97] used in his computations led to a value $\bar{R}_p = 1/2$; in this case $A_G = A$ again. For a continuous slope, namely an infinite potential step, $\bar{R}_p \simeq 0$ for $E_n/E_v > 1$ so that

$$A_G \simeq 120 \cdot 10^4 \; A \; m^{-2} \; K^{-2} \; .$$

It is known from experiments that the value of A_G depends to a great extent on the chemical purity of the surface. As will be shown later on, adsorption of electropositive elements decreases the value of A_G, whereas adsorption of electronegative elements increases the value. Experimentally found values for A_G depend upon the state of the surface and vary for niobium in the range $(57 - 120) \cdot 10^4$ and for hafnium from $14 \cdot 10^4$ to $22 \cdot 10^4$ [98]. Measurements on pure metals, however, gave values for A_G in the neighborhood of $1 \cdot 10^6 \; A \; m^{-2} \; K^{-2}$ [99].

Since the chemical potential varies with the temperature, the work function was found to vary almost linearly with the temperature, $\varphi = \varphi_0 + \gamma T$ [100]. Thermionic emission capabilities of surfaces are thus expressed by an effective

work function φ at a particular operating temperature, assuming a constant A_G factor, or by a constant work function φ_0 with the temperature dependance subsumed by the coefficient $D = A_G \exp(-q\gamma/k_B)$, which is typically $D < A_G$. Henceforth, the work function is assumed to be temperature-independent.

4.1.2 The Nature of the Work Function

Charges redistribute in materials, primarily by building up at the surface, to shield out externally applied fields. For metals the process is remarkably efficient due to the high number of conduction band electrons. This redistribution of the electrons at the surface occurs over short length scales, typically tens of Å, and is sufficient to keep the surface equipotential in the presence of a charged external object. Classically, such a redistribution is accounted for assuming that an equal-in-magnitude but opposite-in-sign charge exists below the surface at the same distance as the charged object. This approach is known as *image charges* method [101]. In this classical approach, the force felt by the external electron at a distance x from the metal surface due to its image charge is given by $F_i = q^2/[4\pi\varepsilon_0 (2x)^2] \equiv Q/x^2$, implying that the work required to remove the electron to infinity is Q/x. Such classical image-charge potential figures strongly in the origins of the work function since, due to this force, the energy E_v is higher than E_F.
It is possible to demonstrate that the electrostatic charge density at the surface of a metal does not drop sharply but in an exponential manner, thus forming a dipole layer [93], which is the origin of the electron confining force, see Fig. 4.3. Somorjai showed that total potential height can be divided into three contributions corresponding to the potential between core and valence electrons U_c, the exchange potential between valence electrons U_{ex} and the surface dipole potential U_d, namely $U = U_c + U_{ex} + U_d$ [102]. Even though the debate about whether the work function can be considered a surface property or a bulk property is still flourishing among researchers [104, 105], the previous considerations lead to a definition of the work function that includes both bulk and surface properties of the emitter, namely $\varphi_0 = U - U_F = U_{bulk} + U_d$. As it will be described in Section 4.3, the presence of an adsorbed layer of foreign atoms can substantially affect the work function of the substrate, due to the modification of the charge distribution at the emitter surface and thus of the dipole potential U_d. Moreover, the dipole potential of the bare metal, being tied with the distance between the ion cores, can be different for different crystalline surfaces, as shown by Brodie [106]. As a matter of fact, the work function is a strongly anisotropic property and an averaged value over the different surface orientations (effective work function) is commonly employed [107].

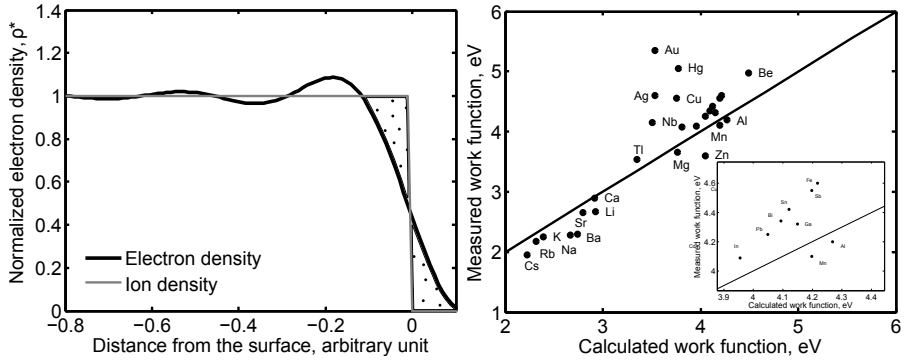

Figure 4.3: (left) Distribution of the electronic charge density at the surface of a metal. (Right) Measured work function versus calculated as done by [103].

For any practical engineering applications, Halas [103] showed that the effective work function of a bare metal can be related to its density parameter r_s and to the Fermi energy E_F using the following semi-empirical equation:

$$\langle \varphi_0 \rangle \simeq 43.46 \frac{\alpha}{r_s^{3/2} E_F^{1/2}} \ , \tag{4.6}$$

where $r_s = (3/4\pi n_e)^{1/3}$ is expressed in Bohr radius, $E_F \simeq 50.1/r_s^2$ is in units of eV and α is a scaling factor equals to unity for all elements except the alkali metals for which $\alpha \simeq 0.86$. The quality of this approximation is shown in Fig. 4.3 using values for the work functions from the CRC tables [99].

4.1.3 Electron Emission in Accelerating Fields

If an electric field F, giving a constant force $W = qF$, is applied at the surface, the effective work function decreases. With reference to Fig. 4.4, using a linear approximation for the applied field force, the total potential distribution perpendicular to the surface can hence be written as

$$U(x) = \varphi_0 - \frac{q^3}{16\pi\varepsilon_0 x} - eFx \ . \tag{4.7}$$

The maximum of the potential barrier is thus given by $\partial_x U(x) = 0$, so that it can easily be shown that the potential high is given by

$$\varphi_S = \varphi_0 - \sqrt{\frac{q^3 F}{4\pi\varepsilon_0}} = \varphi_0 - \Delta\varphi_S \ . \tag{4.8}$$

By inspection of equation (4.8) it is clear that an external applied electric field reduces the work function leading to a higher electron emission. The

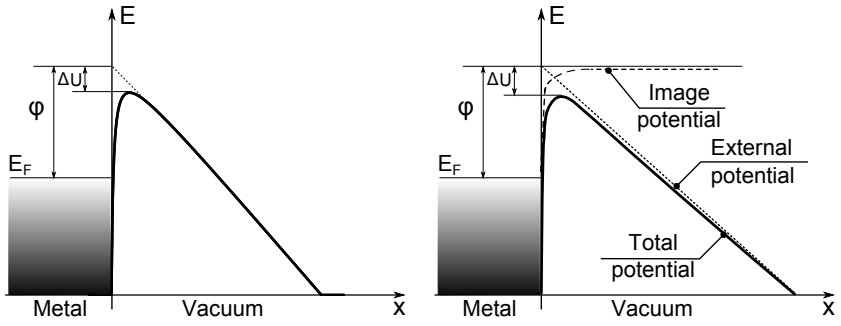

Figure 4.4: Potential barrier for electrons at the surface of a metal and Schottky effect

lowering of the image charge barrier by the application of a field relates to the shifting of the electron density profile of a quantity δx that can be found by demanding global charge neutrality [108]. Nevertheless, the previous equation holds if the correction term is much smaller that the original work function, $\Delta\varphi_S/\varphi_0 \ll 1$ since, at still higher electric field, the thickness of the potential barrier becomes so small that electrons can tunnel through it even at $T = 0\ K$. Assuming $\Delta\varphi_S/\varphi_0 \simeq 1/10$, an electric field strength of about $10^8\ V/m$ should be considered as the validity upper limit for equation (4.8). In the limiting case of low surface temperatures, the field emission process can be described by the so called Fowler-Nordheim equation

$$j_F = \frac{q^3}{8\pi h\varphi_0 t^2(y)} F^2 \exp\left[-\frac{8\pi\sqrt{2m_e\varphi_0^3}}{3qhF} v(y)\right], \tag{4.9}$$

where $t(y)$ and $v(y)$ are elliptical functions whose numerical values have been listed by Burgess [109]. When both high temperature and electric field are present at the surface of a metal, the emission current density can be several orders of magnitude higher than the sum of the thermionic and field emission, namely $j_{TF} > j_T + j_F$ [110], where j_{TF} identifies a different emission mechanism named thermo-field (TF) emission. One of the main applications of this mechanism lies in the field of high-current cathodes, where temperatures of few thousand degrees and electric fields in the order of $10^6 - 10^7$ V/m are typical during steady-state operations. In addition, the thermo-field emission mechanism is predominant during the thruster start-up phase or during pulsed applications when the current conduction is accomplished through luminous spots where the temperatures at the arc root are often in excess of the material melting point and the electric fields can be as high as 10^{10} V/m [111].
According to Murphy and Good [112], the thermo-field emission current den-

sity j_{TF} is related to the surface temperature T, the electric field E and the work function of the material φ_0 by the following relation

$$j_{TF} = \int_{-E_a}^{\infty} D(E,W) \cdot N(W,T,\varphi_0)\, dW \ , \tag{4.10}$$

where $-E_a$ refers to a constant ground state potential in the emitter, $D(E,W)$ is the electron tunneling probability across the potential barrier at the surface and $N(W,T,\varphi_0)$ is the Fermi-Dirac energy distribution function of the electrons moving towards the surface. Due to the complexity of the previous equation, the prediction of the thermo-field current densities implies the use of numerical methods. Approximate formulae of the Murphy and Good formalism exist in the literature even though their use is restricted to defined ranges of temperature and electric field and is only given for few cathode materials. Hantzsche [113] developed a number of additive and harmonic combinations of thermionic and field emission formula such as

$$j_{TF} \simeq \left(\bar{A}T^2 + \bar{B}F^{9/8}\right) \exp\left[-\left(\bar{C}T^2 + \bar{D}F^2\right)^{-1/2}\right] \ , \tag{4.11}$$

where j_{TF} is in units of A/cm^2, T in K, F in V/cm while $\bar{A} = 174\ A/cm^2\,K^2$, $\bar{B} = 174\ A/cm^{7/8}\,V^{9/8}$, $\bar{C} = 3.667{\cdot}10^{-10}\ K^{-2}$ and $\bar{D} = 2.352{\cdot}10^{-18}\ cm^2/V^2$, while Jüttner [114] suggested the following simple equation for the T-F emission

$$j_{TF} \simeq A \cdot Y^2 \exp\left(B\frac{\varphi_0}{Y}\right) \ , \qquad Y = T + C\frac{E}{\sqrt{\varphi_0}} \ , \tag{4.12}$$

where $A = 5 \cdot 10^6$, $B = -1.19 \cdot 10^4$ and $C = 1.49 \cdot 10^{-6}$, referring to SI units. The equations above hold for $\varphi_0 \simeq 4.5\ eV$, $T \simeq 10^3 \div 10^4\ K$ and electric field in the $10^8 \div 10^{10}\ V/m$ range. The Murphy and Good equation is assumed to be the most accurate relationship for the prediction of the electron emission current of cold cathodes [115].

4.2 Theoretical Model for Thermo-Field Emission

Theoretical developments of the TF emission theory for metals were presented by Murphy [112], Christov [116] and Jensen [117] and later experimentally verified in the intermediate region between thermionic and field emission by Christov [118]. Nevertheless, no accurate and simple formula for the emitted current density in the typical range of temperatures, electric fields and work function of MPDT cathodes is yet available. To this purpose, a general approach for the TF emission based on the standard Sommerfeld model of free electrons is developed starting from the work of Petrin [119] .

A simple Schottky barrier is assumed to confine the electrons of the conduction band in the metal, see Fig. 4.5. The barrier is described by the potential energy

$$U(x) = \begin{cases} \varphi_0 + E_F - q^2/(16\pi\varepsilon_0 x) - qFx, & \text{if } x > \tilde{x} \\ 0, & \text{if } x \leq \tilde{x} \end{cases} \tag{4.13}$$

where F is the externally applied electric field and $\tilde{x}$ is the smaller root of the equation $\varphi_0 + E_F - q^2/(16\pi\varepsilon_0 x) - qFx = 0$. The energy of the electrons in the metal directed along the normal to the boundary is given by $E_x = p_x^2/(2m_e)$. The probability that an electron incident on the barrier will overcome the potential well or tunnel through is given by the transmission probability $T(p_x) = j_{trans}/j_{inc}$. The emission current density is thus the integral over

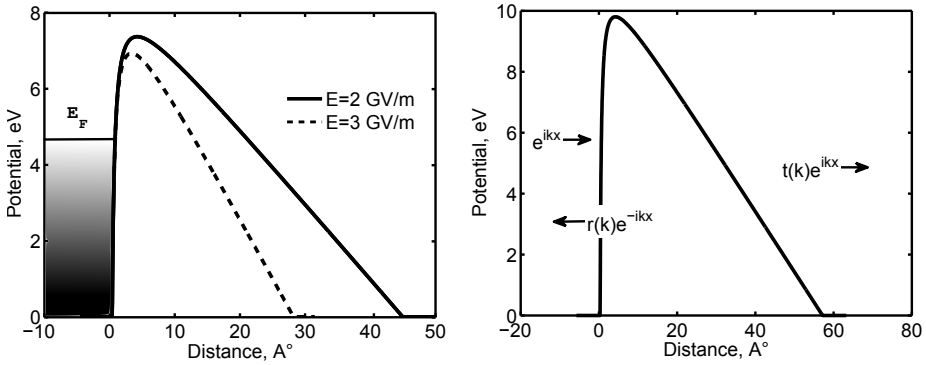

Figure 4.5: Schematic of the potential barrier and effect of the external electric field.

the energy distribution of the number of electrons escaping from a unit surface per unit time, namely

$$\begin{aligned} J &= \frac{q}{m_e} \int_0^\infty T(p_x) p_x f(p_x) dp_x \\ &= \frac{4\pi q m_e k_B T}{h^3} \int_0^\infty T(p_x) \left\{1 + \exp\left[-\beta\left(E_x - E_F\right)\right]\right\} dE_x \,, \end{aligned} \tag{4.14}$$

where $f(p_x)$ is the supply function. A similar expression for the surface power density can be written to include the energy exchange during the electron emission, namely

$$Q_S = \frac{4\pi m_e k_B T}{h^3} \int_0^\infty T(p_x) \left(E_F - E_x\right) \left\{1 + \exp\left[-\beta\left(E_x - E_F\right)\right]\right\} dE_x \,, \tag{4.15}$$

where Q_S is negative when the surface is cooled by the electron emission and positive when is heated (Nottingham effect).
In order to evaluate the integrals of equation (4.14) and (4.15), the transmission coefficient for a standing electromagnetic wave through a finite potential barrier must be found. Across the barrier, the wave function satisfies the time-independent, one-dimensional Schröedinger equation given by

$$-\frac{\hbar^2}{2m_e}\frac{d^2\psi}{dx^2} + U(x)\psi = E_x\psi \ , \tag{4.16}$$

where $U(x)$ is the potential energy and E_x is the directed kinetic energy. Since, far from the barrier, the potential energy is constant and equal to zero, equation (4.16) has a plane-wave solution in the form $\psi = \exp(ikx)$. It is thus possible to write the reflected and transmitted waves far from the barrier as

$$\psi_r = r\exp(-ip_o x/\hbar) \ , \qquad \psi_t = t\exp(ip_x x/\hbar) \ , \tag{4.17}$$

where $p_0 = \hbar k_0$ is the particle momentum component along the x axis of the incident wave having a wave vector k_0 while r and t are the reflection and transmission coefficient, respectively. Taken a finite-difference approximation of the derivatives at the grid points $x_n \in [0, \tilde{x}]$, equation (4.16) can be recast as

$$\psi_{n+1} - \left[\frac{2m_e}{\hbar}(\Delta x)^2 U(x_n) + 2 - \frac{2m_e}{\hbar}(\Delta x)^2 E_x\right]\psi_n + \psi_{n-1} = 0 \ , \tag{4.18}$$

which has to be solved for the unknown function $\psi(x)$ with the left-side boundary condition given by

$$\psi_0 = \psi_1 \exp\left(\frac{ip_0\Delta x}{\hbar}\right) + \exp\left(\frac{ip_0 x_0}{\hbar}\right)\left[1 - \exp\left(\frac{2ip_0\Delta x}{\hbar}\right)\right] \ , \tag{4.19}$$

and the following right-side boundary condition

$$\psi_{N+1} = \psi_N \exp\left(\frac{ip_x\Delta x}{\hbar}\right) \ . \tag{4.20}$$

Since the Schottky barrier is such that $U(x_0) = U(x_N) = 0$, the energy of the incident electrons from the left does not change during the motion through the barrier, thus $p_0 = p_N$. Solving the linear system $[M]\cdot\{\psi\} = \{B\}$, it is thus possible to evaluate the transmission probability as

$$T(p_N) = \frac{p_N}{p_0}|t|^2 \Rightarrow T(p_N) = \left[\psi_N \exp(-ip_0 x_N/\hbar)\right]^2 \ . \tag{4.21}$$

4.2.1 Results

In order to assess the validity of the model with respect to both experimental data and accepted models, solutions of equation (4.14) and equation (4.15) are presented in a range of temperatures, electric fields and work functions relevant for MPDT applications, namely $T \simeq 1000 \div 4000\ K$, $F \simeq 10^7 \div 10^{10}\ V/m$ and $\varphi_0 \simeq 2 \div 5\ eV$. Since the model was conceived to describe the electron passage through a triangular barrier, the pure thermionic case, $F = 0$, cannot be properly modeled so far. Moreover, as the electric field decreases, the potential barrier tends to a Heaviside function leading to a wobbling solution.
Figure 4.6 shows the effect of the external electric field as well as of the work function on the transmission probability. As expected, the increase in electric field or the reduction in the work function lead to an increased escaping probability for a given electron energy. However, while changes in the work function yield to a shape-preserving shifting of the transmission probability, the effect of the applied electric field is more involved reflecting the response of the electric field on the barrier height and thickness. Figure 4.7 shows the dependence of the emission current density on the electric field on a tungsten surface ($E_F = 4.5\ eV$) for two different surface temperatures. The modulus of the thermal power density $|Q_S|$ released on the surface during the electron emission is also reported. The $j_{TF} - E$ curve clearly shows a

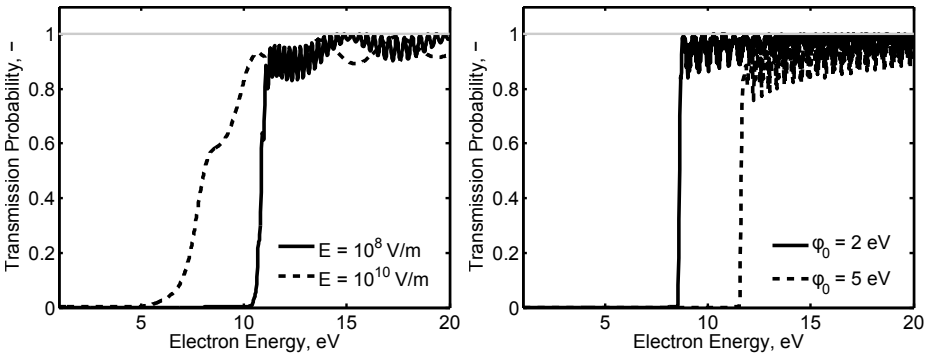

Figure 4.6: Transmission probability for different electric fields and work functions

temperature-dependent regime and a field emission regime up to the electron current saturation level. In the first regime the thermionic electron emission is a significant fraction of the total current density and the curves approach the values predicted by the Richardson-Dushman equation for $E \to 0$. At higher electric fields, say $E > 10^9\ V/m$, the emission through the barrier is

predominant leading to a temperature-independent regime. It is interesting to note that, unlike the equations for pure thermionic and field emission, a saturation current density of about $2{\cdot}10^{15}\ A/m^2$ is predicted by the model. In the saturation regime the barrier height becomes lower that the bottom of the conduction band and a local explosive emission (spot) is much likely to occur. This phenomenon was experimentally verified by Dyke [120] and Dolan [121]

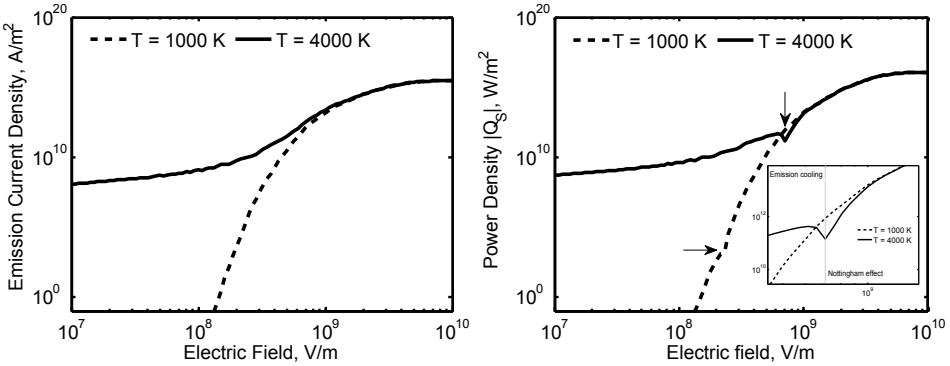

Figure 4.7: Emission current density and modulus of the power density for $\varphi = 4.5\ eV$

who found stationary modes at current densities up to $10^{11}-10^{12}\ A/m^2$ while for higher current densities an explosive destruction of the emitting material was observed and they speculated that the resistive heating was sufficient to locally melt the emitter at the critical current density. To investigate this hypothesis, the thermal power density released on the surface during the emission process was calculated. Figure 4.7 shows that the cooling capacity reaches a maximum after which a sharp transition from thermionic cooling to surface heating takes place. This phenomenon occurs when the external electric field exceed a given threshold, E^* and is due to the replacement of the emitted low energy electrons by electrons from higher energy states (Nottingham effect). The effect of the work function on both the emission current and the power density is shown in Figure 4.8. Moreover, it was found that the critical electric field scales as $E^* \propto T$ suggesting that a possible way to delay the inception of local explosive phenomena is to allow for a full warm-up of the cathode to support thermionic emission before the discharge. Heated cathodes are, indeed, used in a number of pulsed vacuum devices and have also been tested in quasi-steady MPD thrusters. As a matter of fact, Paganucci showed that heating the cathode prior to each firing the damage appeared to be substantially reduced in depth and number than the case with no heat addition [122].

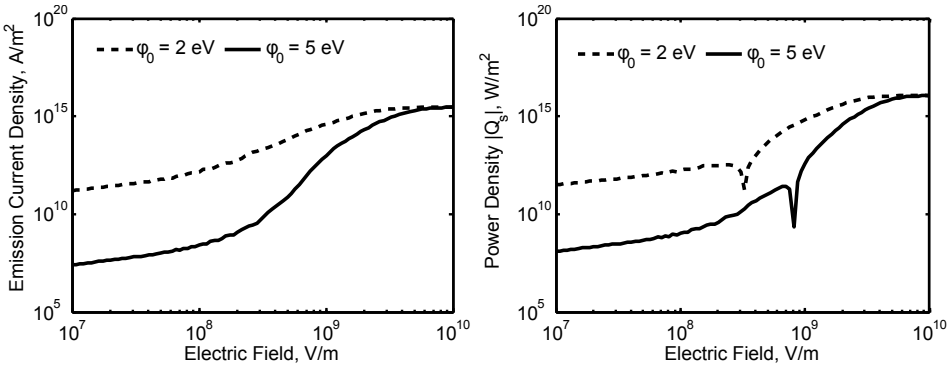

Figure 4.8: Emission current density and modulus of the power density for $T = 4000\ K$

The experimental results give credence to the hypothesis that the triggering mechanism for explosive heating is the reduction of the potential barrier height below the Fermi energy so that, unlike previous analysis, no Joule effect is here invoked. Figure 4.9 compares the numerical results with the

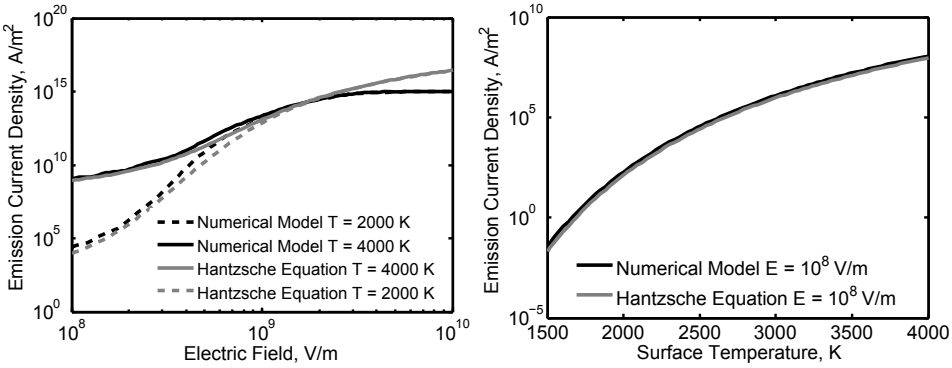

Figure 4.9: Comparison between the numerical model and the Hantzsche equation

Hantzsche semi-empirical equation for tungsten emitters. The numerical method describes the thermo-field emission process with a reasonable level of accuracy for a wide range of surface temperatures and external electric field strengths. Moreover, it was found that for typical operative conditions of steady-state cathodes, e.g. $T \simeq 2500 \div 3000\ K$ and $E \simeq 10^6 \div 10^7\ V/m$, thermionic emission with Schottky correction is a fairly good approximation of the emission process while for quasi-steady, pulsed devices, a thermo-field emission mechanism must be taken into account. Results of the numerical

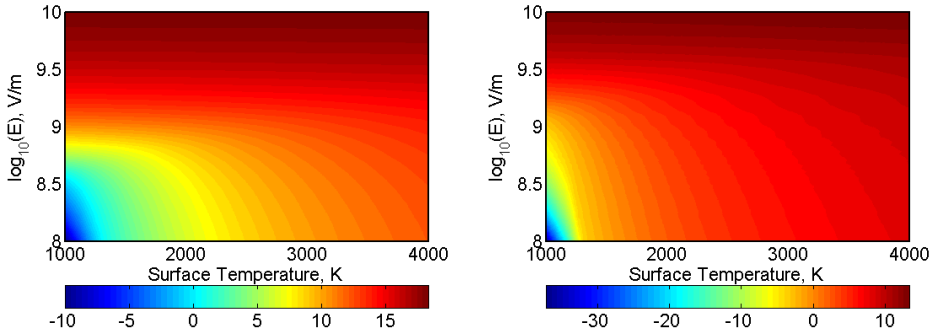

(a) Murphy-Good (b) Numerical Model

Figure 4.10: Comparison between the Murphy-Good (left) and the numerical electron current density (right) for $\varphi = 4.5\ eV$

evaluation of equation (4.10) and equation (4.14) for a $\varphi = 4.5\ eV$ metal are presented in Fig. 4.10. As expected, the emission current density tends to become independent from the electric field for $E \lesssim 3 \cdot 10^8$ V/m and independent from the temperature for large fields, say $E \gtrsim 3 \cdot 10^9$ V/m. Figure 4.11 shows $j_{TF}/j_T = k$ isocontours in the temperature-electric field plane. The low-temperature, low-field region is poorly defined and led to odd j_{TF}/j_T ratios. Good agreement between the Richardson-Dushman equation and the numerical models can be found only for $T > 2000$ K and $E < 3 \cdot 10^8$ V/m, namely in the thermionic emission region. It was predictable, thus, that moving towards the field emission region the discrepancy became more and more pronounced. Nevertheless, both the Murphy-Good formalism and the numer-

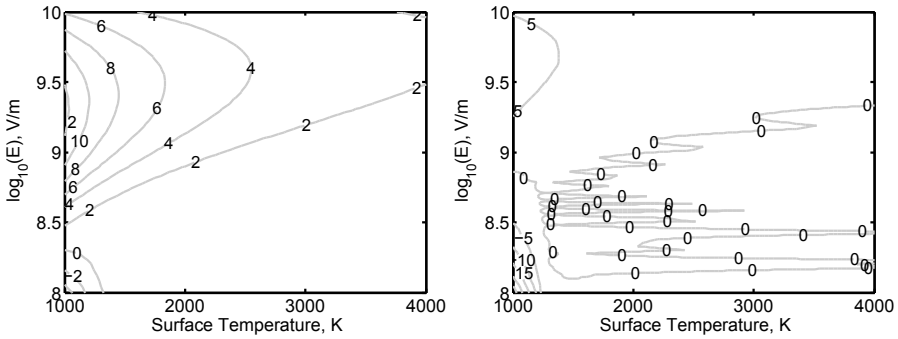

Figure 4.11: Isocontours j_{TF}/j_T in the $T - \log_{10}(E)$ plane for the Murphy-Good equation (left) and the numerical model (right)

ical model show that the Richardson-Dushman equation underestimates the

thermo-field emission current density of about $20-40\%$ at high temperatures and up to 200% at high electric fields.

4.3 Low-Work Function Coatings

Considering the different electron emission processes, cathodes are generally classified as thermionic or non-thermionic, depending upon their ability to sustain the high temperatures needed for thermionic emission without considerable melting or evaporation. In light of the previous definition, the distinction between refractory and non-refractory cathodes can be made calculating the ratio of the flux of vaporized atoms Γ_n to the flux of thermionically emitted electrons j_T/q, namely

$$\zeta = \frac{q\Gamma_n}{j_T} = \frac{p_v/\sqrt{2\pi m_s k_B T_w}}{4\pi m_e k_B^2 T_w^2 \exp\left(-q\varphi_0/k_B T_w\right)/h^3} \ , \tag{4.22}$$

where T_w is the cathode wall temperature, p_v is the vapor pressure at temperature T_w, m_S is the atomic mass and φ_0 is the work function of the bare material. Clearly, the lower is ζ the better suited is the cathode material for thermionic operations. A material can be thus considered suitable for thermionic cathodes if $\zeta \leq 1$. Equation (4.22) can be rewritten considering

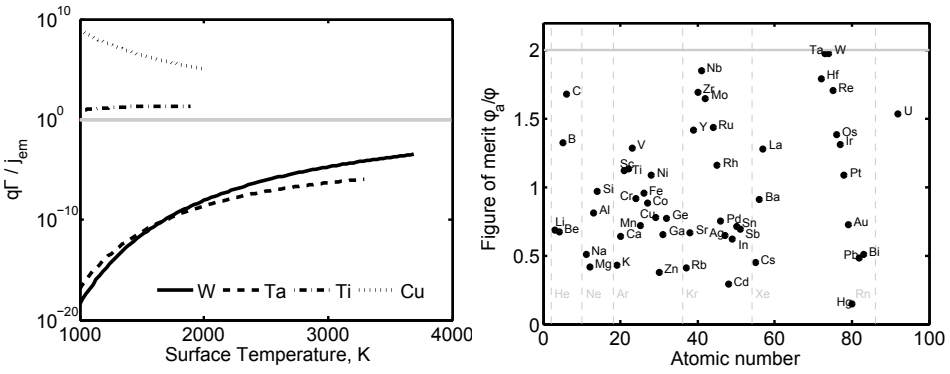

Figure 4.12: ζ-parameter and ξ-parameter for different cathode materials

that both electron emission and neutral evaporation are thermally activated processes and thus described by Arrhenius equations having the form

$$\nu = Q \exp(-H/kT) \ ,$$

where Q is a pre-exponential factor that includes the number of permissible paths over the barrier of energy H, the number of times per second each particle attempts to surmount the barrier and the number of particles in the

potential well at any time. Since $H \gg kT$ for the processes to be considered, the exponential term is very strongly dependent on temperature while Q is a relatively weak function of temperature [123]. Combining the Richardson-Dushman equation with the relation for the evaporation rate, it is possible to identify a figure of merit ξ for the elementary emitters given by

$$\xi = \frac{\varphi_a}{\varphi_0} = \frac{\ln\left(Q/\nu_a\right)}{\ln\left(A_R T^2/j_T\right)} \,, \tag{4.23}$$

where φ_0 is the work function of the bare material and φ_a is the *cohesive energy*, defined as the energy needed to remove an individual atom from its bonded position in the solid to an isolated position at infinite distance. In any practical application ν_a must not exceed some maximum permissible value and j_T must be above some minimum usable value so that the highest is ξ the better suited is the cathode material for steady-state high current applications. Values of ξ for different elements are shown in Fig. 4.12 in which the data for φ_0 and φ_a listed by Anders [98] were used. By inspection of Fig. 4.12 an apparent natural limit seems to exist, $\xi < 2$. As shown by Rasor [124] and Gadzuk [125], the origin of such a limit can be investigated by considering the equilibrium among the transition energies at the surface (Born-Haber cycle). With reference to Fig. 4.13, the energy required to

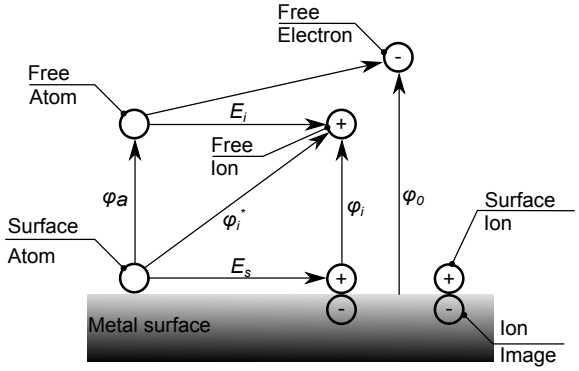

Figure 4.13: Born-Haber cycle for the transition energies at the surface

convert an atom on the surface to a free ion is given by $\varphi_i^* = E_S + \varphi_i$, where E_S is the electron binding energy while φ_i is the so-called ion work-function. However, a free ion can be obtained through ionization of a desorbed atom so that $\varphi_i^* = \varphi_a + E_i - \varphi_0$, where $-\varphi_0$ is the energy needed to bring a free electron to its bonded state on the surface. Since the net energy change must be zero,

$$\varphi_0 = \varphi_a + E_i - \varphi_i - E_S \,.$$

Assuming $\varphi_i \simeq \varphi_0$, the previous relation can be recast as $\varphi_a \simeq 2\varphi_0 - (E_i - E_S)$. Since the ionization energy is always greater than the binding energy at the surface, $E_i > E_S$, the figure of merit writes

$$\xi = \frac{\varphi_a}{\varphi_0} \simeq 2 - k \,, \qquad k > 0 \,, \tag{4.24}$$

explaining the upper limit of Fig. 4.12. This result implies that elementary emitters have an inherent short lifetime at thermionic temperatures due to the occurrence of significant evaporation. As a consequence, elementary emitters seem to be not suitable for long-lasting operation as discharge cathodes in steady-state MPD thrusters. Since the cohesive energy is an intrinsic property of the bulk material, the only way to increase the ξ parameter and, thus, the cathode lifetime, is to reduce the work function by employing a layer of foreign atoms adsorbed on the elementary surface. The rest of this chapter is, therefore, devoted to a careful investigation of the effects of non-metallic atoms deposition on the lifetime of elementary emitters.

4.3.1 Work-Function of Surfaces with Adsorbed Layers

Although the effect of the adsorption of activator particles on metal surfaces has been studied long ago starting from the pioneering work of Kingdon and Langmuir [126], the actual mechanism leading to variations of the substrate work function is not yet fully understood. In the field of alkali-metal adsorption, the existing paradigm is based on the Langmuir-Gurney model (LG) [127] which represents the first quantum-mechanical treatment of the problem. The LG model predicts a partial charge transfer from the alkali metal adsorbed atoms (adatoms) to the substrate at very low coverage while, as the coverage increases, its foresees a mutual depolarization of the adsorbed atoms due to their reciprocal electrostatic interaction. Thanks to its qualitative agreement with the measured work function curves and its relatively simple physical picture of the absorbtion process, the LG model was unquestioned for more that half a century. However, recent theoretical and experimental works casted doubts upon the validity of the LG treatment since the predicted increase in the chemical bondlength as the coverage changes from sub-monolayer to monolayer levels was found to be substantially incorrect [128–131]. As a consequence, computationally intensive physical models based on the density function theory (DFT) were developed and validated in the last years to gain a deeper insight into the basic nature of the adsorption process [132, 133]. However, since the purpose of the present work is to give a general picture of the basic cathode processes without dwelling upon the intricate field of the condensed-matter physics, the qualitative analytical models developed some 40 years ago seem to be the most practical

compromise between including details and keeping the treatment computationally reasonable. All these models assume that an electric dipole is formed at the adsorption site thereby modifying the work function of the substrate. Moreover, because of their relevance to the cathode technology, most of the semi-empirical models developed in the past years employed transition metals as substrates.
Among them, the phenomenological approach developed by Gyftopoulos and Levine (GL) [134] gives rather good agreement with experimental data for a large variety of adsorbate-substrate sets. This model accounts for dipole and dipole-dipole proximity effects on the magnitude of the work function even if questions remain about its interpretations. According to the GL model the work function variation with coverage owes its existence to differences in electronegativity W and dipole effect d so that

$$\varphi(\vartheta) = W(\vartheta) + d(\vartheta) \; . \tag{4.25}$$

The $W(\vartheta)$ term is taken to be the simplest polynomial that fulfills the boundary conditions, namely for $\vartheta = 0$ the work function is that of the bulk material φ_0 and for $\vartheta = 1$ the work function is that of the adsorbate φ_c. Moreover, small variations of the degree of coverage around $\vartheta = 0$ and $\vartheta = 1$ are assumed to not change the work function barrier. Thus,

$$W(0) = \varphi_0 \qquad \lim_{\vartheta \to 0} \partial_\vartheta W = 0 \qquad W(1) = \varphi_c \qquad \lim_{\vartheta \to 1} \partial_\vartheta W = 0 \; . \tag{4.26}$$

The simplest polynomial expression that satisfies the boundary conditions (4.26) is a cubic given by

$$\begin{aligned} W(\vartheta) &= \varphi_c + (\varphi_0 - \varphi_c)(1 + 2\vartheta)(1 - \vartheta)^2 \\ &= \varphi_c + (\varphi_0 - \varphi_c)H(\vartheta) \; . \end{aligned} \tag{4.27}$$

The derivation of the dipole term $d(\vartheta)$ is somewhat more involved and assumes that the dipole moment $M(\vartheta)$ between two atoms is proportional to the difference in their electronegativities W even at the surface, $M(\vartheta) \propto (W(\vartheta) - W(1))$. With reference to Fig. 4.14, the atoms are represented by hard spheres in a square array with an adsorbed atom (adatom) at the apex of the pyramid. The distance from the center of the substrate atoms w and the adatom c is indicated with R while the angle between the line joining the atom centers and the vertical axis is designated β. Denoting M_{wc} the dipole moment between the atoms and considering that for the four dipoles only the components parallel to the vertical axis survive, the total dipole for the group is given by $M_0 = 4M_{wc}\cos\beta$. Using the Gordy-Thomas relation between electronegativities and work function of a pure metal, a relation in the

form $M_{wc} \propto (\varphi_0 - \varphi_c)$ can be written. In particular, the Gyftopoulos-Levine model suggests that $M_{wc} \simeq 19\varepsilon_0(\varphi_0 - \varphi_c)$ so that the dipole term is

$$M(\vartheta) = 4\varepsilon_0 r_0^2 \cos\beta(\varphi_0 - \varphi_c) \ , \tag{4.28}$$

where a constant radius parameter $r_0 \simeq 4.36$ Å is introduced. The $\cos\beta$ term

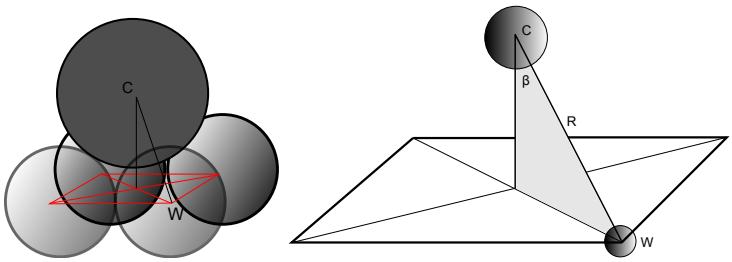

Figure 4.14: Schematic of coverage atoms atop a layer of bulk atoms

can be deduced from geometrical arguments regarding the configuration in Fig. 4.14, namely $\sin^2(\beta) = 2/n_w(r_w/R)^2$ where $n_w/(2r_w)^2$ is the number of substrate atoms per unit area, $n_w \simeq 1$ is a dimensionless parameter interpretable as the number of atoms per unit cell and r_w is the covalent radius of the substrate atoms. Since the total dipole moment $M(\vartheta)$ is diminished by the depolarizing effect of the adjacent dipoles, the GL model introduces the Topping's formula [135] to account for this phenomenon,

$$M_e(\vartheta) = M(\vartheta) - \alpha E(\vartheta) \ , \tag{4.29}$$

where $\alpha = 4\pi\varepsilon_0 n r_c^2$ is the polarizability, n accounts for the electronic shell structure of the atom and r_c is the covalent radius of the adsorbate atoms. Note that α for a real polarized atom is expressed as the rank 2 tensor α_{ij}. Nevertheless, since the electric field near a metal surface is predominantly along the surface normal (equipotential surface), only the dipole perpendicular to the surface effectively determines the momentum so that $\alpha_{zz} = \alpha$. The depolarizing field $E(\vartheta)$ is calculated as the electric field acting on a dipole within an infinite array of charge images. If interactions between image charges are neglected, the electric field $E(\vartheta)$ is given by

$$E(\vartheta) = \frac{9}{4\pi\epsilon_0}\left[\frac{n_f}{(2r_c)^2}\right]^{3/2} M_e(\vartheta) \ , \tag{4.30}$$

where, analogous to n_w, n_f is number of adsorbate atoms per unit cell at monolayer coverage. Since the dipole term is given by $d(\vartheta) = n_c M_e(\vartheta)\vartheta$, the

following relation can be used

$$\begin{aligned} d(\vartheta) &= -M_e(\vartheta)\left[\frac{n_f}{(2r_c)^2}\right]\frac{\vartheta}{\varepsilon_0} \\ &= -\frac{M(\vartheta)}{1+\dfrac{9\alpha}{4\pi\varepsilon_0}\left[\dfrac{n_f}{(2r_c)^2}\vartheta\right]^{3/2}}\left(\frac{n_f}{\varepsilon_0(2r_c)^2}\vartheta\right) . \end{aligned} \tag{4.31}$$

Combining equation (4.27) with equation (4.31), the expression for the work function in terms of the degree of coverage can be written as

$$\frac{\varphi(\vartheta)}{\varphi_c-\varphi_0} = \frac{1}{1-\varphi_0/\varphi_c} - (1-\vartheta)^2(1+2\vartheta)G(\vartheta) , \tag{4.32}$$

where

$$G(\vartheta) = 1 - \frac{n_f(r_0/r_c)^2\left[1-2/n_w(r_w/R)^2\right]\vartheta}{\left[1+n(r_c/R)^3\right]\left[1+9n/8(n_f\vartheta)^{3/2}\right]} = \frac{a\vartheta}{1+b\vartheta^{3/2}} . \tag{4.33}$$

While n depends on whether the covering is alkali ($n = 1$) or alkali-earth ($n \simeq 1.65$), the two parameters n_w and n_f remain to be determined empirically according to the specific adatom-substrate system under consideration. However, these two parameters are not independent, since the substrate atoms provide the surface onto which the adsorbate atoms nestle. Clearly, the number of adatoms per number of substrate atoms in a cell depends on the nature of the adsorbate and on the crystal plane. Gyftopoulos introduced a quantity N_0 to describe the crystal face and argued that in a body-centered cubic (bbc) crystal having a Miller index of [100], $N_0 = 1$ while $N_0 = 2$ corresponds to the [110] face and $N_0 = 3$ corresponds to everything else. On sintered tungsten surfaces and dispenser cathodes, the best representation is to use $N_0 = 3$. As a consequence, the GL model suggests that the quantities $n_f/\sqrt{N_0}$ and $n_w/\sqrt{N_0}$ are approximately constant from one face to another, so that the constraint between n_f and n_w is given by

$$\frac{n_w}{n_f}\left(\frac{r_c}{r_w}\right)^2 = \begin{cases} 4, & \text{for Cs on W, Mo, Ta...} \\ 2, & \text{for Ba on Sr, Th, W...} \end{cases} . \tag{4.34}$$

Since the GL model captures some features of the adsorption effect on the work function rather easily, it still retains most of its original appeal but it is not without complications. The assertion that $\varphi(\vartheta)$ can be expressed as the sum of a dipole and an electronegativity barriers is quite dubious since Schmidt and Gomer were able to describe the work-function reduction with increasing ϑ without including electronegativity effects [136, 137].

Moreover, the interpretation of the data is a bit ambiguous since the experimental values of ϑ reported in the literature are usually inferred by assuming a linear relation between the deposition time and the degree of coverage so that experimental errors can alter the estimate of ϑ. Figure 4.15 compares

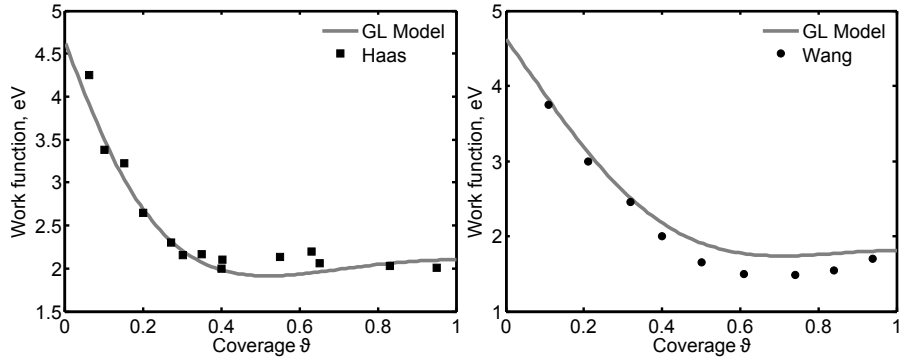

(a) BaO-W (b) Cs-W

Figure 4.15: Comparison of experimental data compared to the GL model

the experimental measurements reported by Haas [138, 139] and Wang [140] for barium on tungsten and cesium on tungsten, respectively. Using the values for $n_f/\sqrt{N_0}$ and $n_w/\sqrt{N_0}$ suggested by Jensen [141], the predicted work function is in remarkably good agreement with the experimental data. However, it has to be underlined that there is no established method to compare different coverage measurements and the reproducibility of the data via independent measurements is scarce. As a matter of fact, since the surface coverage is not directly observable in practical use, it is necessary to correlate typical global properties such as the substrate temperature and the activator partial pressure with the degree of coverage. A rather straightforward way to determine a relation for $\vartheta = f(p_g, T_w, T_g)$, is to define a proper adsorption isotherm for the phenomenon under investigation. Thus, using the expression for $\varphi = g(\vartheta)$, a direct relation between the cathode operating conditions and the effective work function can be finally established.

4.3.2 Adsorption Isotherms

Any surface exposed to a gas is subjected to impingement of the constituent atoms. An early approximation for the mass flux impinging a surface was developed by Hertz and Knudsen, assuming that the gas and the surface is in thermal equilibrium [142]. From the kinetic theory of gases, the impingement rate is given by

$$\dot{n}_a = \frac{p}{\sqrt{2\pi m_g k_B T_g}} \,, \tag{4.35}$$

where p is the background pressure of the gas, m_g is its mass and T_g its equilibrium temperature. Assuming that all the arriving gas atoms stick to the surface, the characteristic time needed to cover an initially clean surface is given by $\tau_{ML} \simeq n_\sigma/\dot{n}_a$, where n_σ is the number of available adsorption sites per unit area, typically $n_\sigma \simeq 10^{19} - 10^{20}\ m^{-2}$. Typical values for the impingement rate and monolayer formation times are shown in Fig. 4.16 for Xe and He in a range of temperature between 1000 and 4000 K. Since hollow cathodes typically operate at internal pressures in the order of 10^2 Pa, a characteristic time of about $10^{-6} - 10^{-5}$ s is needed to completely cover the initial surface even at high temperatures. Nevertheless, the fractional surface

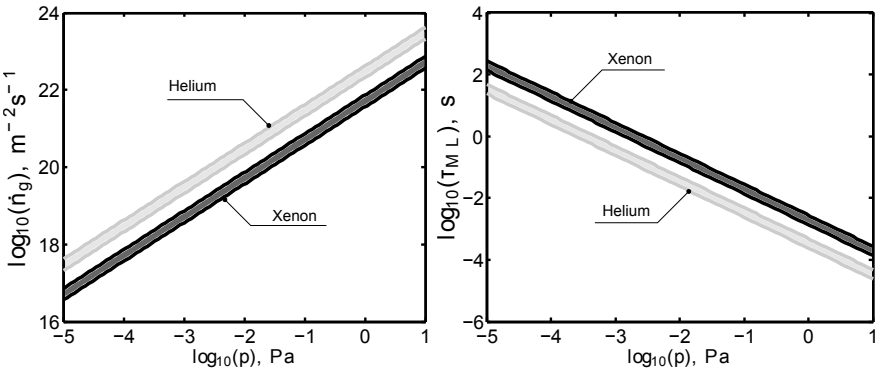

Figure 4.16: Typical impingement rates and monolayer formation times for Xe and He between 1000 K and 4000 K

coverage in steady-state conditions $\vartheta = n_a/n_\sigma$ can be determined by equating the adsorption and the desorption rates for a given surface temperature, namely $\dot{n}_a = \dot{n}_d$. The desorption rate can be derived starting from the trapping probability of the impinging atom in the Lennard-Jones potential well. As shown by Kurkmans [143], a trapped atom has a probability of escape from a given potential depth E_d given by

$$\nu_d = \nu_0 \exp\left(-E_d/k_B T_w\right) , \tag{4.36}$$

where $\nu_0 \simeq 10^{13}\ s^{-1}$ is the attempt frequency and T_w is the temperature of the surface atoms. Note that $E_d \neq \varphi_a$ since the cohesive energy is the difference between the average energy of the bulk atoms of a crystal and that of the free atoms, while the desorption energy is defined as the potential energy difference required to remove an adsorbed particle from the composite surface in the form of a free atom and depends on the interaction between the foreign atom with the surface atoms.
According to the depth of the potential well, it is possible to distinguish

between physical adsorption or physisorption and chemical adsorption or chemisorption [144]. Physisorption in caused by weak Van der Waals forces between the adsorbed gas and the solid surface, while chemisorption involves chemical bond formation due to rearrangement and transfer of electrons between the interactive gas and the solid surface. Typical chemisorption energies are $0.6 - 4\ eV/atom$ that compares to $0.05 - 0.4\ eV/atom$ for physisorption. A transition between these types of adsorption processes is thus customarily set to about $0.5\ eV/atom$ [145]. Note, however, that the above definition is over-simplified and somewhat arbitrary since molecules or atoms are often distorted when adsorbed on solid surfaces leading to significant changes in bond lengths. Moreover, at equilibrium, solid surfaces are highly dynamic in nature presenting a mixture of physisorbed and chemisorbed atoms that can convert their binding state according to the surface conditions. Typical residence times τ_a of an adsorbed atom in trapped state are given by $\tau_a = \tau_{a0} \exp(E_d/k_B T_w)$. According to de Boer [146] the pre-exponential factor τ_{a0} can be written for a monatomic gas as

$$\tau_{a0} = \frac{h}{k_B T_w} f_z \frac{f}{f^*} , \tag{4.37}$$

where f_z is the partition function of the vibration perpendicular to the surface of the adsorbed atoms while f and f^* are the partition functions of the system in the equilibrium and activated states, respectively. Assuming $f \simeq f^*$ (mobile adsorption), the residence time can be written as

$$\tau_a = \frac{h}{k_B T_w} f_z \exp\left(\frac{E_d}{k_B T_w}\right) , \tag{4.38}$$

with $\tau_a = 1/\nu_a = n_a/\dot{n}_a$ where n_a is the number of adsorbate atoms (or ions) per unit surface area of the substrate. Rearranging equation (4.38) it is possible to derive an equation for the degree of coverage of a cathode surface with adsorbed layer in equilibrium, namely

$$\vartheta = \sqrt{\frac{2\pi}{m_g}} \frac{p\hbar}{n_\sigma (k_B T_w)^{3/2}} \exp\left[\frac{E_d(\vartheta)}{k_B T_w}\right] . \tag{4.39}$$

The non-linear relation between the amount of adsorbed atoms (or ions) and the partial pressure of the impinging gas is called *adsorption isotherm*. These curves reflect the nature of the adatom-substrate bound and are of paramount importance to estimate the effect of the deposition on the cathode surface. However, since E_d depends on the degree of coverage of the surface, a theoretical correlation between the desorption energies of atoms and ions and

the degree of coverage must be found. One of the most comprehensive analysis of the desorption energies as a function of the degree of coverage is by Levine and Gyftopoulos [147], who derived a model without involving neither adjustable constants nor detailed quantum mechanical treatment. Much of this section is based on findings of Levine [147–149].The phenomenological approach taken here assumes that metal-adsorbate bonds can be considered partly ionic and partly covalent so that the desorption energy can be represented by

$$E_d = E_{ii} + E_{cc} \, . \tag{4.40}$$

where E_{ii} and E_{cc} are the ionic and the covalent contributions, respectively. Clearly, E_{ii} must vanish for a purely covalent bond, E_{cc} must be null for a purely ionic bond and $E_{cc} \simeq \varphi_a$ when desorption of material from surface of the same bulk material is considered. The dual nature of the surface bond is suggested by the broadening of the valence energy level of the adsorbed particle and by the strength of the bond in case of metallic surfaces immersed in a monatomic metallic vapour. In this conditions, the adsorbed particles are chemisorbed rather that physisorbed by the surface. Moreover, thanks to the surface ionization at high substrate temperatures [150], the metallic particles are mostly adsorbed as ions. It has to be underlined that Rasor and Warner [124] argued that ions and neutrals may exist as distinct states on the surface even though Gadzuk [125] showed that, in case of cesium adsorbed on tungsten, the lifetime of the adatom is in the order of $10^{-15} - 10^{-13}$ s.
The ionic contribution E_{ii} to the desorption energy E_d is assumed to arise from a fraction of charge f_c of the adsorbate which is transferred to the substrate. This fraction f_c determines the partial ionic character of the bond and is associated with the surface dipole moment. By means of a Born-Haber type thermodynamic cycle, the following expression for E_{ii} was derived

$$E_{ii} = f_c \varphi(\vartheta) \left[1 + \frac{f_c}{\varphi(\vartheta)} \left(\frac{q}{16\pi\varepsilon_0 R} - \varepsilon_i \right) \right] \, , \tag{4.41}$$

where ε_i is the ionization potential in units of eV and $R = r_c + r_w$ is the internuclear distance between the substrate and the adsorbate particles, taken equal to the sum of the covalent radii. As expected, if the bond is purely covalent $f_c = 0$, $E_{ii} = 0$, while if $f_c = 1$ the ionic contribution reduces to the energy required to remove an adsorbed ion from the surface, $E_{ii} = \varphi(\vartheta) + q/(16\pi\varepsilon_0 R) - \varepsilon_i$. The fractional charge f_c can be roughly approximated from the dipole moment part of the work function as

$$f_c = \frac{M_e}{qR\cos\beta} \, , \tag{4.42}$$

being M_e the effective dipole moment of equation (4.29) which includes both self-depolarization and dipole-dipole interaction effects. The covalent contribution E_{cc} requires a more intricate analysis to be estimated since it involves the pairing of the valence electrons of the substrate and adsorbate particles to create the chemical bond, namely they have to occupy a common orbital with opposite spins. Since E_{cc} arises from pairing the valence charges, both the substrate and the adsorbates must each contribute to the bond. The contribution of the adsorbate is assumed to be proportional to the cohesive energy φ_a, the valence charge $q_c \propto f_c$ and the strength of the valence orbitals S_c derived according to the molecular orbit (MO) theory. The value of S_c depends on what valence orbital participates in the bond and it is equal to the square root of the number of valence orbitals [151]. The final expression for the adsorbate contribution to the covalent part of the bond is given by $E^c_{cc} = \varphi^c_a S^2_c q_c$. Inclusion of φ_a ensures that E_{cc} is equal to the cohesive energy when the adsorbate is adsorbed on its own bulk material. For similar reasons, the contribution of the substrate is assumed $E^0_{cc} = \varphi^0_a S^2_0 q_0$. The simplest expression of E_{cc} which guarantees the limiting requirements, $E_{cc} = \varphi^c_a$ for $\vartheta = 0$ and $E_{cc} = 0$ in case of purely ionic bond $q_c = 0$, is the following geometric mean

$$E_{cc} = \left[\varphi^c_a \varphi^0_a \frac{4 S^2_c S^2_0}{\left(S^2_c + S^2_0\right)^2} \cdot \frac{4 q_c q_0}{\left(q_c + q_0\right)^2} \right]^{1/2} , \tag{4.43}$$

where $q \simeq \nu - f_c$ with ν is the largest number of valence electrons that participate in the covalent bond, e.g. $\nu = 1$ for alkali metals and $\nu = 2$ for alkaline-earths. Equation (4.44) together with equation (4.41) yield for E_d

$$E_d(\vartheta) = f_c \varphi(\vartheta) \left[1 + \delta(\vartheta)\right] + \sqrt{\varphi^c_a \varphi^0_a} S_{c0} Q_{c0} , \tag{4.44}$$

where $S_{c0} = 2/(S_c/S_0 + S_0/S_c)$ is the angular efficiency of the orbit and $Q_{c0} = \sqrt{1 - f^2_c/\nu^2}$ is the charge efficiency and it is unity when the bond is purely covalent and zero when purely ionic, i.e. when the entire valance charge is transferred from the adsorbate to the substrate $f_c = \nu$. It has to be emphasized that most of the physical constants used in the previous derivation are sensitive to the crystallographic orientation of the substrate so that the obtained results are to be considered as qualitative. However, since the constants merely enter the formalism as input parameters, they can be measured experimentally for a given crystallographic surface arrangement. Figure 4.17 shows the comparison between the theoretical desorption energy for cesium on tungsten with the data taken by Taylor and Langmuir [152]. Comparison with the empirical data indicates a rather good agreement between theory and experiment. Inspection of the data indicates that in the

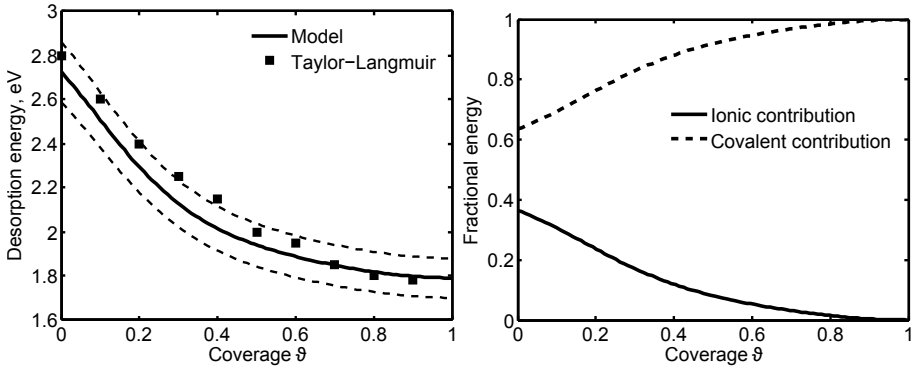

Figure 4.17: Desorption energy for Cs on W and fractional energy. The 5% uncertainty limits are shown as dashed lines.

particular case of Cs/W system, the covalent contribution is dominant and has a weaker dependance on coverage while the ionic contribution accounts for about 40% of the total desorption energy at zero coverage and vanishes at $\vartheta = 1$. Also note that at low coverages the change of desorption energy resembles the linear relation of the work function $\partial_\vartheta \varphi \simeq C\vartheta$ and it is approximately equal to $\partial_\vartheta E_d \simeq f_c \varphi(\vartheta)$.

Thus the theoretical calculation of equation (4.39) is completed and its numerical solution gives the relationship $\vartheta = \vartheta(T_w, p)$. Hence, on the basis of equation (4.39) it is possible to evaluate the effect of the deposition on the work function for any specific adsorbate-substrate pair as a function of the surface temperature T_w and the value of the activator partial pressure $p = nk_BT_w$. Figure 4.18 shows the equilibrium coverage as a function of

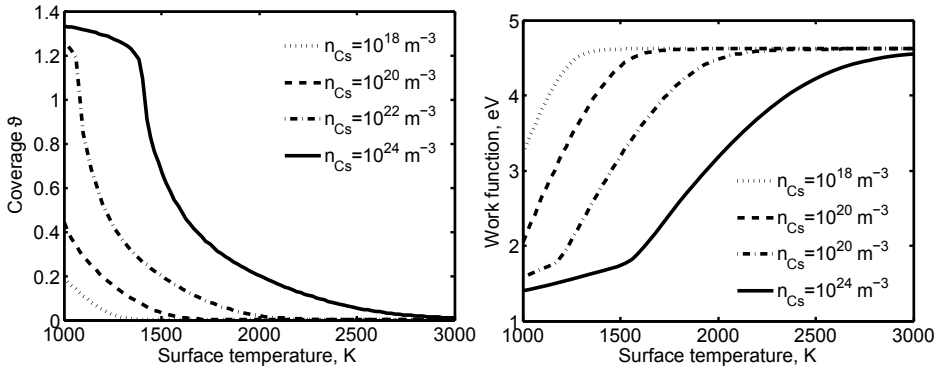

Figure 4.18: Coverage and effective work function as a function of the cathode temperature for different cesium number densities.

the substrate temperature for a Cs/W system. The effect of the cesium deposition on the work function is also reported. From the previous calculations it is clear that, providing a proper replenishment of foreign atoms, the work function can be remarkably reduced leading to a cathode lifetime of several orders of magnitude higher than the relative elementary emitter for a given discharge current.The effectiveness of the propellant seeding with alkali-metal particles on the emission properties of a surface can be shown by considering a simple case of a system in perfect thermodynamic equilibrium as done by Sajben [153]. This implies constant temperatures throughout the plasma and its boundary surfaces, as well as zero net fluxes for neutrals, ions and electrons. Since no transport processes are considered, the net current is also zero. Assuming that the characteristic length scale of the plasma is much larger than the Debye length, the quasi-neutrality can be invoked for the plasma bulk where the degree of ionization at the midplane between the electrodes is given by $\alpha_0 = n_0/(n_0 + n_{a0})$, where n_0 and n_{a0} is the seed plasma and atom density, respectively. For an equilibrium plasma, the Saha equation reads

$$\frac{\alpha_0^2}{1-\alpha_0} = \frac{g_i g_e}{g_a} \frac{(2\pi m_e k_B T)^{3/2}}{h^3} \cdot \frac{\exp\left(-q\varepsilon_i/k_B T\right)}{n_0 + n_{a0}} \,, \tag{4.45}$$

where the subscript "0" refers to the plasma properties at the system centerline. Assuming a Boltzmann distribution across the sheath, then $n_a(r) = n_{a0}$, $n_e(r) = n_0 \exp\left(qV/k_B T\right)$ and $n_i(r) = n_0 \exp\left(-qV/k_B T\right)$ where the plasma potential is taken to be zero at $r = 0$. For a Maxwellian EEDF, the flux of the particle j to the wall is given by $\mu_j = n_j/4\sqrt{8k_B T/\pi m_j}$. The requirement of zero net flux yields to the equilibrium between the flux of particles from and to the wall, $\nu_j = \mu_j$. If the rates at which atoms or ions are desorbed from the surface are given in an Arrhenius form $\nu_{aw} = \omega_a(\vartheta) \exp\left(-qE_a(\vartheta)/k_B T\right)$ and $\nu_{iw} = \omega_i(\vartheta) \exp\left(-eE_i(\vartheta)/k_B T\right)$, the neutral flux balance reads

$$\frac{qE_a(\vartheta)}{k_B T} + \ln\left(\frac{\mu_{a0}}{\omega_a}\right) = 0 \,. \tag{4.46}$$

Equation (4.46) states that for a given temperature and plasma density, the degree of coverage adjusts itself so that the desorbed atom flux balances the arriving flux from the plasma. Similarly, the ion flux balance is given by

$$\nu_{iw} = \mu_{iw} = \mu_{i0} \exp\left(-qV_w/k_B T\right) = \mu_{a0} \frac{\alpha_0}{1-\alpha_0} \exp\left(-qV_w/k_B T\right) \,. \tag{4.47}$$

Equation (4.47) can be recast as

$$\frac{qV_w}{k_B T} = \frac{qE_i}{k_B T} + \ln\left(\frac{\mu_{a0}}{\omega_i}\right) + \ln\left(\frac{\alpha_0}{1-\alpha_0}\right) \,. \tag{4.48}$$

By using a Born-Haber cycle, the ion desorption energy can be expressed as $E_i = E_a + \varepsilon_i - \varphi + \Delta\varphi_S$ where $\Delta\varphi_S \sim \sqrt{E_w}$ is the Schottky correction to the work function. The electric field at the wall can be easily calculated for an equilibrium plasma by using the Poisson equation, namely

$$\varepsilon_0 \frac{d^2V}{dr^2} = qn_0 \left[\exp\left(qV/k_BT\right) - \exp\left(-eV/k_BT\right)\right] \ , \tag{4.49}$$

which can be integrated giving

$$E_w = \sqrt{\frac{8n_0k_BT}{\varepsilon_0}} \sinh\left(\frac{qV_w}{2k_BT}\right) \ . \tag{4.50}$$

It is now possible to calculate the degree of coverage from equation (4.46) and the floating potential from equation (4.48) including the Schottky correction. Figure 4.19 reveals that for any given seed density, the floating potential presents two global extremes. The maxima always correspond to roughly $\vartheta \simeq 0.6$ while the minima to $\vartheta \simeq 0.03$. As the surface temperature

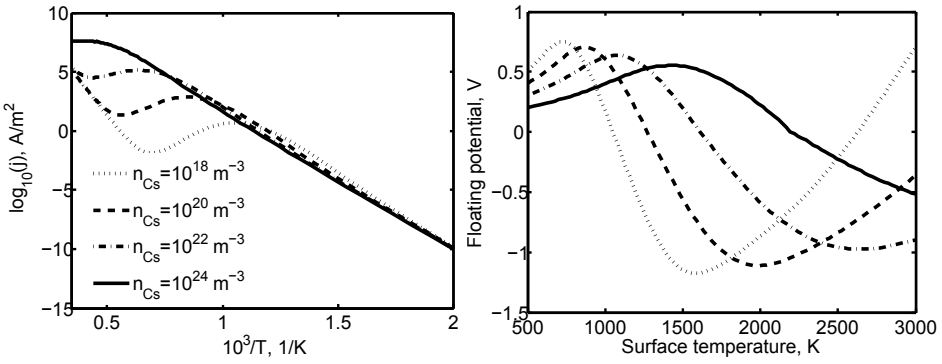

Figure 4.19: Emission electron current and floating potential for a tungsten wall at equilibrium coverage.

is increased, the work function drops and the electron to ion current ratio increases since $\nu_{ew}/\nu_{iw} \propto T^2 \exp\left[-q(\varphi - E_i)/k_BT\right]$. The relative increase in electron emission must be matched by an increased electron arrival rate to the surface, so that V_w has to be electron-attracting. As soon as the quantity $(\varphi - E_i)$ became negative, i.e. for $\vartheta \gtrsim 0.2$, the electron current drops with temperature and the surface has to be electron-repellant. The net effect of the cesium deposition on the emission current density is the presence of a local maximum. Thus, for a given seed number density, there is a local maximum current which occurs at a temperature much lower than the corresponding temperature of the bare substrate.

Chapter 5

Ionization Processes in Hollow Cathodes

As described in Chapter 1, Section 1.3, the *active zone* or *internal plasma column* (hereafter referred to as IPC) is of primary importance in understanding the behaviour of the hollow cathode. However, its limits and area of coverage are still ill-defined both in open-channel and multi-channel hollow cathodes. The internal plasma column is generally associated with the region of the refractory tube in which the thermionic emission is predominant and includes the area of the cathode close to the location of maximum wall temperature. The importance of the IPC can be understood through its relation to the plasma generation processes since the active zone must contain the high-energy electrons needed to efficiently ionize the propellant. However, the ionization potential of the neutral gas sets a minimum energy requirement for a direct-impact single ionization event to occur. The high-energy electrons may come from the emitted electrons (primary) accelerated through the cathode sheath or from the thermalized electrons (secondary) in the high energy tail end of the Maxwellian distribution. The latter is particularly important for non-LTE plasmas in which a Druyvesteyn EEDF gives better approximation than the Maxwellian, as experimentally shown by Domonkos in a low-current hollow cathode [154]. As a consequence, the IPC is like an e-beam sustained plasma, where the ionization of the gas is mostly provided by the injection of high-energy electrons, while the discharge current is carried by the slow electrons.

In this Chapter the theory of the energy degradation of the primary electrons in an argon plasma is discussed while a simple volume-averaged model for multi-step ionization process is described to assess the importance of this phenomenon for typical hollow cathode operations.

5.1 The Ionization Region

The extension of the interelectrode plasma to the interior of the hollow cathode is called IPC. The nature of this region is both a cause and a consequence of the cathode temperature, which depends upon the energy balance between the plasma-related processes and the heat exchange with the environment. Since this hot region determines for a large extent the lifetime and the overall power consumption of a hollow cathode, most of the research conducted so far on these devices gave a particular attention to the description of the phenomena involved in its physical characterization and spatial extension.

In this context, Ferreira and Delcroix [31] have published what is certainly the best attempt to date to construct a comprehensive, self-consistent theory of the ionization processes in a single-channel hollow cathode. In describing the formation of the internal plasma, the model used a gain-function to account for the collisional degradation of the primary electrons. This elegant method basically consists in a direct analysis of the flux of electrons across an iso-velocity sphere in the velocity space. In calculating the total flux across the v =constant sphere, the authors included elastic electron-atom collisions, electron-electron collisions and inelastic ionization and excitation collisions. Using this analysis, the authors discovered that the inelastic collisions rapidly pull the beam electrons down in energy and reintroduce them into the body of the bulk plasma distribution. This process entails a discrete energy spectrum of the primary electrons with a series of narrow peaks corresponding to the knock-on events. Such a result indicates that the energy degradation of the fast electrons cannot be described invoking the continuous slowing-down approximation (CSDA) suggested by Spencer [155], but a discrete-energy-bin method should be adopted as done by Peterson [156] and Cassady [157]. In addition, since the mean energy lost by a primary electron in each elastic collision both with neutrals and with secondary electrons is in the order of 0.1 eV, the cascade may be assumed to be purely inelastic. One of the main results of this model is the function $\alpha(E_0)$, describing the mean number of ions created by each injected electron with an initial energy E_0. The authors calculated that, for Ar propellant, each primary electron yields on average one additional electron due to volume ionization, $\alpha = 1$ for $E_0 < 24$ eV and $1 < \alpha < 2$ for $24 < E_0 < 40$ eV. This means that the volume and the surface processes share equally the total discharge current. However, the total ionization is not tied only with the primary electrons, since a remarkable contribution comes from the ionization collisions between the excited states and the bulk electrons. In other words, the continual production of excited states in the cascade is balanced by the step-wise ionization due to the secondary electrons, thermalized by electron-electron elastic collisions.

In conclusion, the results of the theoretical investigation performed by Ferreira and Delcroix suggest that *the initial energy of the primary electrons controls the production of the metastable states while the temperature of the secondary electrons controls their ionization.*

In spite of its detailed analytical formulation, the model proposed by Ferreira and Delcroix is not a predictive one. The major drawbacks of this model are (i) the need of an experimental wall temperature profile and (ii) the lack of indications about the axial extension of the IPC and (iii) a constant plasma potential at the cathode exit section. Since the results are extremely sensitive to the wall temperature profile, this model is not satisfactory for predictive purposes.

Attempts to measure or theoretically determine the extension of the *active zone* have been sporadically made in the past decades. In their pioneering work on high-current hollow cathodes Lidsky and coworkers [158] suggested that the plasma recedes into the cathode cavity up to the location at which the product between the pressure and the internal diameter is suitable for operation at high current density, namely $pD_C \simeq 1\ m \times Pa$. They speculated that in this condition the ionization mean free path is comparable to the tube size, while no correlation between the IPC axial extension and the cathode temperature profile was identified at that time. However, experimental measurement of the external temperature was performed revealing that a hot spot at about $2500 - 3000$ K appeared on the cathode surface a few diameters from the tip. The authors thus concluded that this macroscopic behaviour can be considered a distinguished feature of proper hollow cathode operations.
A few years later Delcroix [159], through a series of experimental investigations on a tantalum open-channel cathode, proposed that the axial location of the *active zone* is characterized by the condition $p \simeq 500\ Pa$ =constant, being p the gas pressure at the IPC abscissa. This work is, to the author's best knowledge, the first to correlate the location of the cathode wall temperature peak with the axial extension of the ion production region. Performing a large number of temperature measurements for different cathode diameters and mass flow rates, Delcroix concluded that the location of the maximum wall temperature scales as $\ell \sim \dot{m}^{-1}$, suggesting a constant pressure in the *active zone*. In addition, he suggested that such a pressure may correspond to the minimum resistance condition for the current conduction. Interesting enough, no correlation between the axial extension of the IPC and the discharge current was attempted, suggesting a minor role of this parameter in the definition of the plasma penetration length.
Somewhat similar conclusions were drawn by Krishnan [32] after a series of

experimental investigations on a 20 mm inner diameter tungsten hollow cathode operated in pulse mode up to 29 kA. In this work the author concluded that the current attaches over less than one diameter of the cavity near the exit section. Moreover, measuring the plasma potential inside the cathode, he found that the current and voltage patterns in the *active zone* are independent on the dimensions and shape of the cavity. However, his work confirmed the scaling $\ell \sim \dot{m}^{-1}$ and showed that, for a given mass flow rate, increasing the discharge current, the peak of the current density moves downstream, suggesting a further scaling relation, $\ell \sim I^{-1}$. As a result, Krishnan speculated that when the energy exchange mean free path λ^* is either very small or very large compared to the cathode diameter, the resulting surface current distribution is roughly the same and peaks near the exit section. The intermediate case $\lambda^* \simeq D_C$ results in a proper hollow cathode operation with arc attachment upstream in the cavity. Besides, he concluded that, at best, the current can penetrate into hollow cathode of an MPD thruster only for about one cavity diameter, so that $\ell \leq D_C$. As Krishnan admitted, however, it is not clear if the results obtained with pulsed cathodes can be applicable also for steady-state devices since the thermal history of the surface and, thus, the electron emission mechanisms, is dramatically different.
At the beginning of the 1980s, Siegfried [160] deeply investigated both theoretically and experimentally a series of orificed hollow cathodes for ion thruster applications. An important result of this study was the estimation of the axial extension of the ionization region. Starting from the work of Ferreira and Delcroix, the author suggested that the ion production region can probably extend into the cathode cavity for few primary electron energy exchange mean free paths. Since beam electrons can lose energy both by elastic collisions over a mean free path λ_{el} and by inelastic collisions over a mean free path λ_{in}, Siegfried concluded that $\ell \sim \lambda_p^* = (1/\lambda_{in} + 1/\lambda_{el})^{-1}$. This model entails a sharp drop off of the plasma density in the upstream region of the *active zone*. Indeed, experimental data presented by Goebel [6], indicate that since $T_e < \varepsilon_i$, the plasma is dominated by recombination phenomena and its number density scales as $n(z) \sim \exp(-z)$ along the cathode axis, lending credence to the result of Siegfried. In addition, the author found the mean free path for inelastic collision to be insensitive to the various excited states number density and suggested scaling relation in the form $\ell \sim (n_n E_0)^{-1}$, based only on the typical plasma conditions and neutral density [161]. It is worth noting that for typical hollow cathodes operating at about $300 - 500$ Pa, a plasma penetration length of a few λ^* corresponds to a pressure-diameter product of $\sim 1\ m \times Pa$, as reported by Lidsky, corroborating the finding that, at this value of the pD_C product, the primary electron

mean free path is in the order of the cathode radius. Besides, unlike Ferreira, Siegfried calculated that approximately 70% of the total discharge current is provided by the surface electron emission, while the remaining 30% comes from volume ionization processes.

It is important to address here the lack of experimental investigations carried out to directly measure the plasma properties inside a hollow cathode for MPD thruster applications. The harsh environment within the active zone makes these measurements very challenging and therefore it is understandable that they had been rarely accomplished. However, in the following sections of this dissertation, the basic phenomena taking place in the IPC of a hollow cathode are examined in an attempt to find proper scaling relations and phenomenological correlations to indirectly determine the plasma parameters through an analysis of its integral operative parameters and temperature profiles.

5.2 Physical Processes in the Ionization Region

The excitation and the ionization of the neutral gas inside the hollow cathode are mostly produced by the primary electrons emitted by the cathode surface. After being accelerated by the cathode fall, some of them immediately produce excitation and ionization, thus loosing a considerable part of the energy and becoming thermalized in subsequent collisions both with heavy particles and bulk electrons. However, the number of accelerated electrons that do not experience collisions reaches the opposite wall where they are decelerated and returned back. These electrons may accomplish several bounces before experiencing a non-elastic collision. Clearly, the number of these electrons is larger at lower gas pressure. The study of the complex energy degradation process of the primary electrons to the thermalized state constitutes the central problem of the whole hollow cathode theory and is usually referred to as "electron cascade". The thermalization process of both mono-energetic and Maxwellian distributed fast electrons colliding with plasma electrons and heavy particles along with the problem of the neutral gas heating are here discussed and analyzed in detail.

5.2.1 Electron Relaxation and Thermalization Times

The problem of the electron cascade can be outlined considering a primary electron injected in the plasma bulk with a velocity $w = \sqrt{2E_0/m_e}$ and colliding with a population of Maxwellian electrons thermalized at a temperature T_e. In this conditions Spitzer [162] defined the slowing-down time τ_s as the rate of change of the mean velocity of the primary mono-energetic electron

by encounters, namely

$$\tau_s = -\frac{w}{\langle \Delta w \rangle} = \frac{w}{2A_D l_s^2 G(l_s w)} \,, \tag{5.1}$$

where A_D is a diffusion constant, $l_s \equiv \sqrt{m_e/2k_B T_e}$ is the inverse mean velocity of the secondary electrons and $G(l_s w)$ is a function defined in terms of the error function $\Phi(x)$ as

$$G(x) = \frac{\Phi(x) - x\partial_x \Phi(x)}{2x^2} \,. \tag{5.2}$$

Equation (5.1) has two important limiting cases. If w exceeds the mean square root velocity of the bulk electrons u_{th}, then $l_s^2 G(l_s w) \simeq 1/2w^2$ and $\tau_s \propto w^3$. On the other hand, if $w \ll u_{th}$, τ_s approaches a constant value given by $\tau_s \propto (A_D l_s^3)^{-1}$. Assuming that $w \gg u_{th}$, equation (5.1) can be thus recast as $\tau_s \simeq w^3/A_D$. However, primary electrons experience Coulomb interactions with both ions and electrons transferring their energy to them. Using the quasi neutral condition $n_e = n_i \simeq n$, it is possible to derive

$$\tau_s^{-1} = \tau_{s,e-e}^{-1} + \tau_{s,e-i}^{-1} = \frac{q^4 n_e \ln\Lambda}{2\pi\varepsilon_0^2 m_e^2 w^3} + \frac{q^4 n_i \ln\Lambda}{4\pi\varepsilon_0^2 m_e^2 w^3} = \frac{3q^4 n \ln\Lambda}{4\pi\varepsilon_0^2 m_e^2 w^3} \,, \tag{5.3}$$

where $\varepsilon_0 \simeq 8.854 \times 10^{-12}\ As/Vm$ is the permittivity of free space and $\ln\Lambda = \ln\left(6\pi n \lambda_D^3\right) \simeq 10$ is the Coulomb logarithm. Figure 5.1-left shows

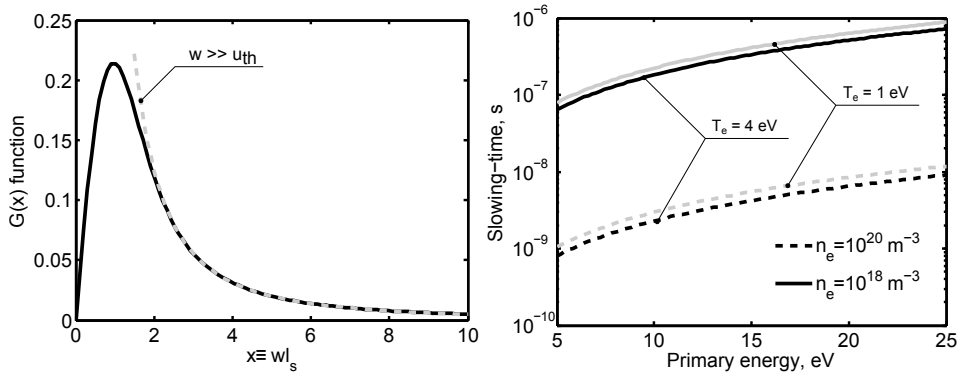

Figure 5.1: G(x) equation and slowing-down time as a function of the primary energy.

the slowing-down time as a function of the primary electron energy for different plasma bulk densities and electron temperatures. The primary electrons, after they have gained several eV by acceleration in the sheath, do not slow down much as long as the plasma is of low density (e.g. $n < 10^{16}\ m^{-3}$).

As the plasma density increases, the slowing-down time remarkably reduces, leading to a rapid thermalization of the primary electrons. It is worth noting that assuming a total cross section for electron-argon interaction of about $\sigma_{e-Ar} \simeq 10^{-20}\ m^2$ [163] and an argon pressure in the cathode cavity of $p \simeq 10^2\ Pa$, the neutral number density is about $n_{Ar} = p/k_B T \simeq 10^{21}\ m^{-3}$ so that the resulting mean free path for electron-neutral collision is $\lambda_{e-Ar} \simeq 10^{-2}\ m$. Since the beam electrons travel with $w \simeq 10^6\ m/s$, the collisional characteristic time is given by $\tau_{coll} = \lambda_{e-Ar}/w \simeq 10^{-10} - 10^{-9}\ s$, which is shorter than the slowing-down time for mono-energetic electrons.

When the primary and the secondary electrons have different temperatures and the emitted electrons have a Maxwellian distribution, it is possible to represent the change in temperature of the fast electrons as an ordinary relaxation equation in the form

$$\frac{dT_p}{dt} = \frac{T_s - T_p}{\tau_{th}}\ , \tag{5.4}$$

where τ_{th} is the equipartition time which characterizes the rate of approach to equilibrium. Clearly, the solution of equation (5.4) is

$$T_p = T_{p0} \exp\left(-t/\tau_{th}\right) + T_s \left[1 - \exp\left(-t/\tau_{th}\right)\right]\ , \tag{5.5}$$

in which τ_{th} can be interpreted as the relaxation time for the temperature equipartition process. Spitzer [162] obtained an expression for the electron-electron equipartition time scale as

$$\tau_{th} = \frac{12\pi^{3/2}\varepsilon_0^2 m_e^{1/2} \left(k_B T_s + k_B T_p\right)^{3/2}}{q^4 n_e \ln\Lambda}\ , \tag{5.6}$$

Figure 5.2-left shows the relaxation time for mono-energetic primary electrons τ_s and Maxwellian distributed beam electrons τ_{th} injected in a 5 eV bulk plasma. The slowing-down time was found to be faster than the equipartition time, as can be shown considering

$$\frac{\tau_{th}}{\tau_s} = \frac{\pi^{1/2}}{m_e^{3/2}} \frac{(k_B T)^{3/2}}{w^3} \simeq 10^0 - 10^1\ , \tag{5.7}$$

where $T = T_p + T_s$. It is interesting to note that the ratio τ_{th}/τ_s is independent of the bulk plasma density, as it appears in Fig. 5.2-right. Considering a hollow cathode 10 mm in diameter, from a preliminary investigation of the characteristic time scales for beam electron thermalization, it is possible to state that for low-pressure operations, the plasma in the hollow cathode is somewhat transparent for the beam electrons and the discharge is maintained

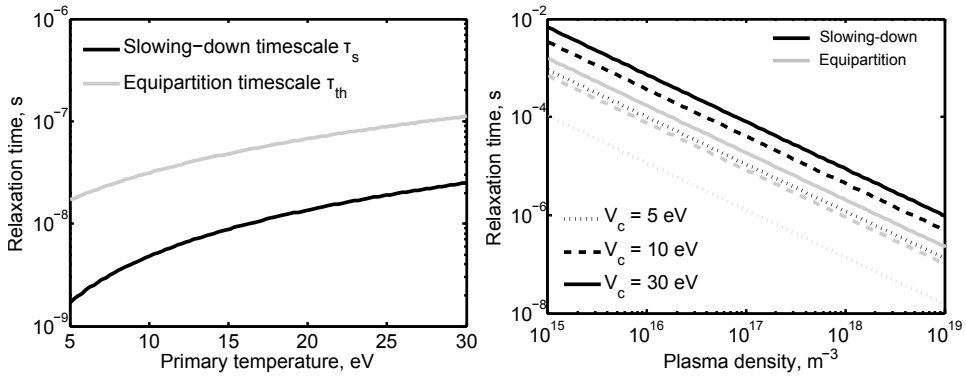

Figure 5.2: (Left) Relaxation times of mono-energetic primaries τ_s and a Maxwellian primary population τ_{th} in a 5 eV, $10^{20}\ m^{-3}$ plasma. (Right) Characteristic time scales as a function of the plasma density with an electron temperature of 5 eV.

purely by these electrons. For pressures above 10^3 Pa, the electron beam does not penetrate much into the plasma bulk since it looses most of its energy at the edge of the plasma volume ($\lambda = w\tau_s \simeq 10^6 \cdot 10^{-9} = 10^{-3}\ m$). In this case, the plasma bulk is maintained by the secondary electrons with an energy that increases with the plasma pressure. For typical operative pressures of about 10^2 Pa both these processes take place in the cathode cavity to sustain the discharge.

5.2.2 Gas Heating Mechanisms

In the IPC of a hollow cathode, a strong thermal non-equilibrium between electrons and neutrals exists. As a matter of fact, the gas temperature is usually assumed to be of the same order of magnitude of the cathode wall temperature, i.e. $T_n \simeq 0.1\ eV$, even though no justifications are clearly given [164–166]. As a consequence, the heat transfer process between neutral gas particles and the plasma constituents in the *active zone* of a hollow cathode is here investigated.

As shown by Delcroix [159], the neutral gas can be heated mainly by (i) elastic electron-neutral collisions, (ii) inelastic collisions between excited atoms and (iii) heat convection from the wall. In order to estimate the neutral number density in the cathode cavity, it has to be considered that, in steady-state operations, the ion production in the volume must be equal to the ion loss rate toward the cathode wall, thus neglecting the ion flux at the upstream end of the control volume. In this condition,

$$\pi r_C^2 \ell n_n n_e \langle \sigma_{en} u_e \rangle = 2\pi r \ell n_e u_D\ , \tag{5.8}$$

where r_C is the cathode internal radius, ℓ is the IPC axial length and u_D is the radial ion diffusion velocity. Assuming that the radial density gradient is negligible, from the ion momentum equation $u_D \simeq qE/m_i\nu$ with $\nu = n_n\langle\sigma_{in}u_{th}\rangle$ neutral-ion collision frequency. As a result, from equation (5.8), the neutral number density can be roughly estimated as

$$n_n \simeq \frac{2}{r_C}\frac{u_D}{\langle\sigma_{en}u_e\rangle} = \frac{1}{r_C}\sqrt{\frac{qV_c\pi\sqrt{m_em_i}}{4k_B\sigma_{en}\sigma_{in}m_i\sqrt{T_eT_i}}}\,. \tag{5.9}$$

Considering a cathode potential drop of about $V_c \simeq 10$ V, an electron temperature of $T_e \simeq 2$ eV and a non-equilibrium ratio of $T_e/T_i \simeq 10$ [167], the neutral number density in a 10 mm diameter hollow cathode is in the order of $n_n \simeq 10^{21}\ m^{-3}$.

The mean free path for electron-argon elastic collision is then given by $\lambda_{el} = (n_n\sigma_{en})^{-1} \simeq 7\cdot10^{-2}$ m with $\sigma_{en} \simeq 10^{-20}\ m^2$ [168]. As shown in the previous Chapter, the gradual energy transfer from the primary electrons to the neutral atoms takes place over a characteristic time much longer than the relaxation time, since the energy transfer from a single collisional event, according to the conservation of momentum law, cannot exceed a fraction of the order of $2m_e/m_n$ of their kinetic energy. Therefore, appreciable energy transfer can occur only when the particles are subjected to a remarkable number of collisions, approximately $N \simeq m_n/(2m_e) \simeq 4\cdot10^4$. Applying the Random Walk (RW) theory, after N collisions, the electron reaches an averaged distance over many trajectories in the radial direction of $\lambda_{th} = \sqrt{N}\lambda_{el} \simeq 14$ m. Since $\lambda_{th} \gg r_C$, it is possible to infer that the energy transferred by the primary electrons to the neutral atoms is negligible. As a matter of fact, in order to loose all their initial energy E_0, the beam electrons need to cover a distance equal to λ_{th}, so that along a cathode radius the average energy lost is given by $E_r = r_C/\lambda_{th}E_0 \simeq 3.5\cdot10^{-4}E_0$.

Since typical cathode falls impart an energy to the emitted electrons which is not sufficient to allow for direct-impact ionization of Ar atoms, atom excitation is the only possible direct process with a single electron-neutral inelastic collision. These excited states can give origin to different other reactions, e.g. ionization, spontaneous de-excitation with emission of a photon and collisional de-excitation with kinetic energy transfer (Coulomb de-excitation). Considering only the Ar $4p$ emission lines[1], the photon wavelength due to spontaneous de-excitation is given by $\lambda = hc/\varepsilon_m \simeq 100\ nm$, in the ultraviolet spectrum. Since the adsorption cross section at the center of a line is in the order of $\sigma_p \sim \lambda^2 \simeq 1.3\cdot10^{-14}\ m^2$ [169], the mean free path for photon adsorption is given by $\lambda_p = (n_e\sigma_p)^{-1} \simeq 100$ nm and the plasma is

[1]Further details concerning the argon excited states are given in Section 5.3

optically thick at the 100 nm bound-bound transitions. A rough estimation of the heating contribution due to these interatomic transitions can be performed considering that the energy per unit time corresponding to the transition from a state of higher energy i to a state of lower energy j is given by $Q_p = n_i h\nu A_{ij}$, where A_{ij} is the Einstein emission probability and n_i is the number density of the excited state i. The population of the excited state is determined applying the principle of *detailed balance* for the various processes involved, namely $n_i/n_n = n_e u\sigma_{ni}/\sum_j A_{ij}$. Here n_n is the population of the ground-level and $\sigma_{ni} \simeq 1.32 \cdot 10^{-22}\ m^2$ is the average cross section for the electron collision excitation at the 100 nm line [168]. The radiation power is therefore given by $P = n_o I\sigma_{ni} h\nu A_{ij}\ell/q\sum_j A_{ij} \simeq 0.8\ W$ for an IPC length of $\ell \simeq D_C$ and a discharge current of $I \simeq 100\ A$. Since the total power consumption of a cathode is approximately $P_T \simeq V_C I \simeq 10^3\ W$, the contribution of the bond-bond transitions to the gas heating is negligible. As a consequence only the Coulomb de-excitation is supposed to effectively heat the neutral gas.

The effective excitation cross section for an Ar neutral atom colliding with a 10 eV electron is in the order of $\sigma_{ex} \simeq 7 \cdot 10^{-22}\ m^2$, so that the mean free path for electron-neutral excitation is given by $\lambda_{ex} = (n_n\sigma_{ex})^{-1} \simeq 1.4\ m$. To estimate the probability of inelastic collisions between electrons and ground-level neutrals, the maximum length cover by electrons before experiencing an elastic collision should be found. Considering a simple diffusion-like process describing the motion of the electron up to the cathode wall $D = r_C^2/\tau \simeq u_e r_C^2/\lambda_{el}$, the total path of the electron between elastic collisions is given by $L_{el} = D/u_e = r_C^2/\lambda_{el} \simeq 3.4 \cdot 10^{-4}\ m$. Along this path, the free electrons have a probability of inelastic collision with ground-level neutrals described by $p = L_{el}/\lambda_{ex} \simeq 0.02\%$. As a consequence, the electrons can loose only a negligible fraction of their initial energy to excite the neutral gas.

Similarly, considering the metastable states $^3P_0$ and $^3P_2$ of the Ar propellant, the mean free path for momentum transfer between these levels is given by $\lambda_m = (n_n\sigma_m)^{-1} \simeq 3 \cdot 10^{-3}\ m$ with $\sigma_m \simeq 3.4 \cdot 10^{-19}\ m^{-2}$ from Phelps [168]. The maximum length covered by these metastable atoms before arriving to the wall is thus $L_m = r_C^2/\lambda_m \simeq 8.5 \cdot 10^{-3}\ m$. The mean free path for atom collision de-excitation is approximately $\lambda_d = (n_n\sigma_d)^{-1} \simeq 480\ m$ being $\sigma_d \simeq 2 \cdot 10^{-24}\ m^{-2}$. As a result, the de-excitation can account for only $E_d \simeq 10^{-5} E_0$. It is thus possible to conclude that the heat transfer from the wall is the main gas heating process.

By applying a simple energy balance for an inviscid, fully developed laminar flow moving at a constant mass flow rate $\dot{m}$ in a thin-wall tube with a

constant surface temperature T_w, the variation of the mean gas temperature along the tube axis T_m can be written as

$$\frac{dT_m}{dx} = S_t \left(T_w - T_m\right) \ , \tag{5.10}$$

where S_t is the local Stanton number. Equation (5.10) indicates that the temperature difference $(T_w - T_m)$ decays exponentially with distance along the tube axis and reaches the 90% of T_w in few tens of millimeters for $S_t > 50$. A substantial difference between the gas and the surface temperatures can be

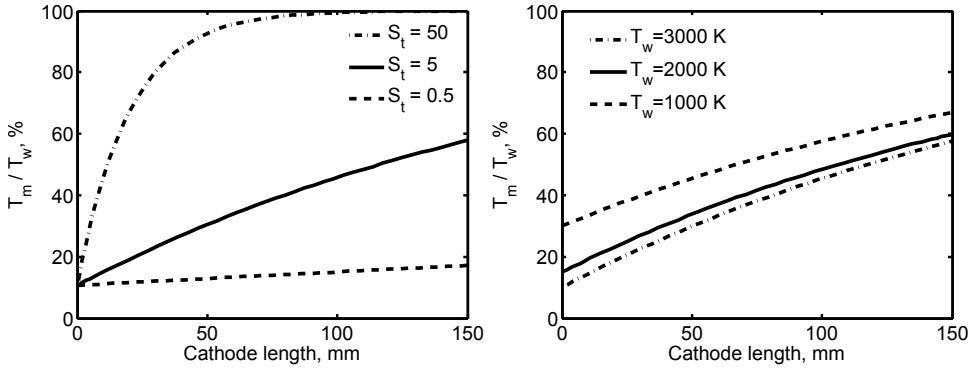

Figure 5.3: Axial variation of the neutral mean temperature for different Stanton numbers at $T_w = 2800$ K (left) and wall temperature at $S_t = 5$ (right).

observed only at high mass flow rates, i.d. low Stanton numbers, in particular $S_t \simeq 5$ at $\dot{m} \simeq 10$ mg/s for the cathode geometry here considered.
In addition, the radial distribution of the heavy particle temperature can be estimated following Salhi [170]. The model considers the heat transfer between the electrons, the ions and neutrals in the *active zone*. Starting from equation (5.4), the electron-ion heat transfer can be written as

$$\frac{1}{r}\frac{d}{dr}\left(r\kappa\frac{dT_i}{dr}\right) = \rho c_p \frac{dT_i}{dt} \simeq \rho c_p \frac{T_i - T_e}{\tau_{th}} \ , \tag{5.11}$$

where τ_{th} is the electron-ion equipartition timescale. A similar equation can be written also for the energy transport from the electrons to the neutrals, namely

$$\rho c_p \left.\frac{dT_n}{dt}\right|_{n-e} = \frac{2m_e}{m_n}\frac{3}{2}\kappa \left(T_n - T_e\right)\nu_{en} n_n \ , \tag{5.12}$$

where $\nu_{e,n}$ is the mean momentum transfer collision frequency calculated by fitting the data gathered by Nakamura [171], namely

$$\nu_{en} = 10^{-20} n_n \sqrt{\frac{8qT_e}{\pi m_e}} \left(2 \cdot 10^{-4} T_e^5 - 6.1 \cdot 10^{-3} T_e^3 - 0.132 T_e^2 + 1.295 T_e + 0.304\right) , \tag{5.13}$$

where T_e is in units of eV. Equation (5.12) can be further modified to include the heat transfer from the ions to the neutrals

$$\rho c_p \frac{dT_n}{dt}\bigg|_{n-i} = 3\kappa \left(T_n - T_i\right) \nu_{in} n_n \, . \tag{5.14}$$

with

$$\nu_{in} = n_n \sigma_{CEX} \sqrt{\frac{2qT_n}{\pi m_n}} \left[\exp(-\zeta^2) + \left(2\zeta + \zeta^{-1}\right) \sqrt{(\pi)}/2Erf(\zeta)\right] , \tag{5.15}$$

where $\zeta = \sqrt{m_m/2qT_n}\bar{u}_i$ is the normalized ion velocity and $\sigma_{CEX} \simeq 10^{-18}\ m^2$ is charge exchange cross section. The previous equation can be combined together to get an expression for the ion and neutral temperature variation along the cathode radius as

$$\begin{aligned} \frac{1}{r}\frac{d}{dr}\left(r\kappa \frac{dT_i}{dr}\right) &= \rho c_p \left[\frac{T_i - T_e}{\tau_{th}} + 2\left(T_i - T_n\right)\nu_{in}\right] \\ \frac{1}{r}\frac{d}{dr}\left(r\kappa \frac{dT_n}{dr}\right) &= \rho c_p \left[\frac{2m_e}{m_n}\left(T_n - T_e\right)\nu_{en} + 2\left(T_n - T_i\right)\nu_{in}\right] \, . \end{aligned} \tag{5.16}$$

The thermal conductivity can be calculated as $\kappa = 2k_B/\sigma_h \sqrt{k_B T_{i,n}/\pi m_{i,n}}$, where $\sigma_h = 2/3\pi d_m^2 \simeq 9.3 \cdot 10^{-20}\ m^2$ is the average heavy particle cross section. Finally, using the kinetic description, the product between the density and the specific heat capacity can be written as $\rho c_p = 3/2 n_{e,n} k_B$.
The boundary conditions for equations (5.16) are that the temperature at the cathode surface is equal to the wall temperature and that at the cathode centerline the radial temperature gradient is zero, namely

$$\begin{aligned} T\left(r = r_C\right) &= T_w \\ \frac{dT_{i,n}}{dr}\bigg|_{r=0} &= 0 \, . \end{aligned} \tag{5.17}$$

The result of the numerical solution of equations (5.16) is shown in Fig. 5.4 for different plasma number densities and bulk electron temperatures. Even though the temperature of the heavy particles can appreciably deviate both from the wall temperature and between each other, the plasma densities required to yield to this result are higher than the typical values experimentally

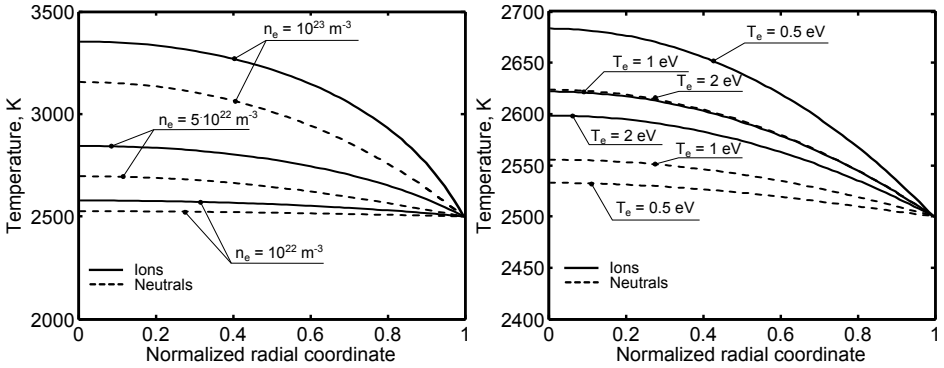

Figure 5.4: Radial variation of the heavy particle temperatures for different plasma densities ($T_e = 1; eV$, $n_n = 10^{21}\ m^{-3}$) and electron temperatures ($n_e = 10^{22}\ m^{-3}$, $n_n = 10^{21}\ m^{-3}$).

observed in open-channel hollow cathodes [172]. As a result, it is possible to state that *a large fraction of the primary electrons energy is indirectly transferred to the heavy particles through the cathode surface temperature via local influence of the plasma density and sheath potential.*

The ordering of the characteristic length for $n_n = 10^{21}\ m^{-3}$ and $n_n = 10^{22}\ m^{-3}$ is shown as an example in Fig. 5.5. The plasma is dominated by excitation electron-neutral collisions and this picture is not dramatically different when the neutral density is decreased. The large electron-heavy particle thermalization mean free path confirms that the two species' temperatures may, indeed, differ substantially.

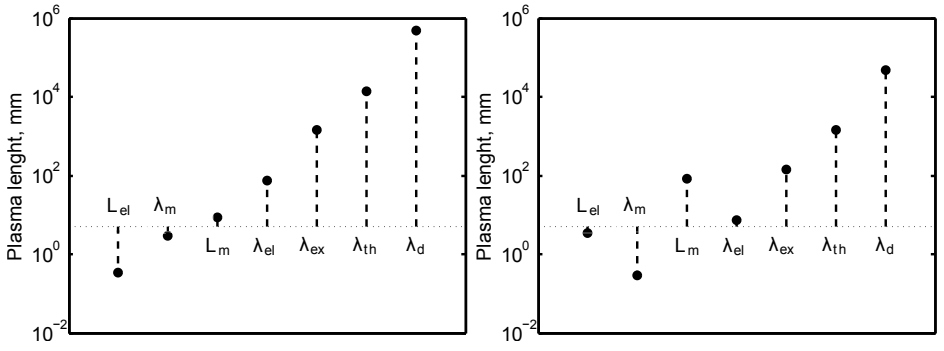

Figure 5.5: Characteristic plasma length scales in the cathode cavity for $n_n = 10^{21}\ m^{-3}$ (left) and $n_n = 10^{22}\ m^{-3}$ (right). The cathode inner radius is used as baseline.

5.3 Multi-step Ionization Model

In order to assess the role of the step-wise ionization in the cathode cavity, a simple collisional-radiative (CR), volume-averaged model for the non-equilibrium ionization in a steady-state hollow cathode is here presented and discussed. It has to be underlined that the present model considers the secondary electrons only and the effects of the beam electrons are not included so far. The steady-state regimes of non-equilibrium discharges are provided by a balance of generation and loss of charge particles. The generation of electrons and ions is mainly tied with volume ionization processes, while the losses of charged particles can be related to both volume processes of recombination and diffusion to the walls with subsequent surface recombination (catalytic surface). These two loss mechanisms identify two different regimes of steady-state discharges: volume-processes control discharges and diffusion-dominated discharges. As suggested by Lieberman [173], when the degree of ionization is relatively high for the diffusion to be considered as ambipolar, the frequency loss for particle diffusion toward the walls can be written as $\nu_D = D_a/\Lambda_D^2$, where D_a is the coefficient of ambipolar diffusion and Λ_D is the characteristic diffusion length scale. Solutions to the diffusion equation in a cylindrical domain of radius r_C and length ℓ indicate that

$$\frac{1}{\Lambda_D^2} = \left(\frac{\chi_{01}}{r_C}\right)^2 + \left(\frac{\pi}{\ell}\right)^2 , \tag{5.18}$$

where χ_{01} is the first zero of the zero-order Bessel function. Clearly, the discharge processes in the cathode cavity are volume-controlled if

$$n_n K_i(T_e) \gg \frac{D_a}{\Lambda_D^2} , \tag{5.19}$$

where $K_i(T_e)$ is the ionization rate coefficient. Since $D_a \propto 1/n_n$ and $n_n \propto p$, the criterion of equation (5.19) can be expressed in terms of pressure as $p \gg (K_i(T_e)\Lambda_D^2)^{-1/2}$. As a consequence, it is possible to qualitatively state that when the pressure exceeds $(1-2)\cdot 10^3$ Pa, the diffusion is relatively slow and volume processes dominate the particle balance in the cavity. Since typical pressures in an open-channel cathode are in the order of few hundreds Pa, the discharge processes are assumed to be diffusion-controlled. Under this hypothesis the particle balance equations of the excited states can be written as a combination of the rate coefficients related to the excitation, ionization and radiative de-excitation processes involved.

Figure 5.6 shows the energy levels of an argon atom (Grotrian diagram). In order to make reasonable CR analysis possible and considering that close-lying levels are likely to be very closely coupled via collisions, the various

energy levels of the Ar atom were lumped together. Thus, the lumped energy and transmission probabilities were averaged as

$$\langle A_{ij} \rangle = \frac{\sum_i g_i A_{ij}}{\sum_i g_i} \ , \tag{5.20}$$

where g_i is the degeneracy of the $i-$th sublevel and A_{ij} is the transmission probability between the states i and j. The energy levels used for the atomic Ar I model are the same levels adopted by Gomes [174]. The model includes a collective representation of the four $4s$ and $4p$ levels and the relative bond-bond, bond-free transmission processes. The $4s$ and $4p$ levels are among the

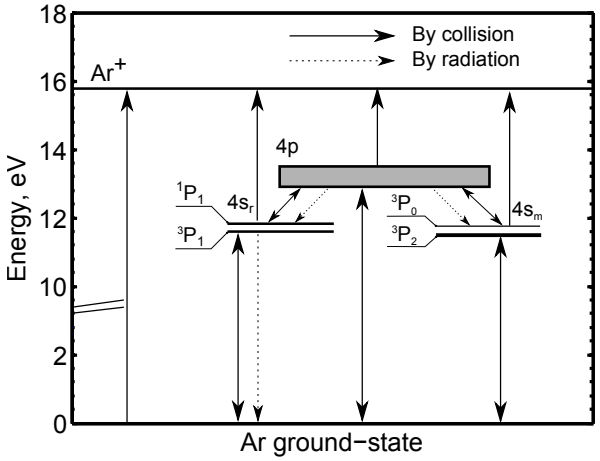

Figure 5.6: A schematic diagram for energy level of an argon atom.

most extensively studied rare gas levels due to their intrinsic physical properties and because they generate spectral lines frequently present in various applications in the visible ($4s - 4p$) and in the UV regions ($3p - 4s$) [175]. Of the four $4s$ levels, two are resonant ($4s_r$) and two metastable ($4s_m$). The metastable states are characterized by a forbidden transition (small probability of spontaneous occurrence) to the ground-level (GL). The presence of low-energy metastable states ($\varepsilon_m \simeq 11\ eV$) contributes to an increased population of these levels in comparison with the most excited states ($4s_r$ and $4p$), to the point that their population may became a significant fraction of the entire neutral density, including the ground-level population [176]. Moreover, since the ionization cross sections of the excited states are considerably higher than the direct Ar-GL/Ar-I cross section, the metastable $4s$ levels, even when less populated then the GL, may significantly contribute to the plasma bulk ionization. The reaction rates of the transmission processes included in the model have been collected by Min-Hyong [177] and Ashida [178]

and are listed in Table 5.1.

The kinetics of each excited state can be described by the following set of

Reaction	Rate constant
$Ar^+ + e \rightarrow Ar_m + e$	$K_{gm} = 2.5 \times 10^{-15} T_e^{0.74} \exp(-11.56/T_e)$
$Ar + e \rightarrow Ar_r + e$	$K_{gr} = 2.5 \times 10^{-15} T_e^{0.74} \exp(-11.56/T_e)$
$Ar + e \rightarrow Ar_p + e$	$K_{gp} = 1.4 \times 10^{-14} T_e^{0.71} \exp(-13.20/T_e)$
$Ar + e \rightarrow Ar^+ + 2e$	$K_{gi} = 2.3 \times 10^{-14} T_e^{0.68} \exp(-15.76/T_e)$
$Ar_m + e \rightarrow Ar + e$	$K_{mg} = 4.3 \times 10^{-16} T_e^{0.74}$
$Ar_m + e \rightarrow Ar_r + e$	$K_{mr} = 2.0 \times 10^{-13}$
$Ar_m + e \rightarrow Ar_p + e$	$K_{mp} = 8.9 \times 10^{-13} T_e^{0.51} \exp(-1.59/T_e)$
$Ar_m + e \rightarrow Ar^+ + 2e$	$K_{mi} = 6.8 \times 10^{-15} T_e^{0.67} \exp(-4.20/T_e)$
$Ar_r + e \rightarrow Ar + e$	$K_{rg} = 4.3 \times 10^{-16} T_e^{0.74}$
$Ar_r + e \rightarrow Ar_m + e$	$K_{rm} = 3.0 \times 10^{-13}$
$Ar_r + e \rightarrow Ar_p + e$	$K_{rp} = 8.9 \times 10^{-13} T_e^{0.51} \exp(-1.59/T_e)$
$Ar_r + e \rightarrow Ar^+ + 2e$	$K_{ri} = 6.8 \times 10^{-15} T_e^{0.67} \exp(-4.20/T_e)$
$Ar_p + e \rightarrow Ar + e$	$K_{pi} = 3.9 \times 10^{-16} T_e^{0.71}$
$Ar_p + e \rightarrow Ar_m + e$	$K_{pm} = 1.5 \times 10^{-13} T_e^{0.51}$
$Ar_p + e \rightarrow Ar_r + e$	$K_{pr} = 1.5 \times 10^{-13} T_e^{0.51}$
$Ar_p + e \rightarrow Ar^+ + 2e$	$K_{pi} = 1.8 \times 10^{-13} T_e^{0.61} \exp(-2.61/T_e)$
$Ar_r \rightarrow Ar + h\nu$	$A_r = 5 \times 10^6$
$Ar_p \rightarrow Ar_m + h\nu$	$A_{pm} = 3 \times 10^4$
$Ar_p \rightarrow Ar_r + h\nu$	$A_{pr} = 3 \times 10^4$

Table 5.1: Reaction and rate constants used in the model. Units of K are $m^3\,s^{-1}$ and A are s^{-1}.

equations

$$\frac{dn_m}{dt} = K_{gm} n_g n_e + K_{rm} n_r n_e + (K_{pm} + A_{pm}) n_p - \left[(K_{mr} + K_{mp} + K_{mg} + K_{mi})\, n_e + \frac{D_a}{\Lambda_D^2} \right] n_m = 0 \,, \quad (5.21)$$

$$\frac{dn_r}{dt} = K_{gr} n_g n_e + K_{mr} n_m n_e + (K_{pr} + A_{pr}) n_p - \left[(K_{rp} + K_{rm} + K_{rg} + K_{ri})\, n_e + A_r + \frac{D_a}{\Lambda_D^2} \right] n_r = 0 \,, \quad (5.22)$$

$$\frac{dn_p}{dt} = K_{gp} n_g n_e + K_{mp} n_m n_e + K_{rp} n_r n_e - \left[(K_{pm} + K_{pr} + K_{pg} + K_{pi})\, n_e + A_{pm} + A_{pr} + \frac{D_a}{\Lambda_D^2} \right] n_m = 0 \,. \quad (5.23)$$

The above equations can be numerically solved with respect to the number densities of the excited states, being n_m, n_r and n_p the atom densities of the $4s$ metastable state, $4s$ resonant state and $4p$ state, respectively. For an uniform density discharge, the ion power loss to the walls per unit time and unit area is given by the Bohm sheath criterion as $\Gamma_i = n_s u_B = n_s \sqrt{k_B T_e / m_i}$, where n_s is the plasma density at the sheath edge. Following Lieberman [173], when the transport is diffusive and ambipolar, the ion drift velocity greatly exceeds the ion thermal velocity within the plasma bulk, so that the radial plasma density profile in a cylindrical cavity should be relatively flat in the center and steep near the sheath edge. In this condition, the ratio between the plasma density at the sheath edge to the plasma density at the system centerline can be written as

$$h_r = \frac{n_s}{n_0} \simeq 0.86 \left(4 + \frac{r_C}{\lambda_i} \right)^{-1/2} \,, \quad (5.24)$$

where λ_i is the ion-neutral mean free path. Therefore, the balance equation between ion loss and total volume ionization, including multi-step processes, reads

$$\frac{\sum_k K_{ki} n_k(T_e)}{u_B(T_e)} = \frac{2}{r_C} \,. \quad (5.25)$$

Equation (5.25) can be thus solved for the electron temperature in the cathode cavity. As a result, the contribution of the multi-step ionization to the total ionization rate can be estimated as

$$\chi_i = \frac{K_{mi} n_m + K_{ri} n_r + K_{pi} n_p}{K_{gi} n_g + K_{mi} n_m + K_{ri} n_r + K_{pi} n_p} \,. \quad (5.26)$$

Figure 5.7-right indicates that an increase in pressure reduces the electron temperature, which results in the decrease of the ionization rate constants. However, since the energy required to ionize an excited atom is significantly lower than that of the ground-level atoms, the multi-step ionization processes

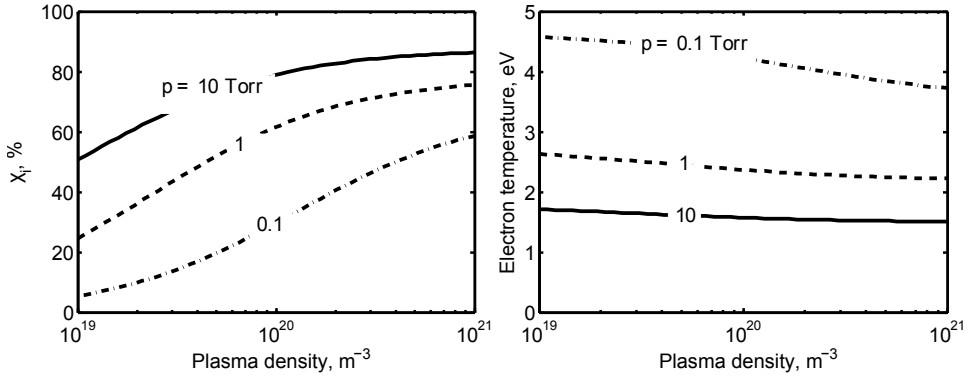

Figure 5.7: Multi-step contribution to the total ionization and electron temperature against plasma density for different pressure levels.

tend to be less affected than the direct-impact electron-neutral ionization rate by the change in T_e. As a consequence, the contribution to the stepwise ionization increases with the pressure. This effect is mainly caused by the increase in the re-adsorption of the radiative photons tied with the deexcitation of the excited atoms. To estimate the plasma penetration length, the mean free path for elastic and inelastic energy exchange must be calculated. Since the electron-ion and electron-neutral collision frequencies are relatively low, the effective mean free path for elastic energy exchange can be approximated as the electron-electron mean free path[2], $\lambda_{el} \simeq \lambda_{ee} \propto T_e^2/n_e$ while the inelastic mean free path can be calculated as $\lambda_{in} = \left(\sum_j n_i \sigma_{ij}\right)^{-1}$ where σ_{ij} is the collision cross section for production of excited states j. Even though in the present model the effect of the beam electrons on the production of excited states is not included, the results are expected to correctly capture the main dependencies of the IPC length on the total neutral and plasma density. Figure 5.8 shows the inelastic mean free path and the total exchange mean free path λ^* as a function of the neutral number density. As expected, increasing the neutral density, e.g. by an increase in mass flow rate, λ^* decreases implying a reduction in the plasma penetration length. In addition, an increase in plasma density for a given neutral density leads to a reduction in plasma penetration length as observed by Krishnan [32].

It is worth noting that the decrease in electron temperature may be under-

[2]Note that, in contrast to neutral particle collisions, it is not appropriate to call this length "collision mean free path" since a very large number of random small-angle Coulomb collisions deflect their trajectories causing a net momentum loss over this length scale. The total number of collisions involved as the electron traverses a Debye length is in the order of $(n\lambda_D^3)^2/\ln\Lambda \gg 1$.

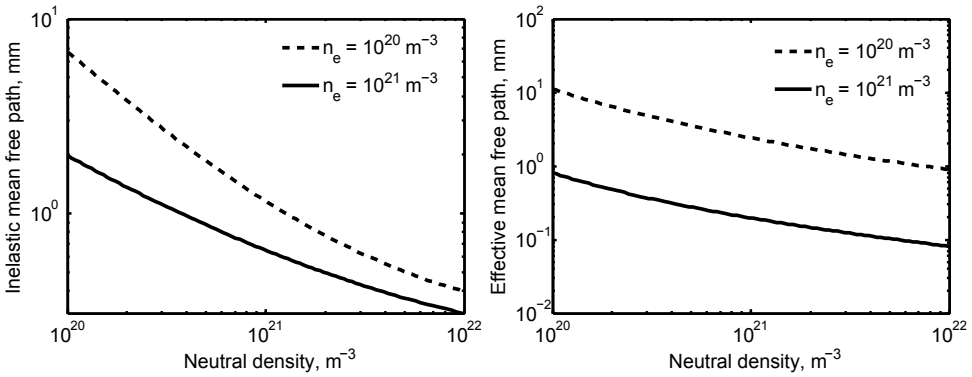

Figure 5.8: Inelastic mean free path and energy exchange mean free path as a function of the neutral density.

estimated in the present calculations since a Maxwellian EEDF was assumed for all the operative conditions investigated. As a matter of fact, Gudmundsson [179] shown that increasing the plasma pressure from few Pa to hundreds of Pa, the EEDF deviates from Maxwellian to become more Druyvesteyn like with a remarkable reduction in sheath voltage and electron temperature. Since the Druyvesteyn energy distribution predicts more electrons with average energy and fewer electrons at higher energies than does the Maxwellian distribution, it seems incorrect by any measure to rely upon the high-energy tail of the Maxwellian distribution for the ionization in a hollow cathode. This is particularly important when orificed-hollow cathodes with small orifice diameters are to be investigated.

Chapter 6

Fundamental Erosion Processes

Cathode mass loss can occur through four main processes: ejection of molten material, chemical-induced reaction by propellant contaminants, evaporation and sputtering. This distinction should be considered as a convenient classification only since a cathode can actually exhibit different erosion mechanisms depending upon its operative conditions. In this context, quasi-steady and steady-state MPD thrusters are characterized by dramatically different electron emission and erosion mechanisms. The nonstationary emission processes in quasi-steady cathode operation and during the start-up phase of steady-state thruster are associated with a very destructive erosion process while the diffuse stationary thermionic emission is inherently less destructive.
In the present Chapter, the main erosion mechanisms for each thruster operative mode are reviewed and discussed to suggest possible ways of improving the cathode lifetime.

6.1 Cathode Erosion in Quasi-Steady MPD Thrusters

In quasi-steady thrusters, the pulse length is sufficiently long for gasdynamic and electromagnetic characteristics of the discharge to reach steady-state conditions even though the electrodes are far from being in thermal equilibrium [180]. In this condition, the cathode erosion is dominated by non-stationary processes required to conduct current through its surface which is too cold to support thermionic emission. Current conduction is thus accomplished by a number of localized, highly-mobile spots, in which the local temperature can be as high as the boiling temperature of the cathode material. Emission initially occurs by field emission at micropoints or inclusions on the cathode surface. Rapid heating leads to explosive release of cathode vapour and to the formation of an emission site, which exist for a very short

time before extinguishing. A new emission site then erupts at a nearby location. These modes are inherently destructive since they require localized regions of very high temperature in which metal vapours are generated.
Historically, cathode spots are classified according to the chemical condition of the electrode. Type-1 spots are observed on non-metallic surfaces or on metallic surfaces with layers of contaminants and consist of many isolated spots ranging from 0.1-1 μm in diameter. Type-2 spots exist on clean metal surfaces. The damage pattern in this mode consists of chains of overlapping craters ranging from 5-20 μm in diameter [181]. The current density of these nonstationary modes has been estimated to range from $10^8 - 10^{12}\ A/m^2$ and erosion rates are as high as $10^0 - 10^4\ \mu g/C$. In the presence of an external magnetic field, arc craters are aligned in a band of well-separated spots for type-1 and in an approximately linear chain for type-2 [98]. Since quasi-steady MPD thrusters are low-pressure, high-current devices in which the cathode surface is generally oxide-free (oxide layers are removed in the first few discharges), the type-2 spot is the most common emission center [182]. Moreover, since the spot internal pressure considerably exceeds the thruster operative pressure, many features of the vacuum arc spots remain unchanged when a gas is added to the discharge system.

6.1.1 Physical Characteristics of Type-2 Spots

At low current levels, type-2 spots appear as a single luminous region carrying a significant fraction of the discharge current. When the current exceeds a certain material-dependent value, the number of simultaneously active emission centers increases proportionally to the arc current (*spot-splitting*) suggesting that each spot can carry only a limited current [183]. The spot-splitting current on tungsten in vacuum was reported by Daalder [184] to be about 250 A and by Kimblin [185] to be approximately 300 A. Generally, an increase in ambient gas pressure causes type-2 spots to divide into fragments carrying smaller currents [111]. Studies of arc damage on clean surfaces have revealed that smaller craters are approximately hemispherical with a depth about equal to one half of the diameter, while large craters tend to have flat bottoms almost independently from the cathode material [184]. Moreover, the diameter of the craters was found to be a mild function of the cathode material with an average value in the order of tens of microns following a lognormal distribution. However, the crater size was found to increase with increasing current up to the spot-splitting current. The spread in the diameter distribution was also found to increase with the current level [184]. At low current levels, the mean crater size approaches a constant value and the spread in the distribution is almost zero. For current levels above a certain value, results indicated that the diameter varies approximately linearly with

current. In addition, the crater size was found to increase with the cathode surface temperature [186].
It is worth noting that the appearance of spots basically depends on the resolution of the equipment used for observation. Every time equipment of higher spatial and temporal resolution became available, new smaller and faster structures were detected. In the last years Anders argued that the experimentally observed spatial self-similarity of the spot racetracks may have a fractal nature [187, 188]. By studying the traces left by a pulse discharge on the surface of an insulator, Anders observed that the structure of multi-spot traces looks very similar to Lichtenberg figures. Moreover, the power spectrum of the ion current revealed a random color noise, $F \sim 1/f^{\alpha}, 1 < \alpha < 2$, within the $10^3 - 10^5$ Hz frequency range on copper and graphite cathodes, suggesting a temporal self-similarity as well [188]. In addition, the FFT of noisy terminal voltage signals showed the $1/f^2$ character in power spectrum for several cathode materials, i.e. the voltage noise has a fractal character which can be associated with a Brownian motion of the spots [189].

6.1.2 Determination of the Main Erosion Mechanism

Cathode erosion rates Γ_{er} are typically determined from weight loss measurements before and after a number of thruster tests, so that $\Gamma_{er} = \Delta m_C / \int I dt$. Assuming a maximum allowable cathode mass loss of 20% for a cathode 1 cm in diameter and 10 cm long operating at 10 kA, the erosion rate should be as low as 0.4 ng/C to guarantee a lifetime of 2000 hours. For quasi-steady MPD thrusters typical erosion rates are in the order of few tens of $\mu g/C$ [190]. It is thus clear that the present quasi-steady MPDT technology cannot be considered as a viable option for future space missions. Moreover, it has to be underlined that the a successful cathode technology capable of long life operations must guarantee a stable surface chemistry to avoid decline in emission capabilities during the service. As a consequence, erosion should not be considered as the only phenomenon affecting the cathode lifetime.
For QS-MPD thrusters operating at low current ($I \lesssim 500\ A$) the erosion rate is dominated by local evaporation and ejection of molten droplets at the crater site. As the discharge current is increased ($I \simeq 1000\ A$), large-scale melting and droplet ejections increase dramatically. Bulk evaporation may dominate only at very high current levels ($I \simeq 10\ kA$). The effect of sputtering should, however, be considered an a case-by-case basis since particle ejection occurs only if enough kinetic energy transferred by the bombarding ions overcomes the surface binding force. Such a threshold energy E_{th} depends upon the incident $j-$particle and $i-$target mass as indicated by Bohdansky [191]. The flux of sputtered material depends on the flux of ions to

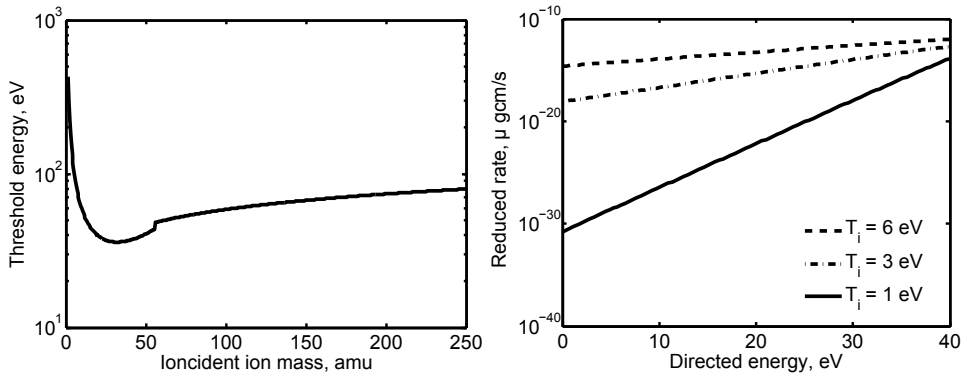

Figure 6.1: Threshold energy for sputtering of tungsten and sputtering rate divided by ion density for Ar ions on W.

the surface Γ_i and by the average yield per ion $\bar{Y}_{ji}$ so that

$$\Gamma_{sp} = \Gamma_i \bar{Y}_{ji} = \Gamma_i \int_{E_{th}^{ji}}^{\infty} f_i(E) Y_{ji}(E) dE \ , \tag{6.1}$$

where the sputter yield $Y_{ji}(E)$ is integrated over the energy distribution function of the ions $f_i(E)$. The ions incident on the cathode wall deliver their random thermal energy and their directed kinetic energy, so that $E_i = ZqV_s + 1/2 m_i v_B^2$, where Zq is the ion charge, V_s is the cathode sheath voltage and v_B is the Bohm velocity. Even though the sheath voltage is in the order of $10-30\ V$ for both quasi-steady and steady-state thrusters, the ions generated by a spot explosion may have charge numbers Z up to five [192]. The threshold energy for tungsten sputtering as a function of incident ion mass is shown in Fig. 6.1. The portion of the curve below 55 amu is based on the estimate threshold energy for low incident-to-target mass ratio while above the small discontinuity, a different approximation, valid for high mass ratios, is used. The sputtering rate for tungsten divided by the ion density at the sheath edge is also displayed in Fig. 6.1 as a function of the directed energy and the ion temperature. Since the threshold energy is very high for light atoms incident on tungsten, the yield of propellants such as hydrogen and lithium is negligible. As regards Ar ions, sputtering may have an important role in the total mass loss if multiple ionization occurs in the metal vapour. Finally, since cathode spots must provide the current continuity, vapour erosion in the emission sites is an inevitable consequence of cold cathode operation and severely limits cathode lifetime.

6.2 Cathode Erosion in Steady-State MPD Thrusters

The cathode in steady-state thrusters is subject to erosion mechanisms which are very different from those in quasi-steady devices since they follow different thermal courses. Even though the discharge initiation mechanism is the same as in pulsed applications, i.e. explosive emission centers associated with type-2 spots, after several seconds of operation a transition from spotty to diffuse arc attachment takes place. In this case the cathode is heated as a whole and the discharge current is emitted through field-enhanced thermionic emission. If the cathode equilibrium temperature does not exceed the melting point of the material, the contribution of droplet ejection to the total mass loss is negligible. Sputtering is generally not an important erosion mechanism since the energy of the impinging ions is below the sputtering threshold for tungsten. As a consequence, if there is no surface melting and the propellant does not contain reactive impurities, the mass loss is dominated by gas diffusion-limited evaporation.

When evaporation and condensation of cathode material are not in equilibrium, a net loss or gain of mass occurs so that the net evaporation rate of the cathode material can be written as $\Gamma_{evap} = \gamma_{evap} - \gamma_{cond} = m(k_{evap} - k_{cond} n_s)$, where n_s is the vapour number density at the surface. At equilibrium there is no net mass transfer, namely $\Gamma_{evap} = 0 \longrightarrow k_{evap} = k_{cond} n_s^{eq}$. Because the evaporation rate k_{evap} depends on processes inherent in the condensed phase and is independent on the state of the vapour phase, this expression for absolute evaporative flux is expected to be also valid under nonequilibrium conditions. Therefore, the net rate of evaporation can be expressed as

$$\Gamma_{evap} = m k_{ads}(n_s^{eq} - n_s) = \alpha \sqrt{\frac{m}{2\pi k_B T_s}} \, (p_s^{eq} - p_s) \ , \tag{6.2}$$

where α is the sticking probability and p_s^{eq} is the equilibrium vapour pressure, which depends only on the surface temperature of the condensed phase. The net evaporation rate approaches zero as the number density of the vapour approaches the equilibrium value and a maximum when the atom number density at the surface is zero. Assuming $p_s \ll p_s^{eq}$, and that the discharge current is provided by thermionic emission only, the main erosion rate for a steady-state cathode can be written as

$$\Gamma_{er}^{SS} = \sqrt{\frac{m}{2\pi k_B T_s}} \frac{p_s^{eq}(T_s)}{j} = \sqrt{\frac{m}{2\pi k_B T_s}} \frac{p_s^{eq}(T_s)}{D T_s^2} \exp\left(\frac{q\varphi}{k_B T_s}\right) . \tag{6.3}$$

Figure 6.2 shows the erosion rate and the specific eroded mass as a function of the cathode surface temperature for different operative time. Even though cathodes for steady-state accelerators would likely be more massive, the types

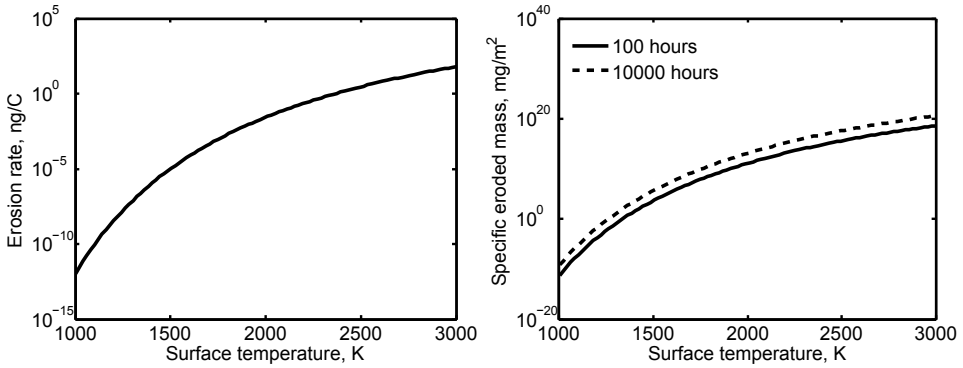

Figure 6.2: Evaporation erosion rate and specific eroded mass as a function of the surface temperature.

of high-power missions that could benefit from the use of such thrusters would require larger total impulses and correspondingly extended lifetimes, in the order of $10^3 - 10^4$ hours. Therefore, the maximum tolerable erosion rate under these conditions is also likely to be on order of few tens of a ng/C. While mass loss is an unavoidable part of the electron emission process, it is much less significant in thermionic cathodes, so this operating regime offers more hope for improving cathode service life.

6.3 Recommendations for Improving Cathode Lifetime

The nonstationary processes inherent in cold cathode operation result in excessive erosion rates for any practical applications. Conventional cathodes in quasi-steady thrusters can thus be replaced with either consumable emitters or externally heated devices. Liquid lithium and solid gallium have been used as consumable cathodes in MPD thruster experiments [193, 194] with encouraging results both in terms of performance and contamination. A quasi-steady thruster might also use a porous tungsten cathode wetted with a liquid emissive material, e.g. lithium or sodium, supplied from the propellant reservoir. In this case the lifetime of the electrode would be limited by erosion of the refractory structure and pore closure, as observed in high-current switches. The only other option appears to be the external heating of the cathode to a temperature sufficiently high to support thermionic emission. As a consequence, the cathode would be subjected to the same erosion problems as steady state thermionic cathodes. However, since the cathode would be kept hot even in the off-phase of the thruster duty cycle, the useful lifetime would be shorter than in a similar steady-state thruster. As a matter of fact, during the off-phase the cathode bulk evaporation is maximum since

$\dot{m}_{evap} \propto (p_{vap} - p_{amb})$. Moreover, the heater reliability may also be a critical issue. A multichannel hollow cathode can be considered as a viable option if feeded with alkali vapours and properly heated. Experimental investigation performed with argon-feed, cold multi-channel hollow cathode has shown no substantial benefits over conventional solid-rod cathodes.

Nevertheless, the quasi-steady cathode option is critical and the advantages of quasi-steady thruster operation compared to alternate technologies are questionable. The steady-state cathode concepts should therefore be given the highest priority. In this context, since an increase in emissive area leads to a *linear* increase in emission current while an increase in temperature affects the emission current *exponentially*, surface temperature has a vastly greater effect on the cathode lifetime since it scales as $L \sim \exp(T^{-1})$. Moreover, for a given discharge current, the cathode temperature scales as $T \sim \exp(\varphi)$, so that specific strategies for minimizing the work function should be considered as fundamental. To this purpose, three main mechanisms are suggested: the use of alternate cathode materials, the adoption of dispenser cathodes and the seeding of the propellant.

6.3.1 Alternate Cathode Materials

As already underlined, elementary emitters (pure metals) suffer either of a high work function, as for refractory metals, or low melting point and high vapor pressure, as for cesium and barium. The use of ceramic compounds such as carbides, borides and oxides has shown superior properties. Among them boride compounds are the most promising. The most well-characterized of the borides in the LaB_6. Lanthanum hexaboride has been used as the electron emitter in hollow cathodes since 1970s and the space heritage of this technology is considerable since over 200 SPT Hall thrusters have flown in Earth orbital applications using LaB_6 cathodes [195]. Polycrystalline LaB_6 cathodes have a work function of about 2.67 eV depending on the surface stoichiometry and emit over 10^5 A/m^2 at temperature of about 1900 K. Since the bulk material is emitting, there is no chemistry involved in establishing the low work function surface and LaB_6 cathodes are almost insensitive to impurities and air exposures that would normally compromise a conventional BaO dispenser cathode [196]. Furthermore, the use of LaB_6 as emitter eliminates the need for the lengthy conditioning processes required when using BaO/W inserts. Nevertheless, the evaporation rate in vacuum exceeds the diffusion rate at temperatures greater than about 2200 K (corresponding to an emitted electron current density of about $7 \cdot 10^5$ A/m^2), leading to depletion of lanthanum near the surface and to an increase in work function [197]. Moreover, LaB_6 emitter cannot be directly touched or supported by most metals during operation due to boron diffusion that causes embrittlement in

high temperature refractory materials. This places some restrictions on the contact techniques and heating mechanisms used in the cathode construction. Metal oxides, such as ThO_2, Y_2O_3 and Ce_2O_3, have work functions in the range 2.3-3.1 eV. However, they are in general n-type semiconductors and their surface is subjected to compositional changes by electrolytic decomposition. Moreover, at current densities over a few 10^4 A/m^2, resistive heating of the oxide become excessive, leading to relatively high evaporation rates. Some of the oxides, such as ZrO_2 and HfO_2, become metallic conductors at sufficiently high temperatures even though their work functions are too high (3.6 and 4.2 eV, respectively) to be considered as alternative to borides.

6.3.2 Dispenser Cathode

Dispenser or reservoir cathodes rely on the migration of the emissive compound towards the surface to replenish the low work function layer. Even though these cathodes have demonstrated extremely long lifetimes at current densities of 10^5 A/m^2 or less in Hall and ion thrusters [198], experimental investigations of dispenser cathodes in MPD thrusters revealed that the activator loss rate is extremely high at the inherent current densities of these devices, i.e. $10^6 - 10^7$ A/m^2, leading to complete depletion of the porous matrix within few tens of hours [37]. All of these cathodes suffer from the problem that the activator supply is too limited to allow for long duration operation at high current levels demanded by MPD thrusters. In addition, since typical dispenser compounds, such as $BaCO_3$ and BaO, are highly prone to poisoning by oxygen adsorption, a very high propellant purity grade and/or efficient oxygen-adsorbing system are needed.

6.3.3 Propellant Seeding

Another approach is to supply the activator as an additive to the propellant (seeding). If a sufficient partial pressure of the activator is maintained over the emitting surface, deposition can balance the desorption rate at a given coverage level. For open-channel cathodes, the adsorption isotherms for the Cs/W system revealed that unreasonable cesium partial pressures are required, evidently decreasing the thruster specific impulse and raising spacecraft contamination issues. A possible solution to this problem can be found in multi-channel hollow cathodes, where the rods pattern acts as a porous matrix keeping the pressure almost constant in the main tube, much like the restriction in orificed hollow cathodes. However, preliminary numerical investigations considering pure gasdynamic processes showed that the surface coverage rapidly drops off near the exit section of each channel. The model indicated that this behavior is caused by a reduction in seed density along with a lower deposition probability of the desorbed particles from the up-

stream locations. Since the surface coverage is maintained by transport from the vapour phase, a density gradient of activator material toward the surface is needed. If the activator is ionized, the preferential drift due to the electric field exceeds the random thermal velocity, leading to a higher activator net flux and thus to a higher deposition rate all along the tube length.

Chapter 7

Hollow Cathode Theoretical Model

In this Chapter a theoretical model for the prediction of the operative conditions of steady-state single-channel hollow cathodes is presented and discussed. The model predicts all the relevant measurable properties including the voltage drop, the cathode maximum temperature, the plasma penetration length and the operative lifetime. The theoretical data are validated against the experimental data found in the literature.
The model herein described is intended as a first attempt to develop, unlike most of the previous models, a fully self-consistent code encompassing all the relevant physical processes in a hollow cathode. In this context, a global (volume-averaged) model appears to be the most practical compromise between including details and keeping the model reasonable in terms of flexibility and computational cost, giving access to scaling laws and explicit expressions.

7.1 Hollow Cathode Performance Model

The primary goal of the theoretical model is to examine the sensitivity of the cathode performance, in terms of power consumption and lifetime, to operative conditions, geometry and material choices. All the equations used are based on a fluid approach, which assumes that particles are perturbed from their Maxwellian distribution function only by virtue of collisions and relax to their equilibrium distribution within the mean time between collisions $\tau = (\nu_{en} + \nu_{ei})^{-1}$. The plasma is assumed to act as a mixture of three perfect gases: thermalized electrons, single-charged positive ions and neutrals. Moreover, the temperature of the heavy species is assumed to be equal to the cathode wall temperature since plasma densities lower than about $10^{23}\ m^{-3}$ are expected. Finally, the effect of any magnetic field is neglected and no

radially-inward pinching forces are considered at the cathode exit section. As a consequence, the outlet section of the cathode is assumed to be sonic, namely $M = 1$. It has to be noted that this is not always the case since, at very high discharge currents, the Bennet pinch effect can significantly alter the downstream pressure leading to a subsonic condition at the cathode exit section. This effect can be estimated considering the ratio between the gasdynamic sonic pressure and the magnetic pressure on a cylindrical arc, $p_G/p_M \propto \dot{m}\sqrt{T_n}/I_d^2$. For a ScHC operating with 5 mg/s in Ar, the condition $p_G/p_M = 1$ is reached for a discharge current of about 180 A. In addition, the electric field inside the channel is considered purely axial in the plasma bulk and purely radial in the sheath. The latter condition is valid only if the magnetic Reynolds number based on the electron flow speed is small compared to unity. Typical values of $Re_m = \mu_0 \sigma_0 u_e L$ at the sheath edge are on the order of 10^{-1}, thus the current flow lines should enter the cathode normal to the surface.
In the spirit of the global model, the plasma in the *active zone* is approximated by a control volume with uniform plasma properties throughout. The main physical processes included in the model are (i) multi-step ionization (ii) work function reduction due to sheath effects, (iii) variable IPC length and (iv) material evaporation. The neglected processes are (i) thermalization of the beam electrons within the plasma, (ii) Bremsstrahlung radiation and (iii) photoelectric emission.

7.1.1 Plasma Model

The current conduction from the plasma to the cathode surface is accomplished via emitted electrons j_{em}, bombarding ions j_i and thermal electrons j_{er}. In this condition, the overall current conservation in steady-state operations is given by

$$j = \frac{I_d}{A_w} = j_{em} + j_i - j_{er} \ , \tag{7.1}$$

where $A_w = \pi D_C \ell$ is the effective arc-attachment. If the field-enhanced thermionic emission is the dominant emission mechanism, the emitted current density can be described by

$$j_{em} = D T_w^2 \exp\left[-\frac{q}{k_B T_w} \left(\varphi_0 - \sqrt{\frac{qE_c}{4\pi\varepsilon_0}} \right) \right] \ , \tag{7.2}$$

where E_w is the electric field at the cathode surface. The determination of the electric field in front of an thermionically emitting surface is based on the work of Prewett and Allen [199]. Solving the Poisson's equation under the boundary conditions of quasi-neutrality at the sheath edge along with the

ion minimum energy criterion, the obtained electric field writes

$$\frac{\varepsilon_0}{2}E_c^2 = nk_BT_e\left[\sqrt{1+\frac{2qV_s}{k_BT_e}} - 2 + \exp\left(-\frac{qV_c}{k_BT_e}\right)\right] - j_{em}\sqrt{\frac{2m_eV_c}{q}}\,, \quad (7.3)$$

where V_s is the potential drop in the cathode sheath. Note that the sheath voltage is different from the cathode voltage drop due to the pre-sheath potential needed to accelerate the ions up to the ion sound velocity, namely $V_c = V_s + V_B$. Detailed analytical relation for the Bohm velocity and for the pre-sheath voltage drop are not available in case of emitting surfaces. However, pre-sheath potentials V_B have been found to slightly vary between $0.5k_BT_e/q$ and $0.69k_BT_e/q$ for collisionless or collisional pre-sheaths, respectively [157]. In the present model, the classical collisionless pre-sheath is considered.

The ion current density is thus determined from the ion flux to the cathode surface as

$$j_i = qn_su_B = qn\exp\left(-\frac{qV_B}{k_BT_e}\right)\sqrt{\frac{k_BT_e}{m_i}}\,, \quad (7.4)$$

where n_s is the plasma density at the sheath edge. Thermal electrons from the plasma bulk can reach the cathode wall if their energy perpendicular to the surface is higher than the sheath potential, namely $k_BT_e/qV_c > 1$. Assuming that the electrons follow a Boltzmann distribution, the flux of electrons towards the wall is given by $\Gamma_e = 1/4n\bar{u}$, where $\bar{u}$ is the average electron velocity. Note that the Boltzmann distribution is strictly valid for isotropic systems only. Since the collision, being randomizing, drive the distribution function towards isotropy, the present derivation assumes a high collisionality of the thermal electrons. Considering that for a fully-ionized gas the collision frequencies scale as $T^{-3/2}$, the typical cold-plasma of many hollow cathode devices is collision-dominated and, thus, the thermal electron current can be written as

$$j_{er} = \frac{1}{4}qn\exp\left(-\frac{qVc}{k_BT_e}\right)\sqrt{\frac{8k_BT_e}{\pi m_e}}\,. \quad (7.5)$$

Another equation is required to estimate the average plasma number density in the control volume. Since the characteristic timescale for plasma ionization, $\tau_i = (n_nK_I)^{-1}$, is much higher than the characteristic transit time, $\tau_t = \ell/v \simeq \ell/u_{th}$, a non-LTE[1] condition is considered. The power balance

[1]Note that the LTE hypothesis does not depend on the particular mechanism of ionization-recombination. This condition requires the kinetic and chemical equilibrium as well as all the plasma properties to be functions of the temperature. Unlike the Complete Thermodynamic Equilibrium (CTE), the LTE approximation considers the plasma to be optically thin and that the plasma temperature can differ from point to point in space and time.

equation at the plasma bulk is solved for the number density taking into account the plasma heating due to Joule effect and the power delivered by the beam electrons. The energy is lost by transport towards the anode through electron current conduction, by ionization events as well as by backstreaming electrons crossing the cathode sheath, namely

$$j_{em}\left(V_c+\frac{3}{2}\frac{k_BT_e}{q}\right)+Rj^2=j_i\left(\varepsilon_i+2\frac{k_BT_i}{q}\right)+\frac{5}{2}\frac{k_BT_e}{q}j+2j_{er}\frac{k_BT_e}{q}\,, \quad (7.6)$$

where $R=\eta\ell/A$ is the classical plasma resistance calculated taking into account electron-ion and electron-neutral collisions. Excitation and radiations losses are neglected since the plasma can be shown to be optically thick, so that the radiated energy is reabsorbed back by the plasma itself. Finally, in steady-state plasma the electrons must be sufficiently hot to create ions at a rate equal to the loss rate towards the wall and across the boundaries of the active zone. The electron and ion momentum equations can be combined together to eliminate the electric field as $nu_i=nu_n-D_a\partial_x n$. At low ion temperatures charge-exchange collisions become dominant and $\sigma_{CEX}\gg\sigma_{in}$. In this condition the ions diffuse slowly since the fast ions and the slow neutrals exchange their energies giving rise to slow ions. Therefore, the relevant mean free path, collision frequency and diffusion coefficient for ion-neutral interaction can be written as $\lambda_{in}=\lambda_{CEX}\simeq(n_n\sigma_{CEX})^{-1}$, $\nu_{in}=n_n\sigma_{CEX}\sqrt{8k_BT_i/\pi m_i}$ and $D_i\simeq\lambda_{CEX}^2\nu_{in}$. The balance is then

$$q\ell\pi r_C^2 n n_n K_I=\frac{4q\pi r_C^2 D_a n}{\ell}+2q\pi\ell D_a n\,, \quad (7.7)$$

where $D_a=(1+T_e/T_i)D_i$ is the ambipolar diffusion coefficient. The previous equation can be recast in a more convenient form as

$$n_nK_I=\frac{2}{r_C^2}\left(1+\frac{T_e}{T_i}\right)\frac{\bar{u}_i}{n_n\sigma_{CEX}}\left[1+2\left(\frac{r_C}{\ell}\right)^2\right]\,, \quad (7.8)$$

in which K_I is the ionization rate coefficient and $\bar{u}_i$ is the mean thermal speed of ions. Fridman [200] suggested a quite convenient equation for numerical estimations of the step-wise ionization rate, namely

$$K_I^{sw}\simeq\frac{g_i}{g_n}\frac{1}{(4\pi\varepsilon_0)^5}\left(\frac{m_eq^{10}}{\hbar^3T_e^3}\right)\exp\left(-\frac{q\varepsilon_i}{k_BT_e}\right)\,. \quad (7.9)$$

The direct impact ionization rate for electron temperatures close to the ionization threshold is given by

$$K_I^d=\sqrt{\frac{8k_BT_e}{\pi m_e}}\sigma_0\exp\left(-\frac{q\varepsilon_i}{k_BT_e}\right)\,, \quad (7.10)$$

where σ_0 is approximately the geometrical atomic cross section which for argon can be taken $\sigma_0 \simeq 3 \cdot 10^{-20}\ m^2$. The total ionization rate coefficient is thus obtained by summing up the step-wise and the direct-impact ionization rates, $K_I = K_I^{sw} + K_I^d$. Different approximations for the direct-impact ionization rate are compared in Fig. 7.1-left. The ionization rate suggested by Heiremann [201] is purely theoretical in nature and includes a multi-level equilibrium ionization scheme taking into account the different binding energies of the valence electrons. On the other hand, Voronov [202] presented a simple analytical expression for the ionization rate fitting a large number of experimental data. The total ionization rate coefficient is shown in Fig. 7.1-right. Since typical hollow cathode plasmas are characterized by $\varepsilon_i/T_e \simeq 10$, the step-wise ionization can be $10^3 - 10^4$ faster that the direct one.

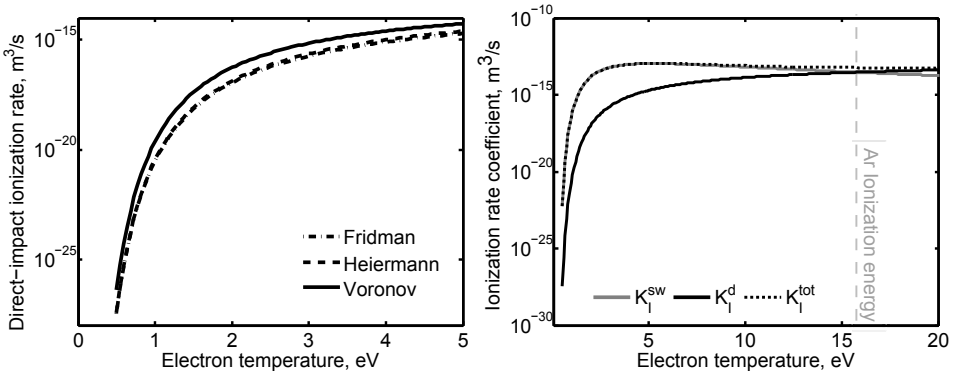

Figure 7.1: Direct-impact ionization reaction rates and total ionization rate.

7.1.2 Cathode Heating and Pressure Model

The cathode surface is subjected to both heating and cooling. Charged particles from the plasma bombard the surface while electron emission, thermal radiation and heat conduction upstream along the cathode remove heat. The net heat deposition per unit area and unit time can be written as

$$Q = P_i + P_{er} - P_{rad} - P_c - P_{em}\ , \tag{7.11}$$

At steady-state Q must be zero and equation (7.11) determines the surface temperature T_w. The total energy delivered by the ions impinging on the surface consists of the acquired kinetic energy across the sheath and of the energy released to neutralize the ion at the surface. The thermal energy of the arriving ions cancels out with the mean energy of the emitted neutral, being the heavy particle temperatures $T_i = T_n = T_w$. As a consequence, the

delivered power per unit area reads

$$P_i = j_i \left(V_c - \varphi_{eff} + \varepsilon_i \right) \ , \tag{7.12}$$

where φ_{eff} is the work function corrected for the electric field effect at the cathode surface. The kinetic energy carried by the bulk electrons as they cross the cathode sheath by virtue of their energy can be estimated assuming a Maxwellian electron energy distribution in terms of potential

$$f(V) = 2\pi \left(\frac{q}{\pi k_B T_e} \right)^{3/2} \sqrt{V} \exp \left(\frac{qV}{k_B T_e} \right) . \tag{7.13}$$

The mean energy of the electrons having $k_B T_e > V_c$ is given by

$$\bar{V} = \frac{\int_{V_c}^{\infty} V f(V) dV}{\int_{V_c}^{\infty} f(V) dV} \ . \tag{7.14}$$

By integration of equation (7.13), the mean energy of the electrons in the plasma bulk is given by $\bar{V} = V_c + 3/2 k_B T_e$. Since the electrons are decelerated by the sheath potential, at the cathode surface their kinetic energy is thus described by $\hat{V} = 3/2 k_B T_e$. As a consequence, the net power delivered by the returning electrons per unit area is

$$P_{er} = j_{er} \left(\frac{3}{2} \frac{k_B T_e}{q} + \varphi_{eff} \right) \ . \tag{7.15}$$

The thermal radiation and the heat conduction can be easily evaluated using the Stefan-Boltzmann relation and the standard Fourier's law, respectively. A lumped-parameter thermal model determines the temperature profile along the cathode length. Convective heat exchange between the propellant and the cathode surfaces is negligible if compared with the other terms. Finally, the power removed by electron emission due to thermionic effect can be estimated considering that the bounded electrons need to overcome the work function barrier to get free from the surface. In doing so, they also remove an energy equal to their mean thermal energy, namely

$$P_{em} = j_{em} \left(\frac{3}{2} \frac{k_B T_w}{q} + \varphi_{eff} \right) \simeq j_{em} \varphi_{eff} \ . \tag{7.16}$$

Even though the emitted electrons are distributed according to a Maxwellian EEDF, the cathode voltage drop is always higher than their mean thermal energy at the surface, $k_B T_w \ll q V_c$ so that the emitted electrons enter the plasma bulk as a mono-energetic beam.

The neutral number density is found through a purely gasdynamic approach assuming a sonic condition at the cathode exit section,

$$(n_e + n_n)\, k_B T_w \left(1 + \alpha \frac{T_e}{T_w}\right) = \frac{\dot{m}}{\pi r_C^2} \sqrt{\frac{R_g T_w}{\gamma} \left(1 + \alpha \frac{T_e}{T_w}\right)}\,, \tag{7.17}$$

where R_g is the specific gas constant, γ is the specific heat ratio and $\alpha = n_e/(n_e + n_n)$ is the degree of ionization. Even though the continuum approach is a quite convenient approximation, preliminary estimations showed that typical Knudsen numbers range between 0.01 and 0.05 leading to a transitional regime between free molecular and viscous continuum [157].

7.1.3 Plasma Penetration Length

A critic parameter of the model is the effective arc-attachment area which is a function of the plasma penetration length inside the cathode, ℓ. The present model postulates that the system follows the principle of minimum power (Steenbeck principle). The total power released in the cathode sheath is given by

$$P_c = A_w \int_0^{\lambda} jE dx = A_w j V_c = I_d V_c\,, \tag{7.18}$$

where λ is the sheath thickness, typically few Debye lengths, and E is the electric field. Since MPD thrusters are current-driven devices, the discharge current I_d can be considered constant so that, according to the minimum power principle, the plasma should arrange itself to minimize the voltage. Such a condition corresponds, by definition, to the minimization of the sheath resistance. On the basis of these considerations, the model is solved for different values of the plasma penetration length, ℓ, seeking for the minimum in the sheath voltage V_c.

7.1.4 Analysis of the Neglected Processes

Among the neglected physical phenomena, the photoelectric emission and the Bremsstrahlung radiation need some comments and explanations. Considering the cathode cavity as an ideal black-body, i.e. all the incident plasma radiation is adsorbed by the cathode wall, the intensity of the radiation is given by

$$I = B(\nu) = \frac{2h\nu^3/c^2}{\exp\left(h\nu/k_B T_e\right) - 1}\,, \tag{7.19}$$

where $B(\nu)$ is the Planck's function. The radiated power in a given wavelength interval $\Delta\lambda$ at wavelength λ is approximately given by

$$P = \frac{2\pi h c^2}{\lambda^5} \frac{1}{\exp(hc/\lambda k_B T_e) - 1} \Delta\lambda A\,, \tag{7.20}$$

where $A \simeq \pi r_C^2 \simeq 8 \cdot 10^{-5}$ is the plasma surface area. Considering an emission line of 100 nm and a Doppler line broadening of $\Delta\lambda/\lambda \propto (T_e/m_n)^{1/2} \simeq 2 \cdot 10^{-5}$, the blackbody radiation power is about 10 W. The photocurrent for incident radiant power P at a wavelength λ is given by

$$I_{ph} = \frac{qP\lambda Q(\lambda)}{hc} \ , \tag{7.21}$$

where $Q(\lambda)$ is the so-called quantum efficiency and indicates the number of emitted electrons per incident photon. For tungsten irradiated with a 100 nm wavelength radiation, $Q(\lambda) \simeq 0.01$ electrons/photon [93]. As a consequence, the photoelectric emission for cathode exposure to the blackbody radiation power of 10 W at 100 nm is approximately $1 \cdot 10^{-2}$ A and, therefore, it can be safely neglected. The power radiated from the plasma due to Bremsstrahlung radiation is not included in the present derivation since, adopting the following relation [157]

$$P_{Br} \simeq 1.43 \cdot 10^{-40} n_e n_i T_e^{1/2} A \ , \tag{7.22}$$

a power of about 10^{-2} W is estimated.

7.2 Theoretical Results

A comparison of the theoretical and experimental results is presented in this Section to demonstrate the validity of the model. Since experimental data on argon-fed open-channel cathode are scarce, a direct comparison is only possible for a limited range of discharge currents and mass flow rates. The experimental data gathered by Downey [172] on a tantalum ScHC are used as reference. The cathode investigated was 2 mm in inner diameter, 38 mm in length and 0.6 mm in wall thickness. The cathode was operated in Ar for discharge currents between 20 and 40 A with mass flow rates ranging from 2 to 3.5 mg/s. The maximum current density with reference to the exit section is therefore about $1.3 \cdot 10^7$ A/m^2. To the author's best knowledge, the experimental study of Downey is the most updated and complete investigation into high-current, gas-fed single-channel hollow cathodes performed so far. The comparison of peak temperature on the outer surface of the cathode as a function of the discharge current for different mass flow rates is shown in Fig 7.2-right.

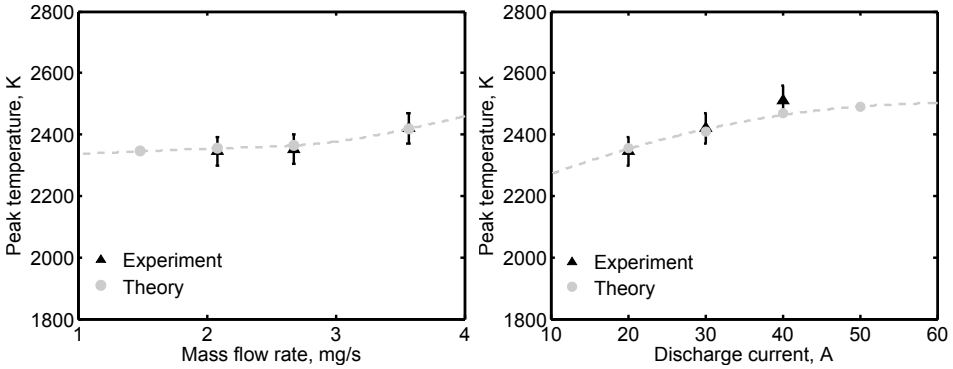

Figure 7.2: Comparison of the cathode peak temperature vs. mass flow rate at 20 A (left) and discharge current at 2 mg/s (right).

Good agreement with the peak temperature is obtained and a nearly linear dependance on the discharge current is predicted by the model and shown experimentally. A slight peak temperature increase with increasing mass flow rates is evident by the experimental data and correctly captured by the model. Even though the dependance of the wall temperature upon the mass flow rate is in contradiction with the data presented by Cassady [157] for lithium-fed cathodes, the empirical data collected by De Tata [203] using an argon-fed McHC corroborate the present finding. According to the present model, the increase in temperature with increasing mass flow rate is tied with a reduction in the plasma penetration length, as shown by Ferreira and Delcoix [31]. Figure 7.3 shows the variation of the axial extension of the *active zone* as a function of the discharge current and mass flow rate. The present results confirm the scaling of an increasing plasma penetration depth with discharge current presented by Cassady [157]. The sheath voltage is found to be a decreasing function of both the discharge current and the mass flow rate as shown by Downey [172]. However, a direct comparison cannot be performed since the total discharge power and terminal voltage were reported, thus including the voltage drops at the anode sheath and along the plasma column. As shown by Goebel [6], the trend of a reducing sheath voltage with increasing current can be explained considering a very simple power balance. Assuming that the net heating plasma power is delivered to the cathode walls only as ion and electron bombarding, the following relation can be written

$$I_d V_c + R I_d^2 - \frac{5}{2}\frac{k_B T_e}{q} I_d \simeq P_i + P_{er} \rightarrow V_c \simeq \sum_j P_j / I_d - R I_d + \frac{5}{2}\frac{k_B T_e}{q} \ . \quad (7.23)$$

Since the net power balance at the cathode surface must be zero in steady state conditions, $\sum_j P_j = P_{cond} + P_{rad} + I_{em}\varphi_0$. Assuming $I_{em} \simeq I_d$, the

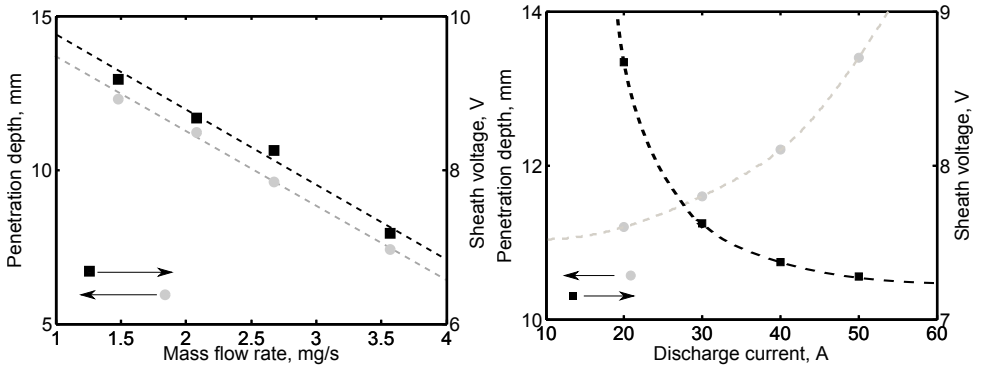

Figure 7.3: Plasma penetration length and sheath voltage vs. mass flow rate at 20 A (left) and discharge current at 2 mg/s (right).

sheath voltage is a linearly increasing function with respect to the total heat lost by conduction and radiation and an almost linearly decreasing function with respect to the discharge current. Figure 7.4 shows that the power consumption increases with the discharge current and decreases with increasing mass flow rate. As the discharge current is increased at constant mass flow rate, the plasma resistance decreases so does the voltage drop. However, since the sheath voltage tends to level off at high current, the net effect is of an increasing power consumption. The predicted electron temperatures as a func-

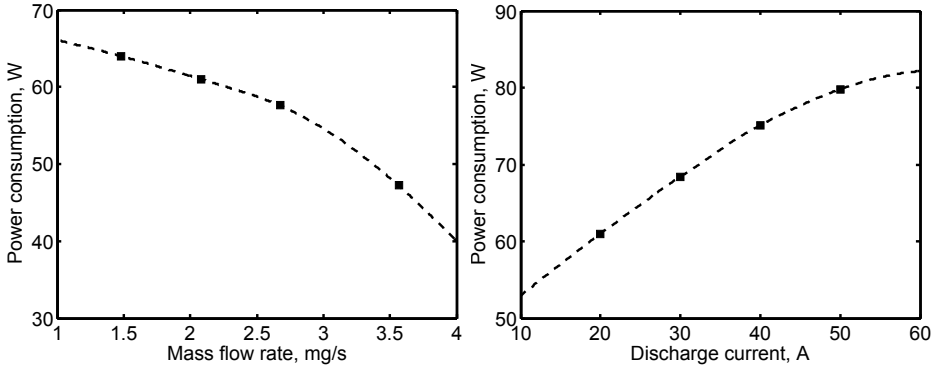

Figure 7.4: Power consumption vs. mass flow rate at 20 A (left) and discharge current at 2 mg/s (right).

tion of the discharge current and mass flow rates are shown in Figure 7.5. The results indicate that the electron temperature is a slightly decreasing function of both the discharge current and mass flow rate in a range of 1-1.3 eV. These results are in good agreement with a wide set of experimental data for differ-

ent cathode geometries and current levels [6, 157, 167, 170]. Since the present model does not include the effect of the energy exchange between the primary electrons and the neutral atoms, the reduction in electron temperature cannot be tied with a reduction in initial energy of the beam electrons as suggested by Downey [172]. It is suggested that such an effect is rather tied with the fact that the electron temperature is constrained to produce sufficient ions to balance the diffusion losses, so that $n_n^2/\sqrt{T_e} \simeq$constant. Since, for a given mass flow rate, the neutral number density scales as $n_n \propto p/T_w \sim T_w^{-1/2}$ and the cathode temperature T_w increases with the discharge current, the electron temperature must decrease to offset the ion diffusion losses to the wall. The same effect is obtained by increasing the mass flow rate since the reduction in plasma penetration length leads to a higher wall temperature. Figure 7.5

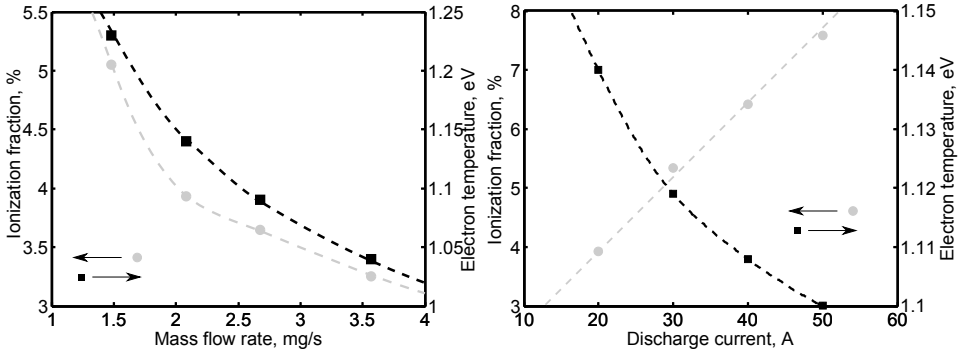

Figure 7.5: Degree of ionization and electron temperature vs. mass flow rate at 20 A (left) and discharge current at 2 mg/s (right).

also shows that the ionization fraction decreases for increasing mass flow rate and shows an almost linear dependence on discharge current, much like the plasma density. These trends can be explained considering that the neutral number density is a slightly decreasing function of the discharge current (doubling the current leads to a 3% reduction in atom density) while the plasma density scales linearly with an increase of about 40% when the discharge current is doubled. While the simple 0-D model is based on a rudimentary thermal analysis and on a crude volume-averaged approach, the qualitative comparison with the available experimental data is encouraging and suggests that the model can be effectively used as a quick tool to illustrate the main physical dependence of the plasma parameters on the geometry and thermal properties of the cathode.

7.2.1 Effect of the Propellant Seeding with Cesium

The effect of the propellant seeding on the emission properties of an open-channel hollow cathode is here analyzed considering a Cs/W system. The flux of cesium towards the surface depends on both ions and neutrals, so that it can be written as

$$J_t = \alpha \frac{p}{k_B T_w} \sqrt{\frac{k_B T_e}{m_{Cs}}} + \frac{p\,(1-\alpha)}{\sqrt{2\pi m_{Cs} k_B T_w}}\,, \tag{7.24}$$

where α is the ionization fraction and p is the partial pressure of the seed. Because of its low ionization potential, cesium is readily ionized, either by surface ionization at the hot cathode or by electron impact in the cavity. Assuming a full-ionized cesium plasma, the flux is determined by the Bohm velocity. Moreover, the cathode wall is assumed to be fully catalytic so that for each adsorbed ion a neutral is desorbed from the surface. No effects on the plasma electrical conductivity are considered. As shown in equation (4.39), the equilibrium surface coverage is obtained from

$$\vartheta - \frac{J_t(T_e) h}{\sigma_m k_B T_w} \exp\left[\frac{q E_d(\vartheta)}{k_B T_w}\right] = 0\,, \tag{7.25}$$

where E_d is the atom desorption energy. By including equation (7.25) and equation (4.32) in the set of equations described above, it is possible to determine the surface temperature and the plasma properties for a given seed number density. The surface temperature as a function of the cesium number density is shown in Fig. 7.6. As expected, a minimum in the peak temperature is observed for a surface coverage of about 0.3. However, a number density of about 10^{24} m^{-3} is needed to reach the minimum temperature. Such a high number density roughly corresponds to a mass flow rate of about 70 mg/s, much higher than the propellant flow rate. Even though the deposition of alkali-metals is an effective method to significantly increase the cathode lifetime, the partial pressure needed to guarantee a proper coverage is definitely too high to be considered a viable option for future MPD thrusters. The use of orificed hollow cathodes to reduce the axial pressure gradient in the main cavity appears not to be a definitive solution since a strong erosion of the orifice is expected with a consequent reduction in internal pressure. It is thus possible to conclude that the use of low-work function refractory ceramics as inserts is the most promising option for high-current, gas-fed MPD accelerators.

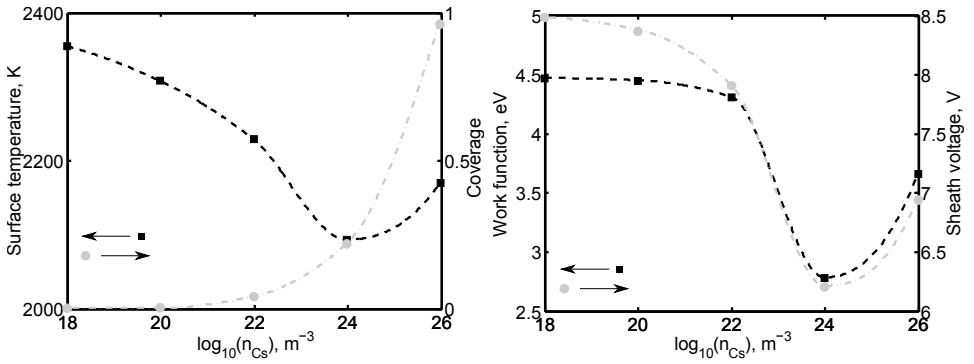

Figure 7.6: Effect of the cesium deposition on peak wall temperature.

7.3 Hollow Cathode Design: Rules of Thumb

In light of the insights gained so far, some rules of thumb and design options concerning open-channel hollow cathodes are here suggested. In an MPD thruster, cathode design is the first step to be accomplished since it determines the overall radial footprint of the thruster for a given $\bar{R}$ ratio. Assuming a requirement of 8000 hours of continuous operation at 2000 A with 80 mg/s of argon, the suggested preliminary design procedure is the following.

Since the ScHC was shown to properly operate when the plasma pressure at the exit section is within few hundreds Pa, a relation between the pressure and the cathode inner radius can be easily found as

$$p = \frac{\dot{m}}{\pi r_C^2}\sqrt{\frac{R_g T_w}{\gamma}\left(1+\alpha\frac{T_e}{T_w}\right)}\,. \tag{7.26}$$

Typical values of the ionization fraction and of the non-equilibrium ratio are $\alpha \simeq 0.1$ and $T_e/T_w \simeq 10$, respectively. As a consequence, the contribution of the electrons to the total pressure can be neglected. For argon propellant equation (7.26) reads $p \simeq 3.56\dot{m}\sqrt{T_w}/r_C^2$ and thus, for an exit pressure of 400 Pa, $r_C^2 \simeq 10^{-2}\dot{m}\sqrt{T_w}$. The maximum wall temperature directly influences the cathode lifetime and thus it should be estimated from the material evaporation rate equation. Assuming a maximum evaporated mass of 10%, the maximum allowable temperature is given by

$$\frac{p_s^{eq}(T_w)}{\sqrt{T_w}} \simeq \frac{1}{10}\frac{t\rho_w}{L_t}\sqrt{\frac{2\pi k_B}{m_w}}\,. \tag{7.27}$$

where L_t is the lifetime, ρ_w is the cathode material density, t is the cathode thickness and p_s^{eq} is the vapour pressure. Figure 7.7 shows the cathode life-

time as a function of the surface temperature for different wall thicknesses. It

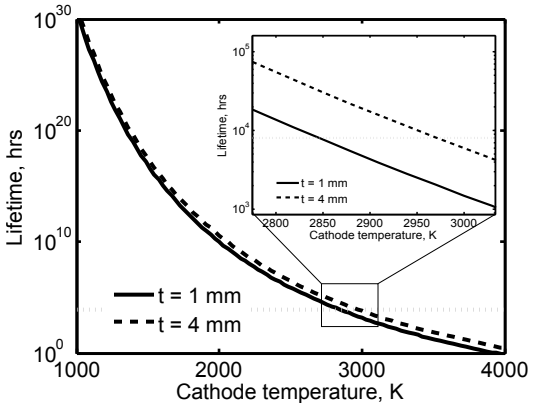

Figure 7.7: Cathode lifetime as a function of the wall temperature.

has to be considered that large thicknesses may induce remarkable temperature differences along the radial direction causing hoop stresses. Assuming a maximum temperature of about 2800 K, the cathode inner diameter is approximately 13 mm leading to a current density of about $1 \cdot 10^7$ A/m^2, a value very close to the current densities suggested by Kaufman [204]. The axial extension of the cathode is mainly determined by thermal dissipation needs. Defining the hot region of the cathode as the location in which the thermal radiation dominates over the conduction, for a given surface temperature the axial extension of such a region can be estimated balancing these two effects, namely

$$\varepsilon\sigma T_w^4 2\pi r_{C,e} L_{eq}^h \simeq 2\kappa T_w \frac{\pi\left(r_{C,e}^2 - r_{C,i}^2\right)}{L_{eq}^h} \,. \tag{7.28}$$

Now, from equation (7.28) the minimum length of the hot zone can be written as

$$L_{eq}^h = \sqrt{\frac{2\kappa t}{\varepsilon\sigma T_w^3}} \,, \tag{7.29}$$

where the condition $t \ll r_{C,i}$ is used. For the thermal radiation to be dominant at a given surface temperature $L^h > L_{eq}^h$. Considering a pure tungsten cathode of 1 mm wall thickness operating at 2800 K, the minimum length of the region at constant temperature is $L_{eq}^h \simeq 13$ mm. It is thus possible to state that the cathode should have a length of at least few times L_{eq}^h, typically $L \simeq 10 L_{eq}^h$. As a consequence, for a given peak temperature the cathode length scales as $L \propto \sqrt{t}$, while, for a given thickness, reducing the maximum temperature a longer cathode is needed due to the lower effectiveness of the

thermal radiation. A more precise analysis can be performed applying a simple conservation of energy so that the temperature profile along the outer surface of the cathode is given by

$$\frac{d^2T_w}{dz^2} - \frac{\epsilon\sigma P_{ir}}{\kappa A_c} T_w^4 = 0 \; . \tag{7.30}$$

where A_c is the cathode cross-sectional area and P_{ir} the external perimeter. Solving equation (7.30) for $T_w(0) = 2800\ K$ and $\partial_z T_w|_{z=L} = 0$, the temperature profiles reported in Fig. 7.8-left are obtained. Since thermal conduction

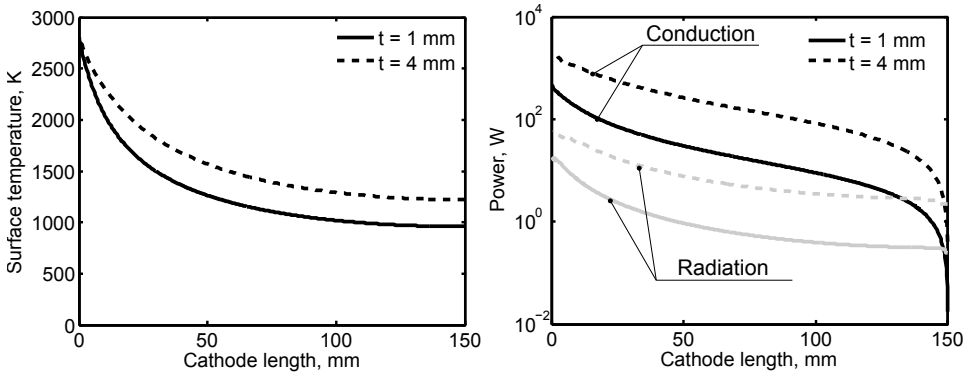

Figure 7.8: Axial temperature profile (left) and power apportionment (right).

is the main heat transfer mechanism, in order to reduce the cathode axial extension, small wall thicknesses should be preferred. Moreover, the use of low-conductivity metals, e.g. tantalum, results in a higher contribution of the thermal radiation to the total heat transfer. Clearly, a trade-off between thermo-mechanical properties, e.g. embrittlement and mechanical loads, and lifetime constrains must be found.

Single crystal refractory metals eliminate recrystallization effects limiting the occurrence of brittle fracture, however they are very expensive and available in rods up to 25 mm dia. The use of W-Re alloys is recommended due to their high mechanical characteristics, especially at high temperatures, and extended plastic domain with respect to pure tungsten. However, the addition of rhenium induces a significant increase in resistivity that may lead to remarkable ohmic losses. An interesting material for steady-state cathodes is the molybdenum alloy TZM (Tungsten 0.5%, Zirconium 0.05%, Molybdenum), offering high recrystallization temperatures (1800-2100 K) and good mechanical properties up to about 2200 K. Propellant purity is often underestimated even though oxygen adsorption may induce a strong reduction in

both mechanical properties and in the ductile-to-brittle transition temperature. A high purity grade propellant (oxygen less than 2 ppm) is therefore recommended. As an alternative, a getter can be used on the propellant feeding line to reduce the cost of the lifetime tests.

Chapter 8

Conclusions

The aim of this dissertation was to identify the main physical processes characterizing high-current hollow cathodes and to outline scaling relations for their design. The approach taken in this investigation was twofold. Initially, a multi-channel hollow cathode was designed and tested on a 100-kW class applied-field MPD thruster to identify the main critical issues and lifetime limiters. Next, a theoretical study was performed to devise possible methods to extend lifetime and performance of high-current electron emitters. Finally, the results of both the experimental investigation and the model were used to propose a design of an improved hollow cathode for MPD thrusters. In this Chapter, the results of the experimental and theoretical results as well as suggested improvements for future developments are presented.

8.1 Summary of Major Results

The results of the 100-kW, quasi-steady MPD thruster experimental campaign pointed out the following important aspects

- The hollow cathode configuration gives no substantial benefits in terms of discharge voltage and lifetime.

- The mechanical stability of the multi-channel configuration is questionable for unsteady applications.

- The current attachment takes place mainly on the outer surface of the cathode unless the discharge timescale is extended to few hundreds milliseconds. With extended pulse length, a transition from lateral to frontal arc attachment is observed.

- The terminal voltage is almost independent of current attachment location at the cathode.

In light of these results, steady-state MPD thrusters are the most promising options for extended in-flight operations. In this regime, evaporation of the cathode material along with oxygen contamination are found to be the main erosion processes. Since the evaporation is a thermo-activated process, two ways aimed at the work function reduction are identified: the adsorption of alkali-metal vapors and the use of bulk-emitting inserts. A simple volume-averaged theoretical model has been developed to assess the effect of these solutions on the performance of high-current cathodes. In spite of the apparent simplicity of the equations involved, several interesting aspects have been pointed out, such as the effect of the plasma penetration length on the cathode temperature and the role of the step-wise ionization in the high-density hollow cathodes plasmas. The fundamental insights are given as follows:

- Propellant seeding is an effective way to remarkably reduce the operative temperature, providing both a reduction in work function and ionization losses.
- The effectiveness of the seeding technique on the emission properties becomes substantial only at high internal pressures, so that large mass flow rates are needed.
- The use of bulk-emitting materials such as LaB_6, together with low-pressure cathode configurations provides the most effective strategy for extending the operative lifetime.

Moreover, the model suggests the following physical dependencies:

- The non-equilibrium multi-step ionization process is predominant in hollow cathode plasmas.
- The peak temperature slightly increases with mass flow rate.
- The plasma penetration length increases with current and decreases with mass flow rate.
- The cathode sheath voltage decreases with increasing current and mass flow rates.
- The cathode sheath voltage does not increase with the plasma penetration depth.
- The Schottky effect increases the thermionic emission by about 30% in the operation conditions investigated.

The model indicates that the ion bombardment is by far the most important cathode heating mechanism while thermionic emission is the most effective heat loss process at high current densities.

8.2 Recommendations for Future Developments

Even though multi-channel hollow cathodes were shown to operate in steady-state regime with lower sheath voltage and slightly lower peak temperature with respect to open-channel cathodes, they cannot be considered the definitive option for long-lasting gas-fed MPD thrusters due to the excessive evaporation of the emitting material. In order to overcome such a limitation, it is here suggested to experimentally investigate both alkali-seeded orificed hollow cathodes and open-channel hollow cathodes with LaB_6 inserts. Experiments with OHCs should be conducted with different orifice diameters to identify the optimal internal pressure while ScHCs should be operated at low internal pressures to guarantee a proper contact of the emitter with the plasma.
Theoretically, a number of questions still remain unanswered and should be addressed in the future to better understand the physical mechanism behind the plasma-wall interaction in hollow cathodes. Most importantly, in this study the effect of the primary electrons has not been directly included. Since the beam electrons are expected to greatly enhance the neutral excitation, the present model underestimates the ionization rate in the *active zone*. Furthermore, future developments should consider the deviation of electron energy distribution function from Maxwellian to Druyvesteyn at high internal pressures. Since the Druyvesteyn distribution leads to a shift of the mean energy at higher electron temperatures with respect to the Maxwell-Boltzmann distribution, a direct effect on the total ionization-excitation rate is expected.

Bibliography

[1] E.Y. Choueiri. A Critical History of Electric Propulsion: The First 50 Years (1906-1956). *Journal of Propulsion and Power*, 20(2):193–203, 2004.

[2] R.H. Goddard. *The Papers of Robert H. Goddard*. McGraw-Hill, New York, 1970.

[3] P. J. Wilbur, R. G. Jahn, and F. C. Curran. Space Electric Propulsion Plasmas. *IEEE Transactions on Plasma Science*, 19(6):1167–1179, 1991.

[4] M.A. Birkan. Introduction to Arcjets and Arc Heaters: An Overview of Research Status and Needs. *Journal of Propulsion and Power*, 12 (6):1011–1017, 1996.

[5] J.E. Polk and K.D. Goodfellow. Results of a 1462 Hour Ammonia Arcjet Endurance Test. In *28th Joint Propulsion Conference*, Nashville, TN, USA, July 6-8 1992. AIAA-1992-3833.

[6] D.M. Goebel and I. Katz. *Fundamentals of Electric Propulsion: Ion and Hall Thrusters*. JPL Space Science and Technology Series. John Wiley and Sons, Ltd, 2008.

[7] M.A. Beattie and J.N. Matossian. Status of Xenon Ion Propulsion Technology. *Journal of Propulsion and Power*, 6(2):145–150, 1990.

[8] P. J. Wilbur and V. K. Rawlin. Ion Thruster Development Trends and Status in the united states. *Journal of Propulsion and Power*, 14(5): 708–715, 1998.

[9] A. I. Morozov and V. V. Savelyev. Fundamentals of Stationary Plasma Thruster Theory. In B. B. Kadomtsev and V. D. Shafranov, editors,

Reviews of Plasma Physics, volume 21, pages 203–391. Springer US, 2000.

[10] V. Kim. Main Physical Features and Processes Determining the Performance of Stationary Plasma Thrusters. *Journal of Propulsion and Power*, 14(5):736–743, 1998.

[11] R.G. Jahn. *Physics of Electric Propulsion*. McGraw-Hill series in missile and space technology. McGraw-Hill, 1968.

[12] L.L. Conrad. The Use of Plasma for Propulsion of Interplanetary Rockets. In S.W. Kash, editor, *Plasma acceleration*, pages 3–11. Stanford University Press, 1960.

[13] E. Ahedo. Plasmas for Space Propulsion. *Plasma Physics and Controlled Fusion*, 53(12):124037, 2011.

[14] M. Andrenucci. *Magnetoplasmadynamic Thrusters*, volume 2, chapter 112. John Wiley and Sons, Ltd, 2010.

[15] M. Martinez-Sanchez and J.E. Pollard. Spacecraft Electric Propulsion-An Overview. *Journal of Propulsion and Power*, 14(5):688–699, 1998.

[16] H. Alfvén. Collision Between a Nonionized Gas and a Magnetized Plasma. *Reviews of Modern Physics*, 32:710–713, October 1960.

[17] F. Paganucci and M. Andrenucci. MPD Thruster Performance Using Pure Gases and Mixtures as Propellant. In *31st Joint Propulsion Conference*, San Diego, CA, USA, July 10-12 1995. AIAA-1995-2675.

[18] A.D. Gallimore. *Anode Power Deposition in Coaxial MPD Thrusters*. PhD in Aerospace Engineering, Dept. Aerospace and Mechanical Engineering, Princeton University, 1992.

[19] T. Andreussi, S. Giannelli, F. Pegoraro, and M. Andrenucci. Fundamental Properties of Plasma Flows in MPD Thrusters. In *47th Joint Propulsion Conference*, San Diego, CA, USA, 31 July - 03 August 2011. AIAA-2011-5888.

[20] K. Kuriki, Y. Kunii, and Y. Shimizu. Idealized Model for Plasma Acceleration in an MHD Channel. *AIAA Journal*, 21(3):322–326, 1981.

[21] A. Fruchtman. Limits on the Efficiency of Several Electric Thruster Configurations. *Physics of Plasmas*, 10(5):2100–2107, 2003.

[22] G. Krülle, M. Auweter-Kurtz, and A. Sasoh. Technology and Application Aspects of Applied Field Magnetoplasadynamic Propulsion. *Journal of Propulsion and Power*, 14(5):754–763, 1998.

[23] A.D. Kodys and E.Y. Choueiri. A Critical Review of the State-of-the-Art in the Performance of Applied-Field MPD Thrusters. In *41st Joint Propulsion Conference*, Tucson, AZ, USA, July 10-14 2005. AIAA-2005-4247.

[24] A.P. Shubin. Dynamic Nature of Critical Regimes in Steady-State High-Current Plasma Accelerator. *Soviet Journal of Plasma Physics*, 2:18–21, 1976.

[25] A. Di Vita, F. Paganucci, P. Rossetti, and M. Andrenucci. Spontaneous Symmetry Breaking in MPD Plasmas. In *36th Joint Propulsion Conference*, Hunstville, AL, USA, July 16-19 2000. AIAA-2000-3538.

[26] E. Y. Choueiri. Instability of a Current-Carrying Finite-Beta Collisional Plasma. *Physical Review E*, 64(6):066413, 2001.

[27] A. G. Korsun. Current Limiting by Self Magnetic Field in a Plasma Accelerator. *Soviet Physics-Technical Physics*, 19(1):124–126, 1974.

[28] F. G. Baksht, B. Y. Moizhes, and A. B. Rybakov. Crtical Regime of a Plasma Accelerator. *Soviet Physics-Technical Physics*, 18(12):1613–1616, 1974.

[29] L. Uribarri. *Onset Voltage Hash and Anode in Quasi-Steady MPD Thrusters*. Phd Thesis, Dept. Aerospace and Mechanical Engineering, Princeton University, Princeton, NJ, 2008.

[30] J.E. Polk, W.F. von Jaskowsky, A.J. Kelley, and R.G. Jahn. Measurment of MPD Thruster Erosion Using Surface Layer Activation. *Journal of Propulsion and Power*, 3(1):33–38, 1987.

[31] C.M. Ferreira and J.L. Delcorix. Theory of the Hollow Cathode Arc. *Journal of Applied Physics*, 49(4):2380–2395, 1978.

[32] M. Krishnan, R.G. Jahn, W.F. von Jaskowsky, and K.E. Clark. Physical Processes in Hollow Cathodes. *AIAA Journal*, 15(9):1217–1223, 1977.

[33] V.I Kolobov and L.D. Tsendin. Analytic Model of the Hollow Cathode Effect. *Plasma Sources Science and Technology*, 4(4):551–557, 1995.

[34] J.L. Delcorix, H. Minoo, and A.R. Trindade. Gas Fed Multichannel Hollow Cathode Arcs. *Review of Scientific Instruments*, 40(12):1555–1562, 1969.

[35] V.G. Ageyev, V.P. Ostrovsky and V.A. Petrosov. High Current Stationary Plasma Accelerator of High Power. In *23rd International Electric Propulsion Conference*, Seattle, WA, USA, September 6-10 1993. IEPC-93-117.

[36] J.S. Fillmore, W.F. von Jaskowsky, A.J. Kelly, and R.G. Jahn. An Experimental Study of Lithium Dispenser Cathodes in the MPD Thruster. In *23rd International Electric Propulsion Conference*, Seattle, WA, USA, September 6-10 1993. IEPC-93-196.

[37] M.A. Mantenieks and R.M. Myers. Preliminary Test Results of a Hollow Cathode MPD Thruster. In *22rd International Electric Propulsion Conference*, Viareggio, Italy, October 14-17 1991. IEPC-91-076.

[38] R.M. Myers, N. Suzuki, A.J. Kelly, and R.G. Jahn. Cathode Phenomena in a Low-Power MPD Thruster. *Journal of Propulsion and Power*, 7(5):760–766, 1988.

[39] D.M. Goebel, J.T. Crow, and A.T. Forrester. Lanthanum Hexaboride Hollow Cathode for Dense Plasma Production. *Review of Scientific Instruments*, 49(4):469–472, 1978.

[40] D.M. Goebel and E. Chu. High-Current Lanthanum Hexaboride Cathodes for High Power Hall Thruster. In *32rd International Electric Propulsion Conference*, Wiesbaden, Germany, September 11-15 2011. IEPC-11-053.

[41] R. Albertoni, F. Paganucci, P. Rossetti, and M. Andrenucci. Experimental Study of a 100-kW Class Applied-FIeld MPD Thruster. In *32nd International Electric Propulsion Conference*, Wiesbaden, Germany, September 11-15 2011. IEPC-11-110.

[42] M. Andrenucci and F. Paganucci. Scale and Geometric Effects on the Performance of MPD Thrusters. In *28th Joint Propulsion Conference*, Nashville, TN, USA, July 6-8 1992. AIAA-92-3159.

[43] F. Paganucci and M. Andrenucci. Performance of an Applied Field MPD Thruster. In *27th International Electric Propulsion Conference*, Pasadena, CA, USA, October 14-19 2001. IEPC-01-132.

[44] R.M. Myers. Applied-Field MPD Thruster Performance with Hydrogen and Argon Propellants. *Journal of Propulsion and Power*, 9(5):781–784, 1993.

[45] R.M. Myers. Applied-Field Geometry Effects. In *27th Joint Propulsion Conference*, Sacramento, CA, USA, June 24-27 1991. AIAA-91-2342.

[46] R.M. Myers. Scaling of 100-kW Class Applied-Field MPD Thrusters. In *28th Joint Propulsion Conference*, Nashville, TN, USA, July 6-8 1992. AIAA-92-3462.

[47] R.M. Myers and G.S. Soulas. Anode Power Deposition in Applied-Field MPD Thrusters. In *28th Joint Propulsion Conference*, Nashville, TN, USA, July 6-8 1992. AIAA-92-3463.

[48] T. Wegemann and M. Auweter-Kurtz. Experimental Comparison of Steady State Nozzle Type and Cylindrical MPD Thrusters at High Current Levels. In *23rd International Electric Propulsion Conference*, Seattle, WA, USA, September 6-10 1993. IEPC-93-122.

[49] M. Winter and M. Auweter-Kurtz. Experimental and Numerical Investigation of Steady-State MPD Thrusters. In *25th International Electric Propulsion Conference*, Cleveland, OH, USA, August 24-28 1997. IEPC-97-113.

[50] D.R. Lev and E.Y. Choueiri. Scaling of Efficiency with Applied Magnetic Field in Magnetoplasmadynamic Thrusters. *Journal of Propulsion and Power*, 58(2):609–616, 2012.

[51] J.E. Daadler. *Cathode Erosion of Metal Vapour Arcs in Vacuum*. Phd thesis, Eindhoven University of Technology, Eindhoven, The Netherlands, 1978.

[52] M. Auweter-Kurtz, B. Glocker, H. Kurtz, and H. Schrade. Cahode Phenomena in Plasma Thrusters. In *21st International Electric Propulsion Conference*, Orlando, FL, USA, July 18-20 1990. AIAA-90-2662.

[53] J.E. Polk, A.J. Kelley, and R.G. Jahn. Characterization of Cold Cathode Erosion Processes. In *20th International Electric Propulsion Conference*, Garmish-Partenkirchen, West Germany, October 3-6 1988. IEPC-88-075.

[54] H. Maecker. Plasmaströmungen in Lichtbögen infolge eigenmagnetischer Kompression. *Zeitschrift für Physik*, Bd. 141:198–216, 1955.

[55] R.L. Burton, K.E. Clark, and R.G. Jahn. Measured Performance of a Multimegawatt MPD Thruster. *Journal of Spacecraft and Rockets*, 20 (3):299–304, 1983.

[56] E.Y. Choueiri. Scaling of Thrust in Self-Field MPD Thrusters. *Journal of Propulsion and Power*, 14(5):744–752, 1998.

[57] V.B. Tikhonov and S.A. Semenihin. Research on Plasma Acceleration Processes in Self-Field and Applied Magnetic Field Thrusters. In *23rd International Electric Propulsion Conference*, Seattle, WA, USA, September 6-10 1993. IEPC-93-076.

[58] A. C. Malliaris, R. L. Garrison, R. R. John, and D. R. Libby. Performance of Quasi-Steady MPD Thrusters at High Powers. *AIAA Journal*, 10(2):121–122, 1972.

[59] P.J. Devillers. *The Acceleration Processes in Magneto-Plasma-Dynamic Arcs*. Phd thesis, University of California, San Diego, CA, 1971.

[60] R.C. Oberth and R.G. Jahn. Anode Phenomena in High Current Accelerators. *AIAA Journal*, 10(1):86–91, 1972.

[61] A.P. Bruckner and R.G. Jahn. Exhaust Plume Structure in a Quasi-Steady MPD Accelerator. *AIAA Journal*, 12(9):1198–1202, 1974.

[62] A. Sasoh. Simple Formulation of Magnetoplasmadynamic Acceleration. *Physics of Plasmas*, 1(3):464–469, 1994.

[63] M. C. Ellis. Survey of Plasma Accelerator Research. *Proceedings of the NASA-University Conference on the Science and Technology of Space Exploration*, 25(1):361–381, 1962.

[64] R. V. Hess, J. Burlock, J. R. Sevier, and P. Brockman. Theory and experiments for the role of space-charge in plasma acceleration. In *Electromagnetics and Fluid Dynamics of Gaseous Plasma*, pages 269–307, 1962.

[65] A. W. Blackstock, D. B. Fradkin, K. W. Liewer, D. J. Roehling, T. F. Stratton, and M. Williams. Experiments using a 25-kw hollow cathode lithium vapor MPD arcjet. *AIAA Journal*, 8(5):886–894, 1970.

[66] G. Krülle. Characteristics and Local Analysis of MPD Thruster Operation. In *AIAA Electric Propulsion and Plasmadynamics Conference*, Colorado Springs, CO, USA, September 11-13 1967. AIAA-67-672.

[67] M. Tanaka and I. Kimura. Current Distribution and Plasma Acceleration in MPD Arcjets with Applied Magnetic Fields. *Journal of Propulsion and Power*, 4(5):428–436, 1987.

[68] P.G. Mikellides and P.J. Turchi. Applied-Field Magnetoplasmadynamic Thrusters, Part 2: Analytic Expressions for Thrust and Voltage. *Journal of Propulsion and Power*, 16(5):894–901, 2000.

[69] F. Allario, R. V. Hess, and O. Jarrett. Onset of rotating disturbance in the interelectrode region and exhaust jet of an mpd arc. *AIAA Journal*, 8(5):902–907, 1970.

[70] M. Zuin, R. Cavazzana, E. Martines, G. Serianni, V. Antoni, M. Bagatin, M. Andrenucci, F. Paganucci, and P. Rossetti. Critical regimes and magnetohydrodynamic instabilities in a magneto-plasmadynamic thruster. *Physics of Plasmas*, 11(19):4761–4770, 2004.

[71] H. Tobari, A. Ando, M. Inutake, and K. Hattori. Characteristics of electromagnetically accelerated plasma flow in an externally applied magnetic field. *Physics of Plasmas*, 14(9):093507, 2007.

[72] A. W. Blackstock, D. B. Fradkin, D. J. Roehling, and T. F. Stratton. A Cesium MHD Arc Jet. *Journal of Applied Physics*, 39(7):3201–3209, 1968.

[73] Y. Kagaya and H. Tahara. Swirl Acceleration in a Quasi-Steady MPD Thruster by Applied Magnetic Noozle. In *29th International Electric Propulsion Conference*, Princeton, New Jersey, USA, October 30 - November 4 2005. IEPC-05-54.

[74] G. Serianni, Vianello N., F. Paganucci, P. Rossetti, and M. Andrenucci. Plasma Diagnostics in an Applied-Field MPD Thruster. In *27th International Electric Propulsion Conference*, Pasadena, CA, USA, October 15-19 2001. IEPC-01-135.

[75] R.M. Myers, A.J. Kelley, and R.G. Jahn. Energy Deposition in Low-Power Coaxial Plasma Thrusters. *Journal of Propulsion and Power*, 7 (5):732–739, 1991.

[76] R.M. Myers. Plume Characteristics of MPD Thrusters: A preliminary Examination. In *25th Joint Propulsion Conference*, Monterey, CA, USA, July 10-12 1989. AIAA-89-2832.

[77] M.T. Randolph, W.F. von Jaskowsky, A.J. Kelley, and R.G. Jahn. Ionization Processes in the Interelectrode Region of an MPD Thruster. In *22nd International Electric Propulsion Conference*, Viareggio, Italy, October 14-17 1991. IEPC-91-052.

[78] R.M. Patrick and A.M. Scheiderman. Performance characteristics of a magnetic annular arc. *AIAA Journal*, 4(2):283–290, 1966.

[79] H. Hügel. Effect of self-magnetic forces on the anode mechanism of a high current discharge. *IEEE Transactions on Plasma Science*, 8(4): 437–442, 1980.

[80] G. C. Soulas and R. M. Myers. Mechanisms of anode power deposition in a low pressure free burning arc. *IEEE Transactions on Plasma Science*, 24(2):478–486, 1996.

[81] R.M. Myers and A.D. Gallimore. Anode Power Deposition in an Applied-Field Segmented Anode MPD Thruster. *Journal of Propulsion and Power*, 10(2):262–268, 1994.

[82] R.M. Myers and M. Mantenieks. Geometric Effects in Applied-Field MPD Thrusters. In *21st International Electric Propulsion Conference*, Orlando, FL, USA, July 18-20 1990. AIAA-90-2669.

[83] N.S. Merinov, I.N. Ostretsov, V.A. Petrosov, and A.A. Porotnikov. Anode Processes with a Negative Potential Drop at the Anode. *Soviet Physics-Technical Physics*, 21(4):467–472, 1975.

[84] L. I. Vainberg, G. A. Liubimov, and G. G. Smolin. High-current discharge effects and anode damage in an end-fire plasma accelerator. *Soviet Physics-Technical Physics*, 48(4):746–753, 1978.

[85] K.D. Diamant, E.Y. Choueiri, and R.G. Jahn. The Role of Spot Mode Transition in the Anode Fall of Pulsed MPD Thrusters. *Journal of Propulsion and Power*, 14(6):1036–1042, 1998.

[86] J. E. Foster and A. D. Gallimore. An Investigation Into the Role that a Transverse Magnetic Field Plays in the Formation of Large Anode Sheath Potentials. *Physics of Plasmas*, 3(11):4239–4249, 1996.

[87] G. A. Dyuzhev, S. M. Shkolnik, and V. G. Yurev. Anode Phenomena in the High-Current Arc. I. *Soviet Physics-Technical Physics*, 23(6): 667–671, 1978.

[88] G. A. Dyuzhev, S. M. Shkolnik, and V. G. Yurev. Anode Phenomena in the High-Current Arc. II. *Soviet Physics-Technical Physics*, 23(6): 672–677, 1978.

[89] V. V. Subramaniam and J. L. Lawless. Thermal Instabilities of the Anode in a Magnetoplasmadynamic Thruster. *Journal of Propulsion and Power*, 6(2):221–224, 1990.

[90] D.R. Lev. *Investigation of Efficiency in Applied Field MagnetoPlasmaDynamic Thrusters*. Phd thesis, Dept. Aerospace and Mechanical Engineering, Princeton University, Princeton, NJ, 2012.

[91] E. H. Niewood. *An Explanation for Anode Voltage Drops in MPD Thrusters*. Phd thesis, Dept. Aerospace Engineering, Massachusetts Institute of Technology, Boston, MA, 1993.

[92] V.B. Tikhonov, F. Paganucci, and M. Andrenucci. Development and Testing of a New Type of MPD Thruster. In *27th International Electric Propulsion Conference*, Pasadena, CA, USA, October 14-19 2001. IEPC-01-123.

[93] K.L. Jensen. Electron Emission Physics. In Kevin L. Jensen, editor, *Electron Emission Physics*, volume 149 of *Advances in Imaging and Electron Physics*. Elsevier, 2007.

[94] O. W. Richardson. Electron Emission from Metals as a Function of Temperature. *Physical Review*, 23(2):153–155, 1924.

[95] S. Dushman. Thermionic Emission. *Reviews of Modern Physics*, 3(1): 190–190, 1931.

[96] R.H. Fowler and L.W. Nordheim. Electron Emission in Intense Electric Fields. *Proceedings of the Royal Society of London A*, 119(781):173–181, 1928.

[97] L.W. Nordheim. The Effect of the Image Force on the Emission and Reflexion of Electrons by Metals. *Proceedings of the Royal Society of London A*, 121(788):626–639, 1928.

[98] A. Anders. *Cathodic Arcs: From Fractal Spots to Energetic Condensation*. Springer Series on Atomic, Optical, and Plasma Physics. Springer, 2008.

[99] L. P. David, editor. *CRC Handbook of Chemistry and Physics*. CRC PRESS, 81 edition, 2000.

[100] A. Kiejna, K.F. Wojciechowski, and J. Zebrowksi. The Temperature Tependence of Metal Work Functions. *Journal of Physics F: Metal Physics*, 9(7):1361–1367, 2001.

[101] J.D. Jackson. *Classical Electrodynamics Third Edition*. Wiley, third edition, 1998.

[102] G. A. Somorjai and Y. Li. *Introduction to Surface Chemistry And Catalysis*. John Wiley & Sons, 2010.

[103] S. Halas and T. Durakiewicz. Work Functions of Elements Expressed in Terms of the Fermi Energy and the Density of Free Electrons. *Journal of Physics: Condensed Matter*, 10(48):815–821, 1998.

[104] S. Halas and T. Durakiewicz. Is Work Function a Surface or a Bulk Property? *Vacuum*, 85(4):486 – 488, 2010.

[105] Y. Shigehiko. Fundamental Physics of Vacuum Electron Sources. *Reports on Progress in Physics*, 69(1):181–231, 2006.

[106] I. Brodie. Uncertainty, Topology and Work Function. *Physical Review B*, 51(19):660–668, 1995.

[107] C. J. Fall, N. Binggeli, and A. Baldereschi. Theoretical Maps of Work-Function Anisotropies. *Physical Review B*, 65(4):401–407, 2001.

[108] K.L. Jensen. Electron Emission Theory and its Applications: Fowler-Nordheim equation and Beyond. *Journal of Vacuum Science and Technology B*, 21(4):1528–1544, 2003.

[109] R. E. Burgess, H. Kroemer, and J. M. Houston. Corrected Values of Fowler-Nordheim Field Emission Functions $v(y)$ and $s(y)$. *Physical Review*, 90(4):515–515, 1953.

[110] J. Paulini, T. Klein, and G. Simon. Thermo-Field Emission and the Nottingham Effect. *Journal of Physics D: Applied Physics*, 26(8):1310–1315, 1993.

[111] B Jüttner. Cathode Spots of Electric Arcs. *Journal of Physics D: Applied Physics*, 34(17):R103–R123, 2001.

[112] E. L. Murphy and R. H. Good. Thermionic Emission, Field Emission, and the Transition Region. *Physical Review*, 102(6):1464–1473, 1956.

[113] E. Hantzsche. The Thermo-Field Emission of Electrons in Arc Discharges. *Beiträge aus der Plasmaphysik*, 22(4):325–346, 1982.

[114] E. Hantzsche and B. Jüttner. Current Density in Arc Spots. *IEEE Transactions on Plasma Science*, 13(5):230–234, 1985.

[115] S. Coulombe and J.L. Meunier. Thermo-field Emission: a Comparative Study. *Journal of Physics D: Applied Physics*, 30(5):776–780, 1997.

[116] S. G. Christov. General Theory of Electron Emission from Metals. *Physica Status Solidi (B)*, 17(1):11–26, 1966.

[117] K. L. Jensen, P. G. O'Shea, and D. W. Feldman. Generalized Electron Emission Model for Field, Thermal, and Photoemission. *Applied Physics Letters*, 81(20):3867–3869, 2002.

[118] S.G. Christov and C.M. Vodenicharov. On the Experimental Proof of the General Theory of Electron Emission from Metals. *Solid-State Electronics*, 11(8):757 – 766, 1968.

[119] A. Petrin. Thermionic Field Emission of Electrons from Metals and Explosive Electron Emission from Micropoints. *Journal of Experimental and Theoretical Physics*, 109(2):314–321, 2009.

[120] W. P. Dyke, J. K. Trolan, E. E. Martin, and J. P. Barbour. The Field Emission Initiated Vacuum Arc. I. Experiments on Arc Initiation. *Physical Review*, 91(5):1043–1054, 1953.

[121] W. W. Dolan, W. P. Dyke, and J. K. Trolan. The Field Emission Initiated Vacuum Arc. II. The Resistively Heated Emitter. *Physical Review*, 91(5):1054–1057, 1953.

[122] F. Paganucci, S. Lorenzini, A. Turco, and M. Andrenucci. Performance of MPD Thrusters with Cathode Heating. In *30th Joint Propulsion Conference*, Indianapolis, IN, USA, June 27-29 1994. AIAA-94-2991.

[123] N. W. Ashcroft and N. D. Mermin. *Solid State Physics*. Saunders College, 1976.

[124] N.S. Rasor and C. Warner. Correlation of Emission Processes for Adsorbed Alkali Films on Metal Surfaces. *Journal of Applied Physics*, 35 (9):2589–2600, 1964.

[125] J. W. Gadzuk. Adsorption Physics of Alkali Metal Vapors on Metal Surfaces - Cesium-Tungsten. M.S. Thesis, Massachusetts Institute of Technology. Dept. of Mechanical Engineering, 1965.

[126] I. Langmuir and K. H. Kingdon. Thermionic Effects Caused by Vapours of Alkali Metals. *Proceedings of the Royal Society of London. Series A*, 107(741):61–79, 1925.

[127] R. W. Gurney. Theory of Electrical Double Layers in Adsorbed Films. *Physical Review*, 47(6):479–482, 1935.

[128] H. Ishida. Theory of the alkali-metal chemisorption on metal surfaces. *Physical Review B*, 38(12):8006–8021, 1988.

[129] H. Ishida. Theory of the alkali-metal chemisorption on metal surfaces. II. *Physical Review B*, 42(17):10899–10911, 1990.

[130] H. Over, H. Bludau, M. Skottke-Klein, G. Ertl, W. Moritz, and C. T. Campbell. Coverage dependence of adsorption-site geometry in the cs/ru(0001) system: A low-energy electron-diffraction analysis. *Physical Review B*, 45(15):8638–8649, 1992.

[131] A. Schmalz, S. Aminpirooz, L. Becker, J. Haase, J. Neugebauer, M. Scheffler, D. R. Batchelor, D. L. Adams, and E. Bögh. Unusual chemisorption geometry of Na on Al(111). *Physical Review Letters*, 67 (16):2163–2166, 1991.

[132] N. D. Lang and W. Kohn. Theory of Metal Surfaces: Work Function. *Physical Review B*, 3(4):1215–1223, 1971.

[133] V. Vlahos, J. H. Booske, and D. Morgan. *Ab initio* investigation of barium-scandium-oxygen coatings on tungsten for electron emitting cathodes. *Phys. Rev. B*, 81(5):4207–4222, 2010.

[134] E. P. Gyftopoulos and J. D. Levine. Work Function Variation of Metals Coated by Metallic Films. *Journal of Applied Physics*, 33(1):67–73, 1962.

[135] J. Topping. On the Mutual Potential Energy of a Plane Network of Doublets. *Proceedings of the Royal Society of London. Series A*, 114 (766):67–72, 1927.

[136] L. D. Schmidt and R. Gomer. Adsorption of Potassium on Tungsten. *The Journal of Chemical Physics*, 42(10):3573–3598, 1965.

[137] L. D. Schmidt. Adsorption of Barium on Tungsten: Measurements on Individual Crystal Planes. *The Journal of Chemical Physics*, 46(10): 3830–3841, 1967.

[138] G.A. Haas, R.E Thomas, A. Shih, and C.R.K. Marrian. Surface characterization of BaO on W: I. Deposited films. *Applied Surface Science*, 40(3):265–276, 1989.

[139] G.A. Haas, R.E. Thomas, C.R.K. Marrian, and A. Shih. Surface characterization of bao on w: Ii. impregnated cathodes. *Applied Surface Science*, 40(3):277 – 286, 1989.

[140] C. S. Wang. High photoemission efficiency of submonolayer cesium-covered surfaces. *Journal of Applied Physics*, 48(4):1477–1479, 1977.

[141] K. L. Jensen, D. W. Feldman, N. A. Moody, and P. G. O'Shea. A photoemission model for low work function coated metal surfaces and its experimental validation. *Journal of Applied Physics*, 99(12):124905, 2006.

[142] L. B. Loeb. *The Kinetic Theory of Gases*. Dover Publications, 2004.

[143] A. Hurkmans, E.G. Overbosch, and J. Los. Trapping probabilities and desorption energies of alkali atoms on a clean and an oxygen covered tungsten (110) surface. *Surface Science*, 59(2):488 – 508, 1976.

[144] H. S. Taylor. The Activation Energy of Adsorption Processes. *Journal of the American Chemical Society*, 53(2):578–597, 1931.

[145] R.I. Masel. *Principles of Adsorption and Reaction on Solid Surfaces*. Wiley Series in Chemical Engineering. Wiley, 1996.

[146] J.H. De Boer. Adsorption Phenomena. volume 8 of *Advances in Catalysis*, pages 17–161. Academic Press, 1956.

[147] J.D. Levine and E.P. Gyftopoulos. Adsorption physics of metallic surfaces partially covered by metallic particles. I Atom and ion desorption energies. *Surface Science*, 1(2):171 – 193, 1964.

[148] J.D. Levine and E.P. Gyftopoulos. Adsorption physics of metals partially covered by metallic particles. II Desorption rates of atoms and ions. *Surface Science*, 1(3):225 – 241, 1964.

[149] J.D. Levine and E.P. Gyftopoulos. Adsorption physics of metals partially covered by metallic particles. part III: Equations of state and electron emission S-curves. *Surface Science*, 1(4):349 – 360, 1964.

[150] J.-F. Bonnal and A. Pelissier. Contact Ionization Theory. *Acta Electronica*, 17:375–382, 1974.

[151] R. Hultgren. Equivalent chemical bonds formed by s, p, and d eigenfunctions. *Physical Review*, 40(6):891–907, 1932.

[152] J. B. Taylor and I. Langmuir. The evaporation of atoms, ions and electrons from caesium films on tungsten. *Physical Review*, 44(6):423–458, 1933.

[153] M. Sajben. Boundary Conditions for Adsorbing-Emitting Electrodes in Contact with Seeded, Dense Plasmas. *AIAA Journal*, 8(3):400–406, 1969.

[154] M.T. Domonkos. *Evaluation of Low-Current Orificed Hollow Cathodes*. Phd thesis, Dept. Aerospace Engineering, The University of Michigan, Ann Arbor, MI, 1999.

[155] L. V. Spencer and U. Fano. Energy Spectrum Resulting from Electron Slowing Down. *Physical Review*, 93(6):1172–1181, 1954.

[156] L.R. Peterson. Discrete Deposition of Energy by Electrons in Gases. *Physical Review*, 187(1):105–111, 1969.

[157] L.D. Cassady. *Lithium-fed Arc Multichannel and Single-Channel Hollow Cathode: Experiment and Theory*. Phd Thesis, Dept. Aerospace and Mechanical Engineering, Princeton University, Princeton, NJ, USA, 2006.

[158] L.M. Lidsky, S.D. Rothleder, D.J. Rose, S. Yoshikawa, C. Michelson, and R.J. Mackin. Highly Ionized Hollow Cathode Discharge. *Journal of Applied Physics*, 33(8):2490–2497, 1962.

[159] J.L. Delcorix, H. Minoo, and A.R. Trindade. Etablissement d'une Règle Générale pour une Décharge D'Arc a Cathode Creuse. *Le Journal de Physique*, 29(7):605–610, 1698. (In French).

[160] D.M. Siegfried. *A Phenomenological Model for Orificed Hollow Cathodes*. PhD Thesis, Dept. Mechanical Engineering, Colorado State University, Fort Collins, CO, USA, 1982.

[161] D. Siegfried and P. J. Wilbur. A Model for Mercury Orificed Hollow Cathodes: Theory and Experiment. In *16th International Electric Propulsion Conference*. New Orelans, LA, USA, AIAA-1982-1889, November, 17.19 1982.

[162] L. Spitzer. *Physics of Fully Ionized Gases*. Interscience Tracts on Physics and Astronomy. Interscience Publishers, 1962.

[163] G.W. Sutton and A. Sherman. *Engineering Magnetohydrodynamics*. Dover Civil and Mechanical Engineering Series. Dover Publications, 2006.

[164] E.P. Vaulin, M.V. Kiryushkina, V.A. Obukhov, and F. Scortecci. Mathematical Modelling of Arc Hollow Cathodes. In *32nd Joint Propulsion Conference*, Lake Buona Vista, FL, USA, July, 1-3 1996. AIAA-96-3184.

[165] P. Rossetti, F. Paganucci, and M. Andrenucci. A Hollow Cathode Model for Application to the Electric Propulsion. In *38th Joint Propulsion Conference*, Indianapolis, IN, USA, July, 7-10 2002. AIAA-2002-4239.

[166] R.V. Kennedy. Theory of the arc hollow cathode. *Journal of Physics D: Applied Physics*, 34(5):787, 2001.

[167] J.L. Delcorix and A.R. Trindade. Hollow cathode arcs. volume 35 of *Advances in Electronics and Electron Physics*, pages 87–190. Elsevier Science & Technology Books, 1974.

[168] V. Phelps. Complilation of Electron Cross Sections, 2005. URL `http://jila.colorado.edu/~avp/collision_data/electronneutral/ELECTRON.TXT`.

[169] Y.B. Zel'dovich and Y.P. Raizer. *Physics of Shock Waves and High-Temperature Hydrodynamic Phenomena*. Dover Books on Physics. Dover Publications, 2002.

[170] A. Salhi. *Theoretical and Experimental Studies of Orificed, Hollow Cathode Operation*. PhD Thesis, Dept. Aeronautical and Astronautical Engineering, The Ohio State University, Columbus, OH, USA, 1993.

[171] Y. Nakamura and M. Kurachi. Electron transport parameters in argon and its momentum transfer cross section. *Journal of Physics D: Applied Physics*, 21(5):718–723, 1988.

[172] R.T. Downey. *Theoretical and Experimental Investigation into High Current Hollow Cathode Arc Attachment*. PhD Thesis, Dept. Astronautical Engineering, University of Southern California, Los Angeles,CA, USA, 2008.

[173] M.A. Lieberman and A.J. Lichtenberg. *Principles of Plasma Discharges and Materials Processing*. Wiley & Sons, second edition, 2005.

[174] A.M. Gomés. Criteria for partial LTE in an argon thermal discharge at atmospheric pressure; validity of the spectroscopically measured electronic temperature. *Journal of Physics D: Applied Physics*, 16(3):357–378, 1983.

[175] K. Katsonis, A. Siskos, K. Dzierzega, S. Pellerin, and M. Tanguy. C-R Modeling of Ar Plasmas: Low Temperature Validation. In *4th International Spacecraft Propulsion Conference*, volume 555 of *ESA Special Publication*, October 2004.

[176] K. Katsonis, C. Berenguer, A. Kaminska, and M. Dudeck. Argon 4s and 4p Excited States Atomic Data Applied in Arc-Jet Modeling. *International Journal of Aerospace Engineering*, 2011:1–15, 2011.

[177] L. Min-Hyong and C. Chin-Wook. Self-consistent global model with multi-step ionizations in inductively coupled plasmas. *Physics of Plasmas*, 12(7):073501, 2005.

[178] S. Ashida, C. Lee, and M.A. Lieberman. Spatially averaged (global) model of time modulated high density argon plasmas. *Journal of Vacuum Science & Technology, A: Vacuum, Surfaces, and Films*, 13(5): 2498–2507, 1995.

[179] J.T. Gudmundsson. On the effect of the electron energy distribution on the plasma parameters of an argon discharge: a global (volume-averaged) model study. *Plasma Sources Science and Technology*, 10(1): 76–81, 2001.

[180] K.E. Clark and R.G. Jahn. Quasi-Steady Plasma Acceleration. *AIAA Journal*, 8(2):216–220, 1969.

[181] G.A. Lyubimov and V.I. Rakhovsky. The Cathode Spot of a Vacuum Arc. *Soviet Physics Uspekhi*, 21(8):693–718, 1978.

[182] N. A. Khizhnyak, B. G. Safronov, V. L. Vereshchagin, and N. P. Popov. Electrode Erosion in Pulsed Plasma Accelerators. *Soviet Physics Technical Physics*, 15(11):1828–1831, 1971.

[183] I. Beilis, B. E. Djakov, B. Jüttner, and H. Pursch. Structure and dynamics of high-current arc cathode spots in vacuum. *Journal of Physics D: Applied Physics*, 30(1):119–130, 1997.

[184] J.E. Daalder. Diameter and Current Density of Single and Multiple Cathode Discharges in Vacuum. *Power Apparatus and Systems, IEEE Transactions on*, PAS-93(6):1747 –1757, 1974.

[185] C.W. Kimblin. Erosion and ionization in the cathode spot regions of vacuum arcs. *Journal of Applied Physics*, 44(7):3074 –3081, 1973.

[186] S. Anders and A. Anders. On modes of arc cathode operation. *Plasma Science, IEEE Transactions on*, 19(1):20 –24, 1991.

[187] T. Schulke and P. Siemroth. Vacuum arc cathode spots as a self-similarity phenomenon. *Plasma Science, IEEE Transactions on*, 24 (1):63 –64, 1996.

[188] A. Anders. The fractal nature of vacuum arc cathode spots. *Plasma Science, IEEE Transactions on*, 33(5):1456 – 1464, 2005.

[189] J. Rosén and A. Anders. Time and material dependence of the voltage noise generated by cathodic vacuum arcs. *Journal of Physics D: Applied Physics*, 38(23):4184, 2005.

[190] J.E. Polk. *Mechanisms of Cathode Erosion in Plasma Thrusters*. Phd thesis, Dept. Aerospace and Mechanical Engineering, Princeton University, Princeton, NJ, USA, 1996.

[191] J. Bohdansky, J. Roth, and H.L. Bay. An analytical formula and important parameters for low-energy ion sputtering. *Journal of Applied Physics*, 51(5):2861–2865, 1980.

[192] G.Y. Yushkov, A. Anders, E.M. Oks, and I.G. Brown. Ion velocities in vacuum arc plasmas. *Journal of Applied Physics*, 88(10):5618–5622, 2000.

[193] O. A. Gorshkov, V.N. Shutov, and Kozubsky K.N. Development of High Power Magnetoplasmadynamic Thrusters in the USSR. In *30th International Electric Propulsion Conference*, Florence, Italy, September, 17-20 2007. IEPC-07-136.

[194] R.E. Thomas, R.L Burton, and K.A. Polzin. Investigation of a Gallium MPD Thruster with an Ablating Cathode. In *46th Joint Propulsion Conference*, Nashville, TN, USA, July, 25-28 2008. AIAA-2010-6529.

[195] K. Kozubskii, V. Murashko, Yu. Rylov, Yu. Trifonov, V. Khodnenko, V. Kim, G. Popov, and V. Obukhov. Stationary plasma thrusters operate in space. *Plasma Physics Reports*, 29:251–266, 2003.

[196] H.E. Gallagher. Poisoning of LaB_6 Cathodes. *Journal of Applied Physics*, 40(1):44–51, 1969.

[197] J.M. Lafferty. Boride Cathodes. *Physical Review*, 79(6):1012–1012, 1950.

[198] T.R. Sarver-Verhey. 28000 Hour Xenon Hollow Cathode Lifetest Results. In *25th International Electric Propulsion Conference*, Cleveland, OH, USA, August, 24-28 1997. IEPC-97-168.

[199] P. D. Prewett and J. E. Allen. The Double Sheath Associated with a Hot Cathode. *Proceedings of the Royal Society of London. A. Mathematical and Physical Sciences*, 348(1655):435–446, 1976.

[200] A. Fridman and L.A. Kennedy. *Plasma Physics and Engineering*. Taylor & Francis, 2004.

[201] J. Heiermann. *Ein Finite-Volumen-Verfahren zur Lösung magnetoplasmadynamischer Erhaltungsgleichungen*. PhD Thesis, Dept. Aerospace Engineering and Geodesy, University of Stuttgart, Stuttgart, BW, Deutschland, 2002.

[202] G.S. Voronov. A Practical Fit Formula for Ionization Rate Coefficients of Atoms and Ions by Elecron Impact:Z=1-28. *Atomic Data and Nuclear Data Tables*, 65(1):1 – 35, 1997.

[203] M. De Tata, R. Albertoni, P. Rossetti, F. Paganucci, and M. Andrenucci. 100-hrs Endurance Test on a Tungsten Multi-Rod Hollow Cathode for MPD Thrusters. In *32nd International Electric Propulsion Conference*, Wiesbaden, Germany, Septermber, 11-15 2011. IEPC-11-108.

[204] H.R. Kaufman and J.R. Kahn. Hollow Cathode Without Low-Work Function Insert. In *29th International Electric Propulsion Conference*, Princeton University, NJ, USA, October 31-November 4, 2005. IEPC-05-47.

[205] K.A. Fichthorn and W.H. Weinberg. Theoretical Fundations of Dynamical Monte Carlo Simulations. *Journal of Chemical Physics*, 95(2): 1090–1096, 1991.

List of Figures

List of Tables